STRESSED OXIDATION OF HAFNIUM DIBORIDE IN AIR AT 1500˚C

THESIS

Thomas A. Bowen, Captain, USAF
AFIT-ENY-MS-17-M-243

DEPARTMENT OF THE AIR FORCE
AIR UNIVERSITY

AIR FORCE INSTITUTE OF TECHNOLOGY

Wright-Patterson Air Force Base, Ohio

AFIT-ENY-MS-17-M-243

STRESSED OXIDATION OF HAFNIUM DIBORIDE IN AIR AT 1500℃

THESIS

Presented to the Faculty

Department of Aeronautics and Astronautics

Graduate School of Engineering and Management

Air Force Institute of Technology

Air University

Air Education and Training Command

In Partial Fulfillment of the Requirements for the

Degree of Master of Science in Materials Science

Thomas A. Bowen, BS

Captain, USAF

March 2017

AFIT-ENY-MS-17-M-243

STRESSED OXIDATION OF HAFNIUM DIBORIDE IN AIR AT 1500℃

Thomas A. Bowen, BS

Captain, USAF

Committee Membership:

Marina B. Ruggles-Wrenn, PhD

Chair

Randall S. Hay, PhD

Member

Sheena L. Winder, PhD

Member

AFIT-ENY-MS-17-M-243

Abstract

Energy management remains a challenge in aerospace applications, especially in hypersonic vehicles. Unlike traditional reentry vehicles whose thermal protection systems must protect against shocks with large standoff distances, hypersonic vehicles with narrow airfoils produce thin boundary layers and shock temperatures in excess of 2000°C, exceeding the operating limits of traditional aerospace materials. The use of ultra-high temperature ceramics (UHTCs) allows for operating temperatures far exceeding those of metallic alloys. One such UHTC is hafnium diboride (HfB_2). Transition metal diborides generally experience significant oxidation degradation at elevated temperatures. The use of additives, such as silicon carbide (SiC) has been shown to reduce the oxidation of transition metal diborides. This research focused on the compressive creep of HfB_2 with varying amounts of SiC in air at 1500°C. The existing test set-up was successfully modified to permit creep testing at higher compressive stress levels for longer durations. Compression creep tests with creep stresses of 75-100 MPa and durations of up to 66.3 h were performed. Post-test microstructural examination revealed significant SiC-depleted layers in HfB_2-SiC samples. The oxide scale thicknesses in HfB_2-SiC samples were up to 95% lower than those produced in monolithic HfB_2 samples, confirming the use of SiC as an effective means to reduce the oxidation of HfB_2. Notably, oxide layer thicknesses in monolithic HfB_2 samples subjected to 75 and 100 MPa compressive creep tests were as much as 32% lower than those observed under zero stress, suggesting that sustained compressive load may restrict oxidation.

Acknowledgements

My success throughout my master's degree studies would not have been possible if not for the immense level of support from a multitude of individuals. Dr. Ruggles-Wrenn ensured I was equipped with the tools to succeed, allowing me to be creative with testing but never letting me stray too far. The countless hours she spent guiding me, not to mention reviewing this document enabled me to be both successful and knowledgeable in my subject field. To all the other ENY students, and especially my fellow materials science brethren, thank you for the countless hours we spent reviewing homework and studying for exams. My introduction to the materials science field would have been far more painful if not for your support. Thank you to Jamie Smith and the other lab techs for fixing the equipment when I broke it, and cracking jokes with me when everything was going well. The AFIT model shop was instrumental in fabricating the custom YAG holders as well as preparing the YAG and extensometer rods. They were always under a time crunch, but continually found time to get my items completed. Thank you to AFRL/RXCC, specifically Tommy Cissel for the hours he spent helping me prepare my specimens (and talking motorcycles), and Kathleen Shugart for teaching me how to use the SEM without breaking it. Finally thank you to my girlfriend Alyssa for listening to presentation practices, proofreading documents, putting up with the all night tests, and missed events throughout my master's studies.

Table of Contents

List of Figures

List of Tables

STRESSED OXIDATION OF HAFNIUM DIBORIDE IN AIR AT 1500°C

I. Introduction

1.1 Motivation

Historically, humans are never content; there is always another boundary to push, a new frontier to exploit. Long before the first successful powered human flight by the Wright Brothers in 1903, man dreamed of soaring into the heavens. The Chinese kite invention in 1000BCE segued to carrying men over battlefields. Springing forward to the 20th Century, World Wars one and two drove the cutting edge of aviation, and in less than fifty years after the first powered flight, Chuck Yeager broke the sound barrier in a rocket powered Bell X-1 in 1947 [1]. While this was the first time a human sustained supersonic flight in straight and level conditions, the old aeronautical adage, higher, faster, farther was in full effect.

Soon after the historic X-1 flight, the United States embarked in a space race with Soviet Russia, resulting leaps in both technology and knowledge that remain state of the art today. As National Aerospace and Space Agency (NASA) scientists soon discovered, normal aerodynamic phenomena change drastically above Mach 5. Assumptions made for classical aerodynamics, including those for supersonic flight no longer hold true [2]. A new flight regime is born: hypersonics.

Hypersonics includes flight above Mach 5, as alluded to previously. Phenomena associated with hypersonic flight not seen in other flight regimes include, high speed flow (Mach>5), thin shock layers, entropy layer formation, high viscous interaction and high temperature flows. The combination of these effects, but especially the high temperature

flows, preclude the use of traditional aerospace materials. With shock layer temperatures at Mach 10 roughly 3000K, these extreme temperatures are well outside the range of normal alloy based aerospace materials [2]. Figure 1 compares the maximum service temperature of various materials, and demonstrates the limitations of metal alloys.

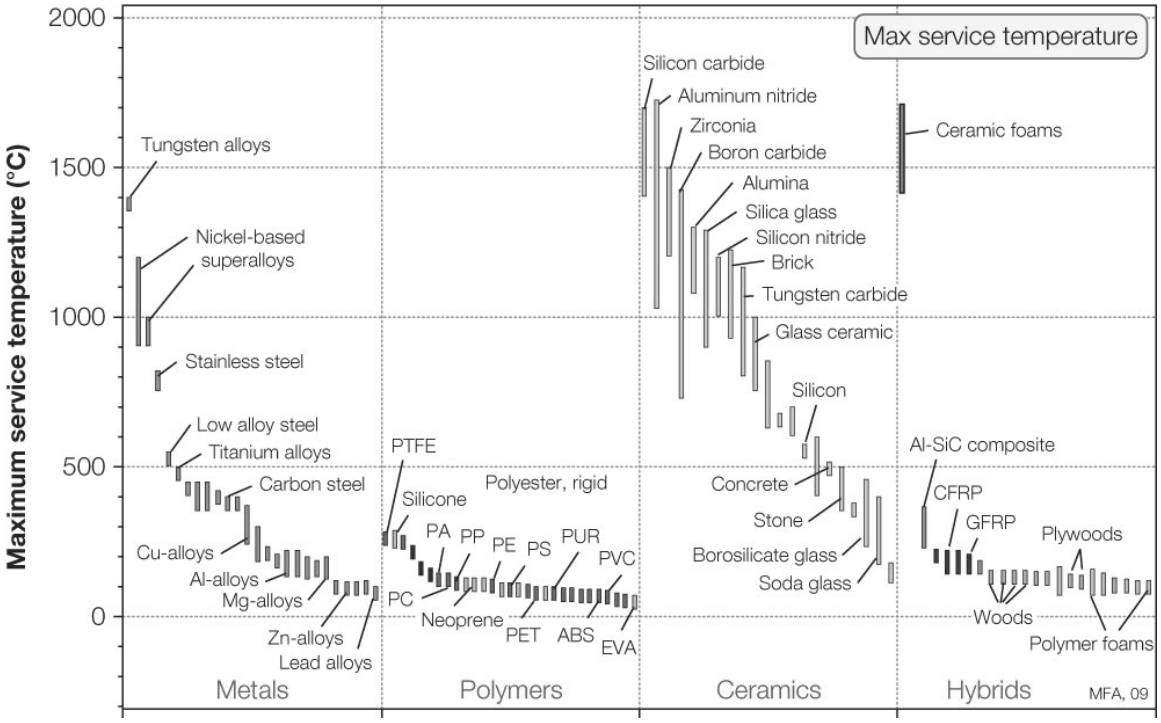

Figure 1. Max Service Temperature for Various Materials, reproduced from [3] with permission from Elsevier.

NASA answered these temperature issues by employing material ablation techniques for thermal energy management. While an effective strategy for single use vehicles as in the case of reentry capsules, or even multi-use vehicles with relatively few flights as with the Space Shuttle, modern military requirements necessitate ground-launched hypersonic vehicles with little to no maintenance between flights [4]. The X-15

demonstrated the damage potential of hypersonic flow when the addition of a ramjet engine resulted in a shock interaction that caused supersonic flow to impinge directly to the body with no separation, creating a high temperature stagnation point that almost completely sheared off the lower pylon, as shown in Figure 2 [5].

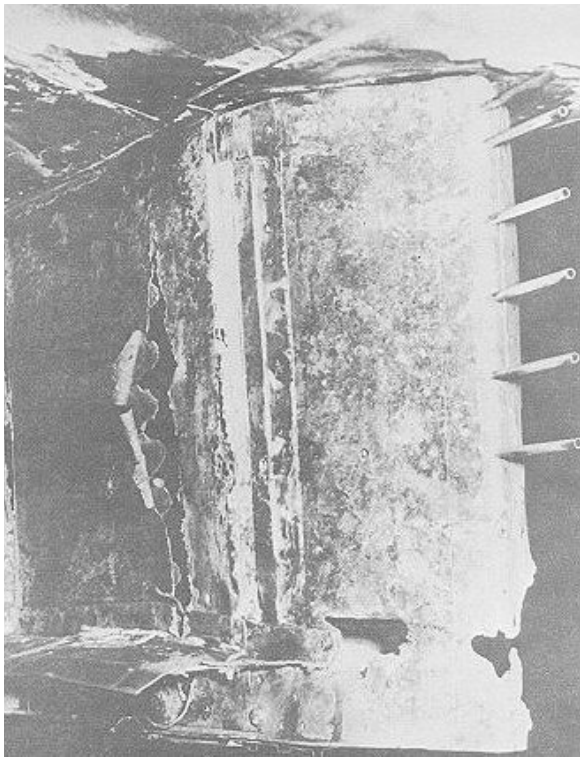

Figure 2. Near-Structural Failure During Flight of X-15, reproduced from [5] courtesy of NASA.

Evidently this becomes a material limitation: a substance that can endure repeated exposure to elevated temperatures and high loads is required for viable hypersonic flight, yet no operational material currently exists. One potential solution involves the use of ultra-high temperature ceramics (UHTCs).

UHTCs have three main advantages over other aerospace materials. They can operate in temperatures in excess of 2000°C, while still retaining their load bearing

abilities [6]. In addition, elevated temperatures tend to increase oxidation rates, with UHTCs categorically less susceptible to oxidation than their super-alloy counterparts [7].

1.2 Problem Statement

UHTCs are candidates for such aerospace applications as sharp leading edges and thermal protection systems for reusable atmospheric re-entry vehicles and hypersonic flight vehicles. However, before UHTCs can be used operationally, their structural integrity and environmental durability must be assured. To provide that assurance, the mechanical behavior of UHTCs at relevant service temperatures and environments must be thoroughly understood and characterized.

This research aims to examine the stressed oxidation of hafnium diboride (HfB_2), an ultra-high temperature ceramic with the potential to fill this material void.

1.3 Research Objectives

Recent Air Force Institute of Technology (AFIT) research developed, constructed and validated a facility for the compression loading of UHTCs in air or argon at temperatures up to 1700°C. The proposed research aims to further improve the test method by exploring the use of sapphire spacers in place of alumina spacers used in prior work. It is envisioned that the sapphire spacers will offer better durability than the alumina spacers, resulting in longer creep tests at higher compressive loads. The basis for this conclusion stems from the observation by Winder in which alumina extensometer rods suffered super-plastic deformation and were successfully replaced with sapphire

extensometer rods [12]. This research will provide the experimental foundation needed to evaluate the stressed oxidation effects of hafnium diboride in air.

1.4 Methodology

a. Perform uniaxial compression creep tests of HfB_2 and HfB_2–SiC in air at 1500°C to characterize the usefulness of sapphire spacers. Repeat tests for various stress inputs to determine the structural limitations of using sapphire spacers in the load train.

b. Conduct creep tests at 1500°C in air with compressive stresses exceeding 50MPa.

c. Characterize the oxidation of HfB_2 and HfB_2–SiC specimens subjected to compression creep at 1500°C by examining the material microstructure via optical and scanning electron microscopy.

d. Compare results to previous work with HfB_2 and HfB_2–SiC.

II. Literature Review

Ultra-high temperature ceramics as introduced in Section I, appear to be a potential solution to the thermal and load bearing material requirement seen in the hypersonic flight spectrum. They fall under the more general category of ceramics, and true to their name, can operate in very high temperatures compared to metallic alloys.

2.1 Ceramics

Ceramics as a material have been used for millennia, with origins dating to 24,000 BCE [8]. They typically involve some sort of heat treatment to cure, and exhibit brittle behavior. These types of ceramics are classified as traditional ceramics, and are composed of clay, silica and feldspar. Engineering ceramics, sometimes referred to as advanced ceramics, are normally nearly pure substances such as aluminum oxide (Al_2O_3) [9]. This research focuses on the latter category.

Advanced ceramics have high resistance to heat, chemicals, abrasion and wear, which increases the difficulty of manufacturing [10]. Engineering ceramics can exhibit very high compressive load capabilities; however, their brittle nature typically results in catastrophic failure under very little strain. This is in stark contrast to metallic alloys which tend to plastically deform before failure [3]. This rigid behavior makes ceramics highly susceptible to impurities and microscopic defects, from which cracks typically originate. A subset of ceramics, called ceramic matrix composites (CMC), utilizes a ceramic as the matrix of a particular composite and various other materials as the fiber reinforcement.

CMCs attempt to bridge the properties of the pure ceramic matrix with the fiber reinforcement. Typically the fibers are utilized to reduce the brittle nature of the ceramic and achieve graceful failure [10]. In this research, the addition of SiC particles to the HfB_2 matrix is primarily for its benefits in oxidation resistance. However DeGregoria found that in certain proportions the balance of SiC fibers enabled the HfB_2-SiC composite to deform significantly more than either of their respective compounds individually [17]. Figure 3 shows a schematic of the creep rates associated with HfB_2 and SiC. Therefore, there exists a composition of HfB_2 and SiC that enables the composite to deform more than their individual components.

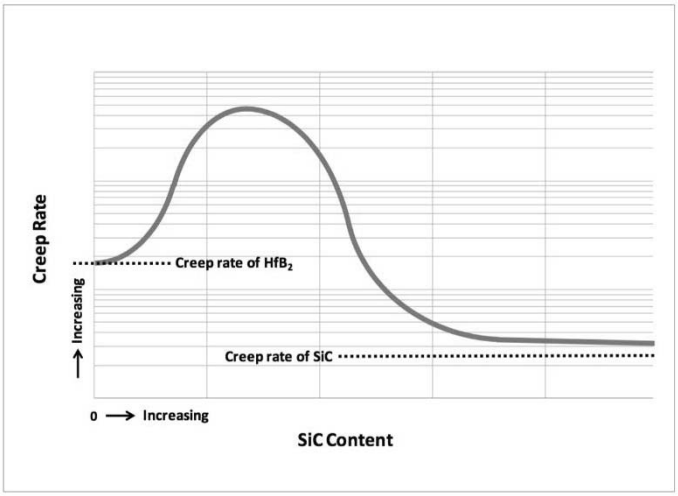

Figure 3. Creep Rate vs. SiC Content, reproduced from [17].

2.2 Ultra High Temperature Ceramics

Ultra-High Temperature Ceramics are a subset of ceramics that have exceptionally high melting temperatures. As mentioned in Section I, UHTCs can operate in environments exceeding 2000°C, making them likely candidates for applications on

hypersonic vehicles. Only fifteen known materials have melting temperatures higher than 3000°C, with the vast majority falling under the UHTC category [6]. Figure 4 compares the melting temperature of various UHTCs to traditional metals.

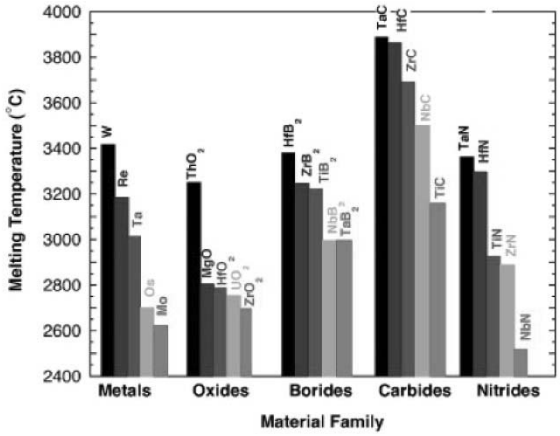

Figure 4. Melting Points of Various Materials, reproduced from [6] with permission from John Wiley and Sons.

UHTCs for applications in aerospace environments must also be load bearing. Oxides have high thermal expansion coefficients making them prone to thermal shock and are more susceptible to failure in aerospace environments. Borides have excellent thermal conductivities allowing them to operate in environments with very rapid temperature changes with lower thermal gradients compared to oxides. Carbides and nitrides can have higher melting temperatures than borides, but typically oxidize more readily, a major concern in operational environments [7]. Therefore, borides are the logical choice for further evaluation.

2.3 Creep

Creep is defined as deformation under constant load. There are three regimes of creep, primary, secondary and tertiary as shown in Figure 5 [11].

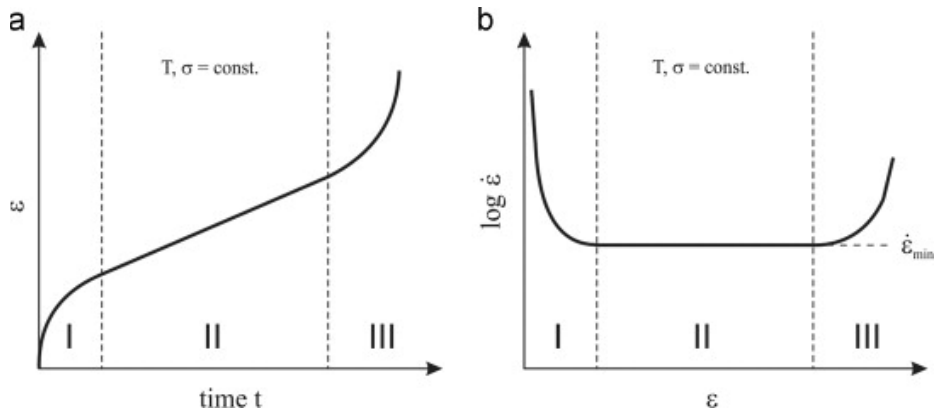

Figure 5. Idealized Three-Regime Creep Curve, reproduced from [11] with permission from Elsevier.

Many models exist depicting creep behavior and model representation is dependent on the material in question. A commonly accepted model for creep is governed by the equations in Figure 6.

For a number of creep mechanisms:

$$\dot{\varepsilon} = \frac{AD\mu b}{kT}\left(\frac{b}{d}\right)^m\left(\frac{\sigma}{\mu}\right)^n \quad (1)$$

Where: $D = D_o \exp\left(\frac{-Q}{RT}\right)$

$\dot{\varepsilon}$ – steady-state creep rate	μ – shear modulus
A – dimensionless constant	k – Boltzmann constant
D – diffusion coefficient	T – absolute temperature
D_o – frequency factor	b – Burgers vector
Q – creep activation energy	d – grain size
R – the gas constant	m – grain size exponent
σ – applied stress	n – stress exponent

Figure 6. Creep Rate Equation for Elevated Temperatures, reproduced from [12]

Creep mechanisms vary by material and test conditions, but typically include dislocation, diffusion, grain boundary sliding and cavitation. Dislocation migrations typically nucleate along grain boundaries, accumulating at triple points. Creep rates controlled by intra-granular dislocations typically involve large stresses at elevated temperatures and flow rates, which are not supported by ceramic materials [13]. Diffusion creep is the result of vacancy migration and a characteristic common among polycrystalline ceramics. In two-phase mixture composites, grain boundary sliding can be the primary creep mechanism at elevated temperature, dependent on stress and grain size. For the material in question, this would represent sliding of the HfB_2 grains against SiC grains [10]. Bird *et. al.* demonstrated this is the primary creep mechanism of zirconium diboride (ZrB_2) at temperatures above 1600°C during flexion tests of ZrB_2 [13]. During the same flexion tests of ZrB_2, cavitation creep was also observed, though cavitation was absent in temperatures below 1500°C. Cavitations also concentrated along grain boundaries, however they were primarily observed in areas under tension; those under compression saw negligible cavitation. Therefore, for the purposes of this research, creep mechanisms will be assumed to be grain boundary sliding as well as Nabarro-Herring creep.

2.4 Oxidation

Oxidation is a chemical process in which oxygen reacts with a particle forming an oxide. The spontaneity of this reaction is driven by the equation:

$$\Delta G = -RT\ lnK_{eq} \tag{2}$$

Where R is the universal gas constant, T is temperature in Kelvin, K_{eq} is the equilibrium constant, and ΔG is the Gibb's free energy, where a negative value indicates a spontaneous process [14]. One such spontaneous reaction is the oxidation reaction of hafnium diboride as governed by the equation below.

$$HfB_2(cr) + \frac{5}{2}O_2(g) \rightarrow HfO_2(cr) + B_2O_3\,(l) \qquad (3)$$

In any oxygen rich environment this process is spontaneous, although reaction rates increase significantly with temperature. Bargeron found the resulting reaction creates a dual layered composition, one of the parent material and the other of the oxide [15]. In Figure 7, the oxide is distinguishable from the parent by its columnar structure in contrast to the parent's uniformity.

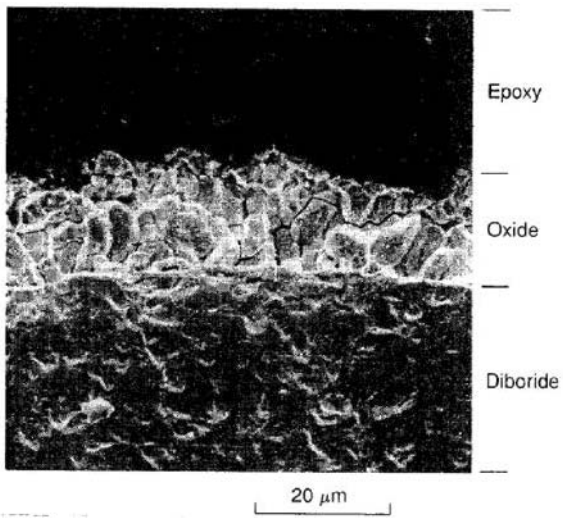

Figure 7. SEM Micrograph of HfB_2 and its Oxide (55 Torr O2, 30 min 1520°C) , reproduced from [15] with permission from © The Johns Hopkins University Applied Physics Laboratory.

This dual nature behavior remains fairly uniform until temperatures approach the boiling point of boric oxide, 1860°C. This results in varied behavior in which HfO_2 is transported and deposited by the liquid and gaseous B_2O_3 as seen in Figure 8. Operating past the boiling point of boric oxide results in the formation of large boria bubbles as evident in Figure 9.

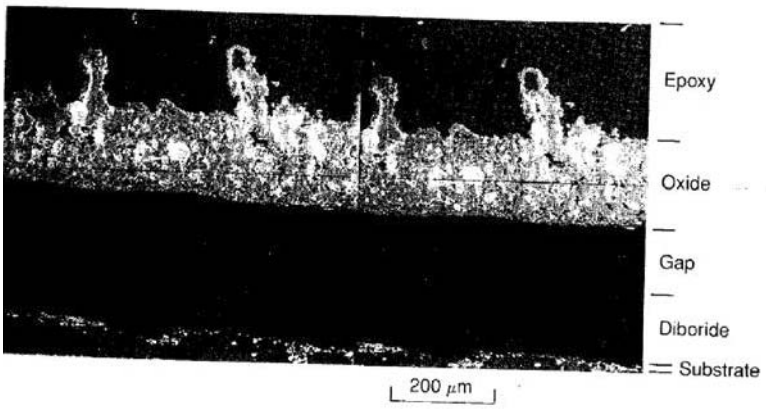

Figure 8. SEM Micrograph of HfB_2 and its Oxide (55 Torr O2, 9min at 1850°C) , reproduced from [15] with permission from © The Johns Hopkins University Applied Physics Laboratory.

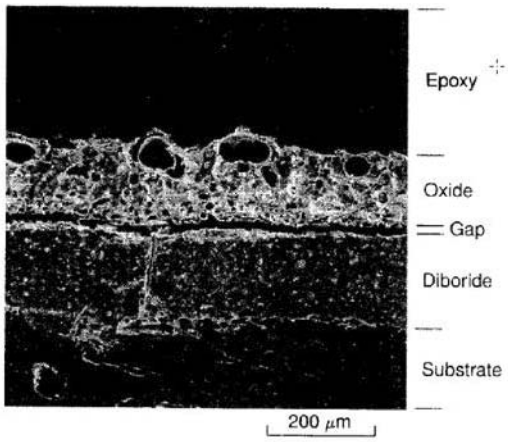

Figure 9. SEM Micrograph of HfB_2 and its Oxide (55 Torr O2, 5min at 1900°C) , reproduced from [15] with permission from © The Johns Hopkins University Applied Physics Laboratory.

However, test results from this research are expected to appear similar to Figure 7. Introducing SiC reinforcement fibers changes the oxidation behavior as mentioned in Section 2.1. Research has shown the oxidation of HfB_2 occurs more readily than that of SiC. However, SiC also oxidizes, combining with liquid boric oxide to produce a surface layer of borosilicate glass, inhibiting oxygen penetration to the parent material [16]. Figure 10 shows the multi-layered nature of the oxidized HfB_2-SiC CMC. Carney identified four distinct regions in the oxidation scale. Region I in Figure 10 represents the borosilicate glass (B_2O_3-SiO_2) region II the hafnium oxide (HfO_2) infused with borosilicate glass, region III HfO_2 with Si-O-C inclusions, and region IV Figure 23. HfB_2 with Si-O-C inclusions (SiC depletion layer) [25]. The reaction equations below show a small subset of the complex series of chemical reactions involved in the oxidation of HfB_2-SiC.

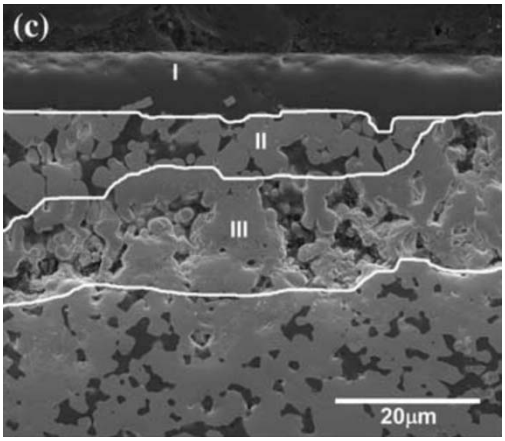

Figure 10. Oxidation of HfB_2-20% SiC at 1600°C (I: SiO_2, II: SiO_2 filled HfO_2, III: HfO_2 with Si-O-C Inclusions), reproduced from [25] with permission from Springer.

$$\frac{2}{5}HfB_2\ (s) + O_2\ (g) \rightarrow \frac{2}{5}HfO_2\ (s) + \frac{2}{5}B_2O_3\ (l) \quad (4)$$

$$\frac{2}{3}SiC\ (s) + O_2\ (g) \rightarrow \frac{2}{3}SiO_2\ (l) + \frac{2}{3}CO\ (g) \quad (5)$$

The effect of stress on the oxidation of HfB_2 has yet to be characterized sufficiently. *Does the compression of HfB_2 result in a reduction of oxidation effects?* Some information has been gathered by previous research dating back to the 1970s, but the most pertinent in the 21st Century.

2.5 Previous Research

High temperature testing of the diboride materials HfB_2 and ZrB_2 began in 1970. Research has focused primarily on ZrB_2, utilizing flexion test methods at elevated temperatures as summarized in Table 1.

Table 1. Diboride UHTC Creep Testing, adapted from DeGregoria [17]

Author	Year	Material	Mechanical Test Method	Temp (°C)	Stress (MPa)	Additives
DeGregoria	2015	HfB_2	Uniaxial Compression	1500	25 to 75	0 to 30% SiC
Winder	2015	HfB_2	Uniaxial Compression	1500	25 to 100	0 to 20% SiC
Gangireddy	2013	ZrB_2	Flexural	1700-2200	20 to 50	30% SiC
Bird	2013	ZrB_2	Flexural	1400-1820	16 to 97	20% SiC
Guo	2011	ZrB_2	Flexural	1500-1600	19	30% SiC
Talmy	2008	ZrB_2	Flexural	1200-1500	30 to 180	0 to 50% SiC
Meléndez-Martinez	2001	ZrB_2	Uniaxial Compression	1400-1600	47 to 472	0, 4% Ni
Kats	1981	ZrB_2	Flexural	1700-2420	5 to 30	0 to 100% ZrC
Spivak	1973	ZrB_2	Flexural	2052-2291	5 to 196	0 to 100 ZrN
Rhodes	1970	Both	Both	800-1800	172	0, 20% SiC

Flexural type testing is much simpler to perform, but creep strain is calculated from deflection, not directly measured. Furthermore, flexural testing imposes compression on one surface and tension on the other. Therefore, uniaxial testing is desirable as it reduces the variability in the experiment. However, uniaxial creep is difficult to perform under these conditions for a multitude of reasons. Firstly, densification of HfB_2 is challenging and the specimens produced are too small to allow

tension testing and must therefore be tested in compression. Secondly, traditional load testing machines are not designed to operate with specimens at ultra-high temperatures.

Winder designed a remote loading system that isolates the test specimen inside a furnace providing sufficient standoff for the machine while still benefiting from the precision of uniaxial testing. Sapphire extensometer rods were employed to aid in the direct measurement of strain, after a set of traditional alumina rods experienced super-plastic deformation [12].

The results from Winder's research highlighted the thermal and chemical instabilities between the materials used in the load train: HfB_2, platinum, and single crystal yttrium aluminum garnet (YAG) rods [12]. Winder utilized single alumina spacers to alleviate the unintended thermochemical reactions. Following Winder's work, DeGregoria performed extensive compressive creep testing using a double-stacked alumina spacer. The use of double stacking was to facilitate specimen removal upon completion of the experiment [17]. However, while these spacers functioned well in regards to preventing unwanted contamination of the HfB_2 specimen, they were the primary failure mode in all of DeGregoria's tests above 25MPa [17]. As a result, the research herein replaces the alumina spacers with sapphire spacers due to their resistance to plastic deformation at testing temperatures as validated by the findings of Winder with the extensometer rods described in Section 1.3.

III. Methodology

This section describes the way in which the test objectives were validated. Included in this section is a description of the material specimen, the test setup and accompanying procedures, as well as observations procedures performed post-test.

3.1 Research Material

The UHTC tested is a hafnium diboride (HfB_2) with varying percentages of silicon carbide (SiC). Samples tested included monolithic HfB_2 (0 vol% SiC), HfB_2-10 vol% SiC and HfB_2-30 vol% SiC. The Air Force Research Laboratory's (AFRL) Materials and Manufacturing Directorate fabricated the material by sintering hafnium, boron, silica and carbon powders to achieve the desired composition and density. C.M. Carney of AFRL was able to achieve 95-99.8% of theoretical density with the introduction of tungsten carbide and tungsten boride in a novel sintering method described in [17, 18]. The lack of porosity enabled the compression testing performed by Winder [12], DeGregoria [17] as well as the tests described herein.

3.2 Test Specimen

The test material produced by AFRL was delivered in puck format and required further processing for use in the high temperature creep test facility. The Air Force Institute of Technology's model shop utilized electric discharge machining (EDM) to cut the pucks to the specifications in Figure 11. Grooves were cut in the face of the specimen to allow for direct strain measurement.

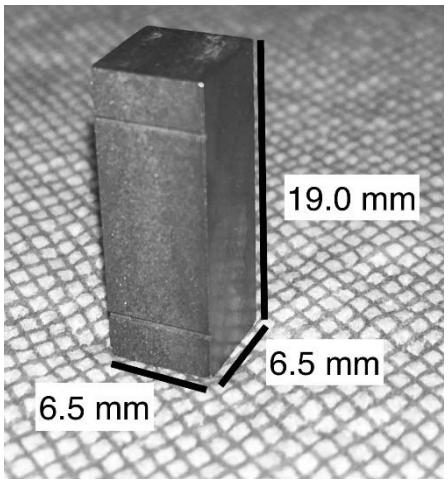

Figure 11. Test Specimen Geometry

Polishing of the specimen was required to remove surface imperfections caused by the EDM process. DeGregoria polished a number of samples to a finish of 45μm [17], including those utilized in this research. Table 2 provides the dimensions of the specimens used in this work.

Table 2. UHTC Test Specimens, Composition and Dimensions

Sample	SiC % (vol)	Width (mm)	Depth (mm)	Height (mm)
HfB2-0Sic-2	0	5.95	6.33	18.95
HfB2-0Sic-3	0	6.05	6.38	18.96
HfB2-10Sic-4	10	7.57	6.54	18.84
HfB2-10Sic-5	10	7.60	6.56	18.81
HfB2-30Sic-3	30	6.19	6.52	18.84

3.3 Test Setup

A detailed description of the specialized test facility and of the method for testing small UHTC specimens in compression at temperatures exceeding 1400°C developed

previously at AFIT are given elsewhere [12, 17]. A brief summary of the test setup and of the test method is offered below.

The test setup integrates the MTS testing machine with a custom furnace and a temperature controller for elevated temperature testing. The servo-hydraulic MTS model 810 test machine was equipped with a 5 KIP load cell and water-cooled wedge grips. A FlexTest 40 Digital Controller running FlexTest version 5.2B software was used for input signal generation and for data acquisition. Strain was measured by a MTS model 632.53E-14 axial high-temperature extensometer, equipped with custom sapphire extension rods. Elevated temperature was achieved using a custom single zone resistance furnace with $MoSi_2$ heating elements controlled by a Eurotherm 3504 temperature controller. Foil backed alumina blankets wrapped around the furnace provided additional insulation needed to reach the desired test temperature. Figure 12 shows the test equipment with the furnace open.

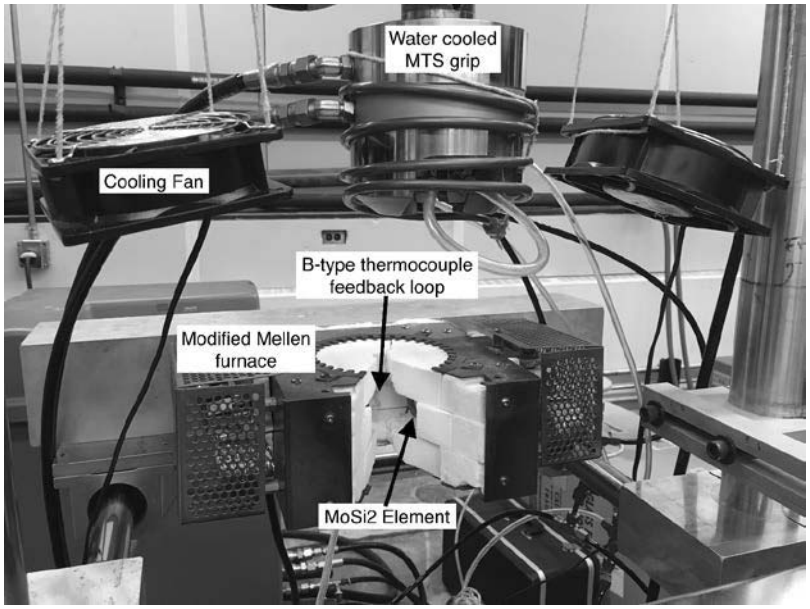

Figure 12. Test Equipment with Open Furnace

The method for testing small UHTC specimens in compression at elevated temperature is schematically depicted in Figure 13. According to this test method, the high purity (99.9999%) single-crystal yttrium aluminum garnet (YAG) pushrods of 10-mm diameter are used to apply compressive stress to the HfB_2 specimen in the furnace hot zone. The single-crystal YAG pushrods are grown using Czochralski method by II-VI Optical Systems, Inc. The pushrods are mounted in custom-built stainless steel holders, which are gripped in upper and lower water-cooled hydraulic wedge grips. The single crystal YAG pushrods are physically separated from the HfB_2 test specimen by Al_2O_3 spacers with platinum (Pt) foil separating the pushrods from the alumina spacers, later replaced with sapphire spacers.

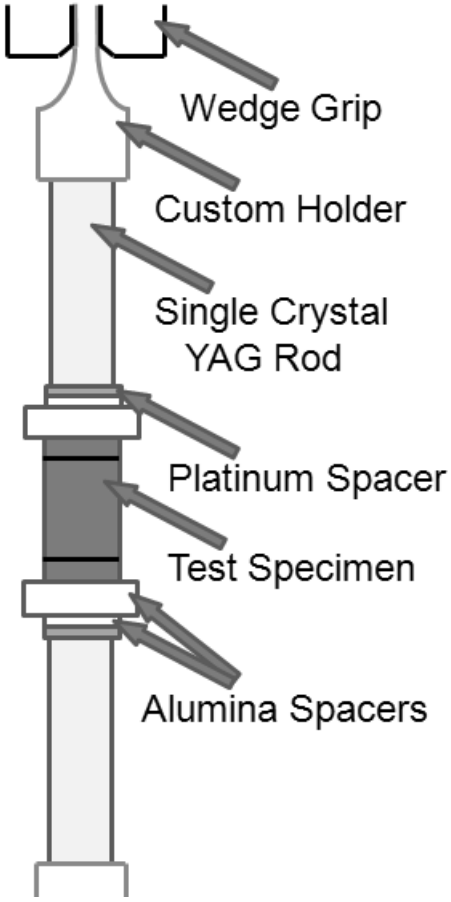

Figure 13. A schematic showing a UHTC specimen gripped in preparation for compression test. eproduced from DeGregoria [17]

The custom holder was initially used by Armani [19] for compression testing of small YAG specimens at 1300°C. The custom holder designed by Armani was a split wedge with setscrews. However the setscrews prevented sufficient thermal expansion of the holder at 1500°C, resulting in cracked YAG pushrods [17]. DeGregoria temporarily resolved this issue by operating without the setscrews. However, during the course of this research, it became apparent that a more permanent solution was necessary. A new set of custom holders was designed that allows for thermal expansion of both the

YAG pushrod and the 303 stainless steel custom holders [20, 21]. The new design incorporates a split holder, over-bored by 0.2 mm, held together with silver plated screws to prevent binding along with spring washers that allow the removable half to expand by 0.15 mm. Figure 14 shows the old wedge style YAG pushrod holder along with the new split style design. The new design of the stainless steel holders allows for easy removal of YAG pushrods even in cases where the rods have broken during the test. Prior to gripping in custom holders the YAG pushrods are wrapped in copper foil to evenly distribute the pressure of the custom pushrod holders.

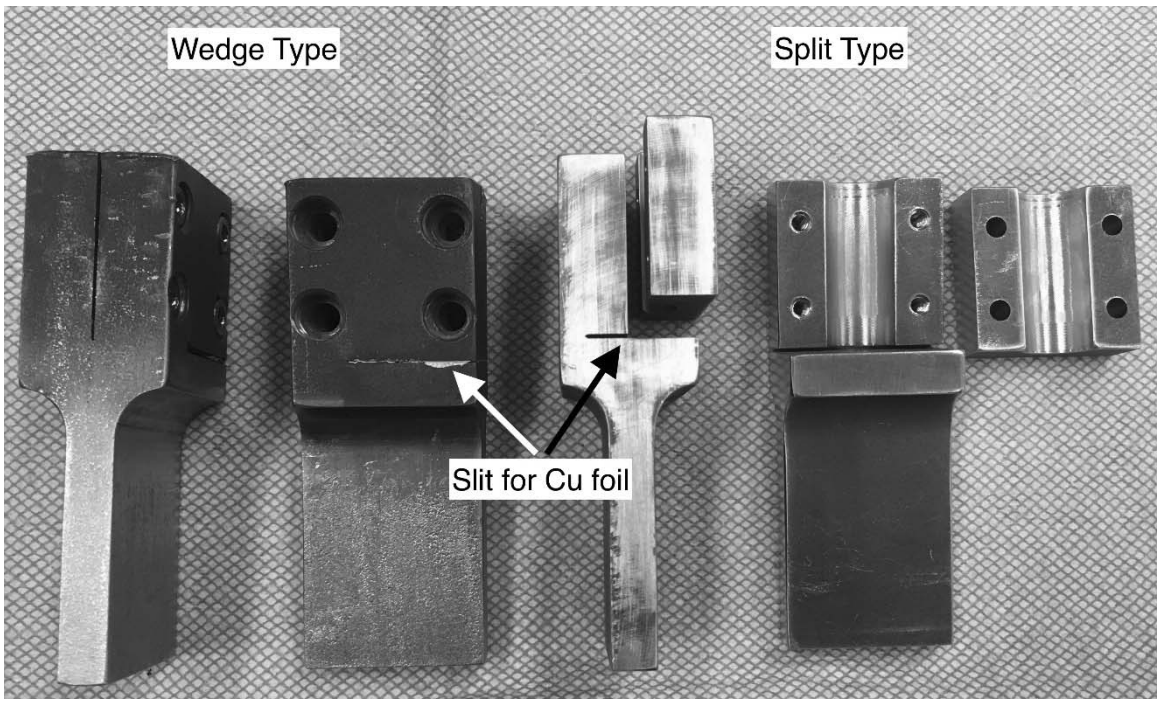

Figure 14. Custom Stainless Steel Holders, Old Design (left) and New Design (right).

One of the objectives of this work was to evaluate the efficacy of replacing the alumina spacers with the sapphire spacers to permit compression creep tests at higher

creep load and to extend the creep test duration. Sapphire spacers with both random and c-plane orientation supplied by Swiss Jewel were used with dimensions of 12.7 mm. x 12.7 mm. x 6.35 mm. Two sapphire spacers were used to separate each YAG pushrod from the hafnium diboride test specimen. Platinum foil separates the YAG rod from the sapphire spacer to minimize adhesion. As described in Section 1.4, one objective of this research is to evaluate the usefulness of sapphire spacers for compression creep testing of small HfB_2 specimens with compression creep stresses above 50 MPa.

With only the custom holders being held by the MTS wedge grips, the rest of the load train must be precisely aligned for successful compressive testing. Misalignment causes uneven loading of the specimen and can result in a premature failure of the specimen or the YAG pushrods. An alignment tool was printed on an Objet 3-D printer using VeroGray material to preposition the platinum foil, sapphire spacers and hafnium diboride specimen for insertion between the YAG rods. Figure 15 shows the custom alignment tool encasing the YAG rods, Pt foil, sapphire spacers and the test specimen. Figure 16 demonstrates the utility of using the alignment tool to pre-position the hydraulic ram to facility the installation of the spacers and specimen.

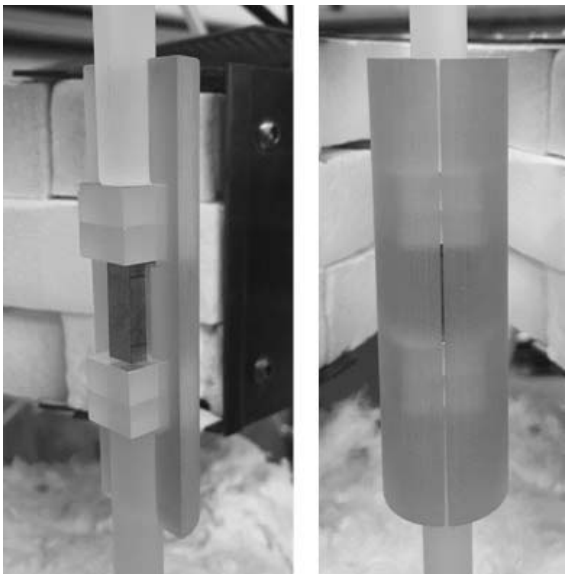

Figure 15. Custom Load Train Alignment Tool, Open (Left) Closed (Right)

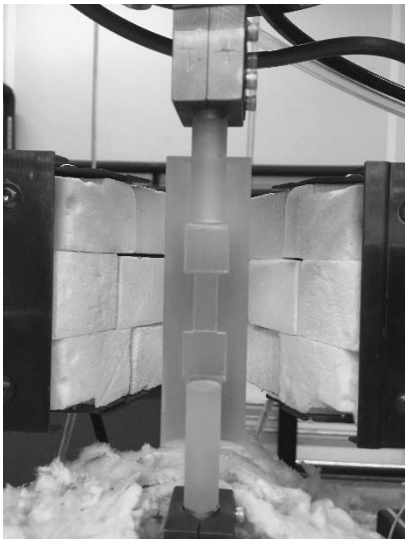

Figure 16. Using Alignment Tool to Determine Initial YAG Spacing

3.4 Test Procedure

The test procedure detailed here is based on prior work by DeGregoria [17]. The test procedure was adapted for the changes and refinements made during the course of this research. Prior to creep testing, accurate temperature calibration was necessary to ensure the specimen was tested at the desired temperature. Accomplishing temperature

calibration involved progressing the “Heat” portion of the test procedure, stopping short of “Load.” Temperature calibration was performed approximately ten times in order to optimize the amount of insulation and identify the furnace temperature set point to ensure the specimen was at the desired test temperature.

The temperature calibration involved soaking a sacrificial HfB_2 specimen at target temperature for a minimum of one hour prior to probing the surface of the specimen with a B-type thermocouple. Temperature readings were then displayed on a Eurotherm 2216e unit and recorded in a laboratory notebook. Multiple furnace set points between 1500-1560°C were explored. Finally, 1515°C was selected as the optimum setting to achieve 1500°C on the surface of the test specimen. It must be noted that during temperature calibration specimen surface temperatures could vary ~10°C depending on the probing location. Because the variation of ~10°C represents less than 1% of the test temperature, it was deemed negligible. In all tests, a specimen was heated to test temperature at the rate of 0.5°C/s, and held at test temperature for at least 1 h prior to loading.

The MTS configuration file developed by DeGregoria [17] was used in this work. This file is identified as “Temperature.cfg” in the test procedure in Appendix B. However, the procedure “Creep.000” developed by DeGregoria was modified to include a fully automatic shutdown that incorporates (1) full unloading of the test specimen and (2) furnace shutdown. Note that the procedure used by DeGregoria reduced the load to zero but did not shut down the furnace. The test procedure also mandated that the following data be collected at fixed time intervals: time (s), strain (m/m), displacement (mm), force (N), force command (N), temperature (°C) and temperature command (°C). During the creep portion of the test a data point was recorded every second for the first

24 h and every 10 s during hours 24-72 of the test. In all creep tests the specimen was loaded to creep load at the rate of 0.5 MPa/s. Upon completion of the creep test, the specimen was unloaded to zero load at the same rate. The full test procedure is detailed in Appendix B.

3.5 Microstructural Examination Procedure

Upon completion of high temperature creep testing, the specimens are first examined with an optical microscope to gain a preliminary understanding of the exterior condition of the specimen. Examination under optical microscope can set the framework for analysis with an SEM. The optical microscope used for this research was a Zeiss Discovery V12 with SteREO running AxioVision (AxioVs40 V 4.8.2.0). While image transmission to a computer monitor was the chief analysis technique, the stereo feature allowed for depth of field permitting the researcher to better understand the specimen. When optical imaging was complete, the specimen must be prepared for examination with an SEM.

3.5.1 Sample Preparation for Examination Under SEM

In preparation for examination with an SEM, specimens were mounted in epoxy resin prior to sectioning to ensure the oxide layer remained intact. The specimens were mounted in a two-stage epoxy by a ratio of two parts EpoThin 2 Expoxy Resin (20-3440-128) to one part EpoThin 2 Epoxy Hardener (20-3442-064). Molds of 1-in. diameter were swathed with a release agent prior to placing the specimen into the empty mold. The epoxy mixture was gently stirred to prevent the formation of air bubbles and poured into the mold containing the specimen. The mold was then placed under a partial vacuum of

10 psi (absolute) for 10 min. to remove unwanted air bubbles in the epoxy. The entire assembly was left overnight to cure.

The samples were then labeled and sectioned using an Isomet 1000 saw along the plane normal to the specimen axis (also the direction of compressive load). For the brittle UHTC, a low concentration diamond blade was used at a rotation speed of 275 RPM and a force of 100 g. The monolithic HfB_2 required significantly less time to cut while the SiC containing samples took several hours, with routine blade sharpening by use of a dressing stick.

Polishing of the samples was done with a Buehler AutoMet 250 polisher using an EcoMet 300 controller. Table 3 outlines the steps used to polish the specimens to a 0.25 μm mirror finish.

Table 3. Polishing Steps

	Surface	**Grit Size**	**Time**	**Spin Type**	**Base Speed**	**Head Speed**	**Pressure**
1	Piano DGD	220	1:00 min increments, until Planar-grinding step is achieved.	Complementary	300 rpm	50 rpm	10 lbs
2	Piano DGD	500	5:00 min	Complementary	150 rpm	50 rpm	8 lbs
3	Piano DGD	1200	5:00 min	Complementary	150 rpm	50 rpm	8 lbs
4	Piano DGD	2000	4:00 min	Complementary	150 rpm	50 rpm	8 lbs
5	Piano DGD	4000	3:00 min	Complementary	150 rpm	50 rpm	8 lbs
6	VerduTex	1μm	3:00 min	Contra	150 rpm	50 rpm	8 lbs
7	VerduTex	0.25μm	3:00 min	Contra	150rpm	50rpm	8lbs

The identification of planar grinding was achieved using a bottom lit optical microscope. This optical microscope enabled the verification of each polishing step. It was critical to ensure that polishing was uniform. A non-uniform finish results in varying focal points and degraded resolution quality depending on the location within the sample. To ensure debris-free transitions, samples were cleaned in an ultrasonic alcohol bath for 30 s and dried with nitrogen gas between polishing steps. Cleaning and meticulous glove usage was especially important upon completion of step 7 in Table 3.

After polishing all specimens to a 0.25 μm finish, copper tape was installed, wrapping from the face of the mounted sample to the back as shown in Figure 17. After the addition of copper tape an iridium sputter coating was applied using a Denton Vacuum Desk IV sputter coating machine. The sputter coating and copper tape reduce charging effects from the SEM and their addition to the specimens concluded the required sample preparation for SEM analysis.

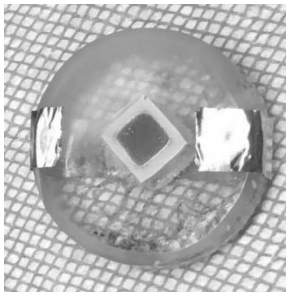

Figure 17. HfB_2 Specimen Prepared for Examination with an SEM

3.5.2 Microstructural Examination of Specimen with an SEM

Detailed analysis of the oxide layer requires a multi-tier approach. Images are used to identify the oxide thickness and its multi-layer nature as described in Section 2.4.

However gray scale images alone produce inconclusive information and must be corroborated with composition analysis. Elemental composition is determined via energy-dispersive X-ray spectroscopy (EDS). The EDS capabilities available at AFRL/RXCC are more sensitive and are able to detect lighter elements such as carbon or boron when compared to the EDS capabilities available at AFIT. All EDS in this effort was performed at AFRL on a FEI Quanta 650 with an EDAX Octane Super 60mm^2 detector. A combination of line, area and point scans gathered a complete picture of the elemental makeup of the samples.

A principal objective of oxidation analysis involves the measurement of the oxide layer in the SEM images of the oxidized material. All images used in oxidation analysis in this work were generated using AFIT's FEI Quanta 450 SEM, which readily achieves the required 1-micron resolution. Images were taken such that the entire oxide thickness was identifiable in the micrograph. For the monolithic HfB_2, this task required only approximately 80x magnification, whereas the analysis of the HfB_2-SiC specimens required images produced under more than 2000x magnification. For each specimen, SEM images were then taken across the perimeter of the specimen for the evaluation of the oxide scale thicknesses.

IV. Results and Analysis

Five compression creep tests were performed in this work using the methodology described in Section III. A summary of the test conditions is provided in Table 4.

Table 4. Summary of compression creep tests performed at 1500°C in air in this work

Specimen	Composition	Compressive Stress (MPa)	Test Duration (h)
HfB2-0SiC-2	HfB_2	75	20
HfB2-0SiC-3	HfB_2	75	30
HfB2-10SiC-4	HfB_2 - 10 vol% SiC	100	0
HfB2-10SiC-5	HfB_2 - 10 vol% SiC	75	66.3
HfB2-30SiC-3	HfB_2 - 30 vol% SiC	100	8.8

4.1 Compression creep test summary

As mentioned in Section 2.5, DeGregoria [17] was unable to achieve compressive loads higher than 50 MPa for any significant duration due to the failure of alumina spacers. Hence this research focused on the replacement of alumina spacers with sapphire spacers. With that goal in mind, the first test using sapphire spacers was performed at a compressive creep stress of 75 MPa. All test results are summarized in Figure 18 along with previous test data from Winder [12] and DeGregoria [17].

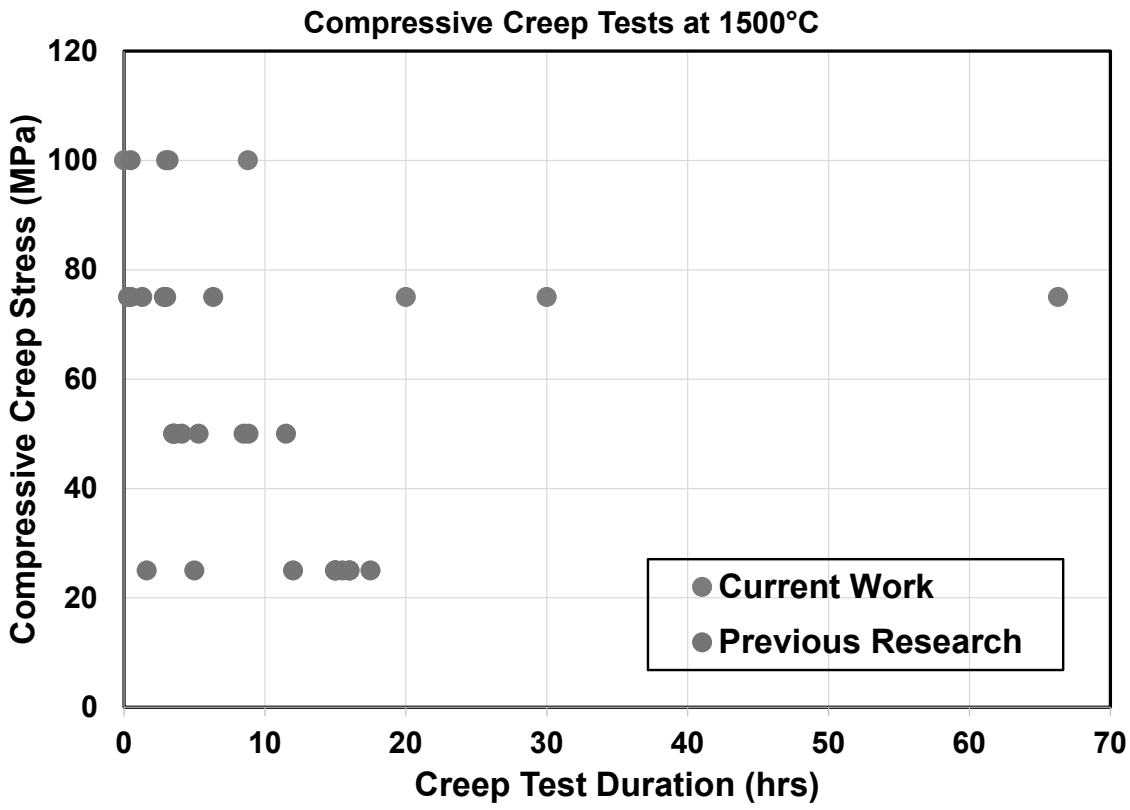

Figure 18. Summary of Compressive Creep Tests Performed at 1500°C in Air: Creep Stress vs. Test Duration

Prior to this effort, the longest compression creep test duration achieved at 75MPa at 1500°C in air at AFIT was 6.3 hours. Recall that those tests had to be terminated due to failure of alumina spacers included in the load train [12, 17]. In this work, a successful 75 MPa compression creep test lasted 66.3 h. Furthermore, failure of test specimen, sapphire spacers or the YAG pushrods did not occur when this test was terminated. While this test indicates that sapphire spacers facilitate longer test durations at higher compressive loads. All four sapphire spacers exhibited multiple cracks with the bottom two spacers showing more damage than the upper two. Additionally, there were visible depressions in the spacers where the test specimen was in contact with the spacer (see Figure 19). Post-test

inspection of the YAG pushrods revealed that the upper rod was undamaged while the lower rod had a slight chip at the interface with the custom pushrod holder. Note that custom holders of the original design proposed by Armani [19] were used in this test.

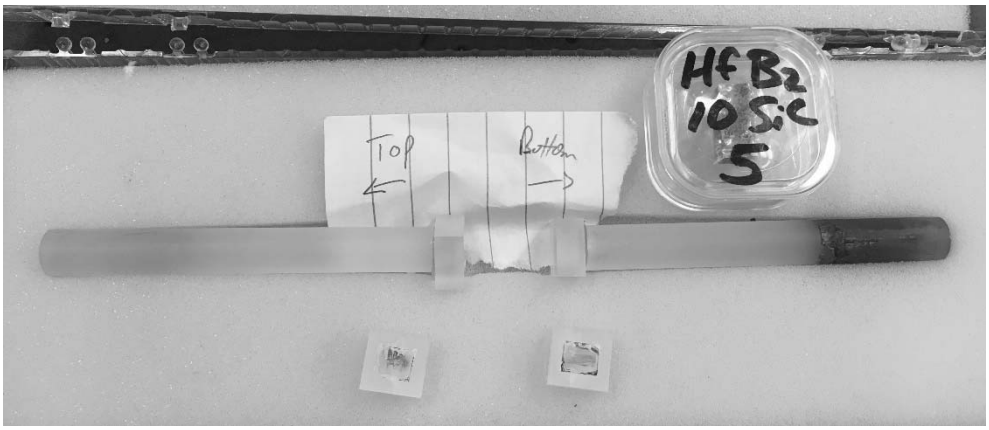

Figure 19. YAG Rods and Sapphire Spacers used in the 75 MPa compression creep test of 66-h duration. Note depressions in the sapphire spacers indicative of substantial superplastic deformation.

The next creep test was performed with compression creep stress of 100 MPa. In addition to providing creep data, this test aimed to explore the limitations of the load train. The expected test duration was ~72 h. The specimen was heated to 1500°C and allowed to soak at that test temperature for 1 h in accordance with the standard test procedure. However, when the test specimen was loaded in compression to 100 MPa, the load train suffered catastrophic failure. The lower two sapphire spacers shattered and the upper spacers cracked. The bottom YAG pushrod also split longitudinally, with the upper YAG rod remaining undamaged as shown in Figure 20. Catastrophic failure of the YAG pushrod in this test prompted the redesign of the pushrod holders as described in Section

3.3. The specimen itself also split longitudinally, though it is unclear which section of the load train failed first.

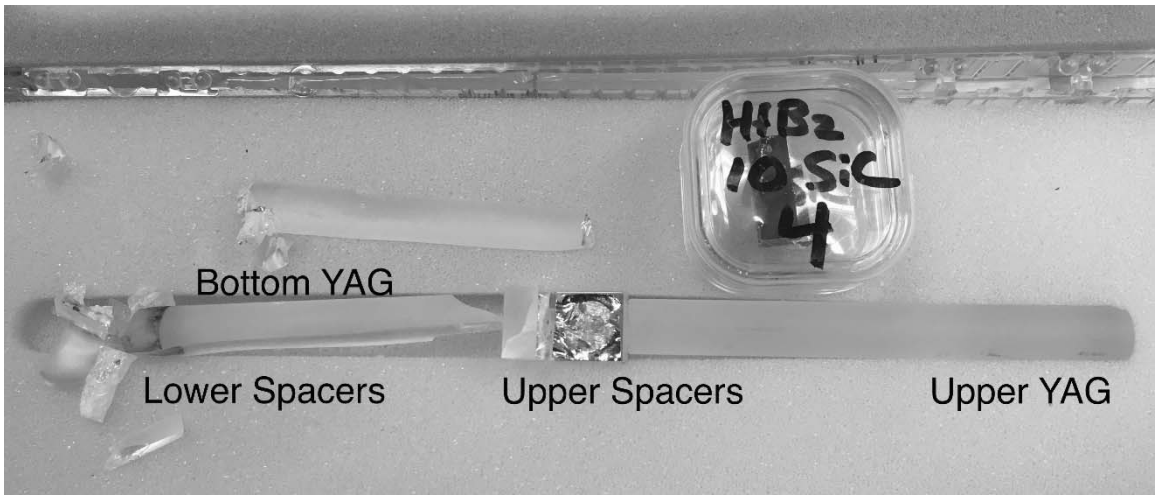

Figure 20. YAG Rods and Sapphire Spacers used in the 100 MPa compression creep test.

All subsequent tests were conducted with the YAG pushrod holders of new design. It is noteworthy that the re-designed pushrod holders reduced the breakage of YAG rods in addition to simplifying the removal of the pushrods from the holders .

After the failure of the load train in the 100 MPa compression creep test, two HfB_2 specimens were tested in compression at 75 MPa. Failure of test specimens did not occur when these tests were terminated after 20 and 30 h of creep. Post-test inspection revealed no damage to the YAG pushrods.

A HfB_2-30 vol% SiC test specimen was tested in creep with a compressive stress of 100 MPa. The re-designed YAG pushrod holders were used in this test. Notably, the load train survived the initial load up to 100 MPa. Moreover, the test lasted nearly 9 h and was terminated due to failure of a sapphire spacer.

Having successfully performed 75 MPa compression creep tests of 20-, 30- and 66-h durations and a 100 MPa compression creep test of nearly 9-h duration, we conclude that replacing alumina spacers with the sapphire spacers is indeed beneficial. Using sapphire spacers, we were able to perform compression creep tests of longer duration at compression creep stress levels above 50 MPa. However, failures of the sapphire spacers in the 100 MPa tests yielded important information regarding the sapphire spacers.

4.2 Sapphire Spacer Analysis

Depressions in the sapphire spacers, noted after compression creep tests at 1500°C in air are indicative of the localized super-plastic deformation of the sapphire. Recall that in these tests the strain measurement is accomplished by an extensometer which maintains direct contact with the HfB_2-SiC specimen. Hence, the excessive deformation of the sapphire spacers has no bearing on the creep strain data collected during these tests. Yet it is instructive to review the characteristics of the sapphire spacers used in this work.

Two types of sapphire spacers were utilized in this work: those with random crystallographic orientation and those with c-plane orientation. In this experimental study the sapphire spacers were selected at random. For example, four sapphire spacers with random crystallographic orientation were used in the 75 MPa creep test of 66.3 h-duration (specimen HfB_2-10SiC-5). Conversely, four spacers with c-plane orientation were used in the 100 MPa creep test that failed upon load-up (specimen HfB_2-10SiC-4). The 75 MPa creep tests of 20-h and 30-h duration on HfB_2 specimens (specimens HfB_2-0SiC-2 and HfB_2-0SiC-3, respectively) both utilized four random orientation spacers.

Post-examination revealed that in all four tests, the bottom two spacers suffered more damage than upper spacers. Note that the 100 MPa compression creep test of 8.8-h duration (specimen HfB_2-30SiC-3) utilized three spacers with random crystallographic orientation and one spacer with a c-plane orientation. Although the single spacer with the c-plane orientation used in this test occupied the uppermost position in the load train, this was the spacer that failed. This result suggests that spacers with c-plane orientation were weaker than those with random crystallographic orientation.

Current literature devoted to mechanical properties of sapphire documents bulk compressive properties, but does not provide compressive properties for specific crystallographic orientations. In contrast, tensile properties of sapphire with specific crystallographic orientations are presented. According to Fischer *et. al*. [22], the tensile strength of sapphire is strongly dependent on temperature. While the crystals with c-plane orientations (plane normal to the c-axis, tension directed along the c-axis) are stronger in tension at room temperature, they have significantly lower tensile strength at 1400°C than the crystals with a-plane orientation (plane normal to the a-axis, tension directed along the a-axis) and those with m-plane orientation (plane normal to the m-axis, tension directed along the m-axis) [22]. Based on these observations it is recommended that sapphire spacers with random crystallographic orientation or spacers with a-plane and m-plane orientations be used in future tests.

4.3 Oxidation of HfB_2 and HfB_2-SiC Under Compressive Stress at 1500°C in Air

Results of this study offer some insight into oxidation behavior of HfB_2, HfB_2-10 vol% SiC and HfB_2-30 vol% SiC at 1500°C under compressive stress. Following

mechanical testing all specimens were mounted, sectioned and polished for examination with the SEM and EDS as described in Section 3.5.2. Typical SEM images of the oxide scales formed on the surface of the HfB_2 and HfB_2-SiC specimens tested in this work are presented in Figures 21, 22, 24, 25 and 29. For each specimen the thickness of the oxide scale was measured in 140-200 locations and the average value of the scale thickness was calculated. Winder and DeGregoria [12, 17] commented that oxidation behavior of the HfB_2 and HfB_2-SiC appeared to be markedly different near the corners of the specimen section and further complicated by corner cracks in the oxide layer. Therefore in this work, measurements of the oxide layer thickness taken at and near the corners were not included in calculating the average value of the scale thickness. In SiC containing specimens the scale thickness measurement includes glass, metal oxide, and SiC-depleted regions when present. The average values of the oxide scale thickness obtained in this work are summarized in Table 5. Note that the results in Table 5 are correlated with the creep time, (i.e. time under sustained compressive stress), which does not include the 1-h soak at test temperature prior to loading. It should be noted that the testing of specimen HfB_2-10SiC-4 was not included in the summary of oxidation results due to spacer failure upon load-up. While the specimen experienced the target temperature for one hour under compressive creep stress of approximately 8 MPa, it should not be directly compared to the stressed oxidation results of the other tests.

Table 5. Summary of Oxidation at 1500 °C in air under compressive stress.

Specimen	Creep Stress (MPa)	Creep Duration (h)	Average Scale Thickness (μm)	Standard Deviation	Number of Measurements	Min Thickness (μm)	Max Thickness (μm)
HfB2-0SiC-2	75	20	814	102	204	620	1050
HfB2-0SiC-3	75	30	1171	136	141	910	1440
HfB2-10SiC-5	75	66.3	210	52	140	114	368
HfB2-30SiC-3	100	8.8	37	28	178	12.5	120

Figure 21 presents an SEM micrograph of the HfB_2 specimen subjected to 20 h of compression creep at 75 MPa at 1500°C in air. The SEM image in Figure 21 clearly shows two distinct regions: unoxidized HfB_2 and HfO_2 scale. The EDS line analysis further confirms the existence of these two distinct regions. Hafnium and boron are observed in the unoxidized parent material. Hafnium and oxygen are detected in the hafnia scale (HfO_2). It is recognized that due to its lightness, detection of boron with EDS is difficult. Hence, the boria filling the columnar channels in the HfO_2 oxide layer is not readily detected. Also note that SEM sample preparation was not optimized to preserve the delicate traces of boria in the HfO_2 oxide layer.

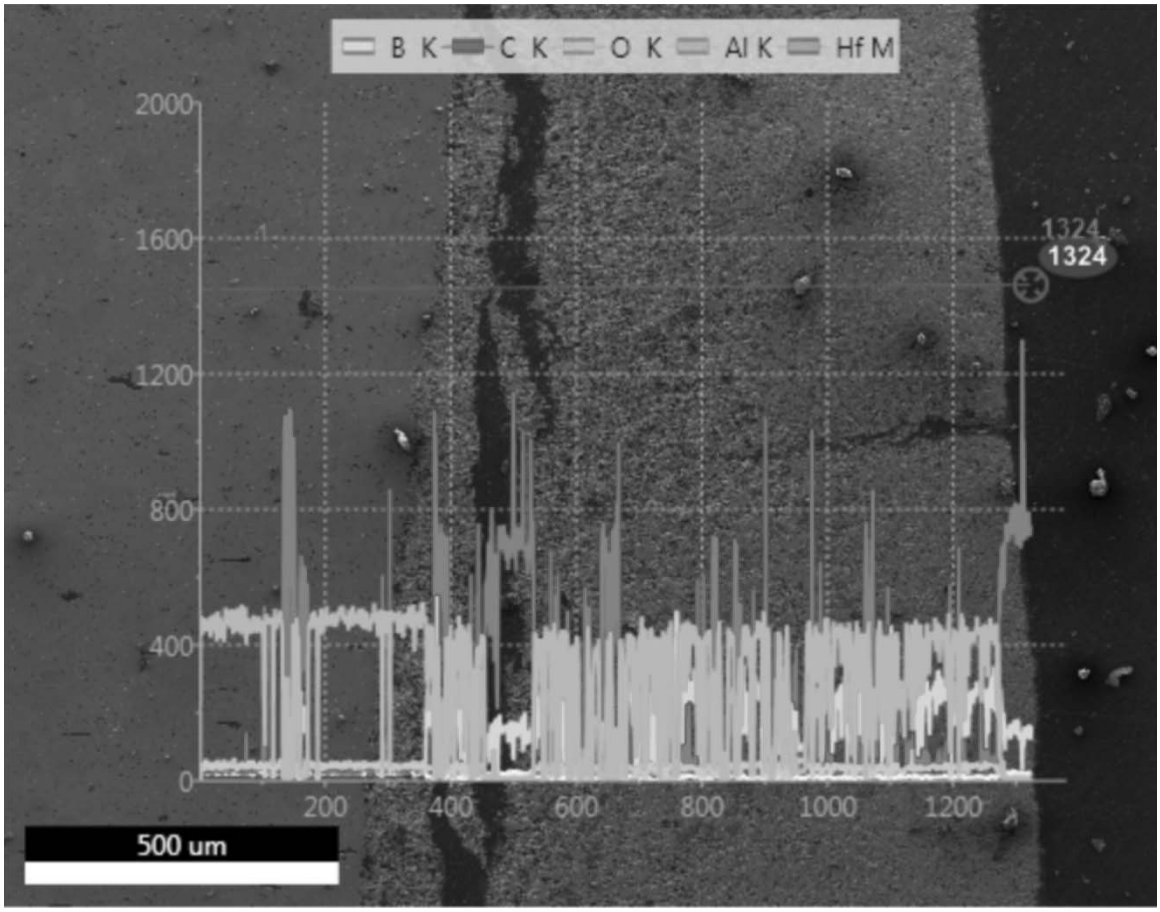

Figure 21. Cross-sectional SEM micrograph of the HfB_2 specimen subjected to 20 h of compression creep at 75 MPa at 1500°C in air. Note the two distinct regions: unoxidized HfB_2 and HfO_2 scale. The EDS line analysis shows presence of (i) Hf and B in the unoxidized HfB_2, of (ii) Hf and O in the HfO_2 scale.

Figure 22 presents an SEM micrograph of the HfB_2-30 vol% SiC specimen subjected to 8.8 h of compression creep at 100 MPa at 1500°C in air. The SEM image in Figure 22 clearly shows three distinct oxide scale regions: I – B_2O_3+SiO_2 (borosilicate glass), region II - HfO_2 with SiO_2 infusion and region III – HfO_2 with Si-O-C. The EDS line analysis confirms the existence of these three distinct regions. Silicon and oxygen are observed in the glassy region (primarily SiO_2, region I in Figure 22). Hafnium and

oxygen are detected in the hafnium oxide (HfO_2) scale (region II in Figure 22). Hafnium, oxygen and silicon are observed traces of carbon indicating HfO_2 scale with Si-O-C (region III in Figure 22). It is recognized that due to its lightness, detection of born with EDS is difficult. Hence, we do not readily detect boron in the glassy layer. Yet we presume that glassy layer formed on the specimen surface is indeed borosilicate glass (B_2O_3+SiO_2).

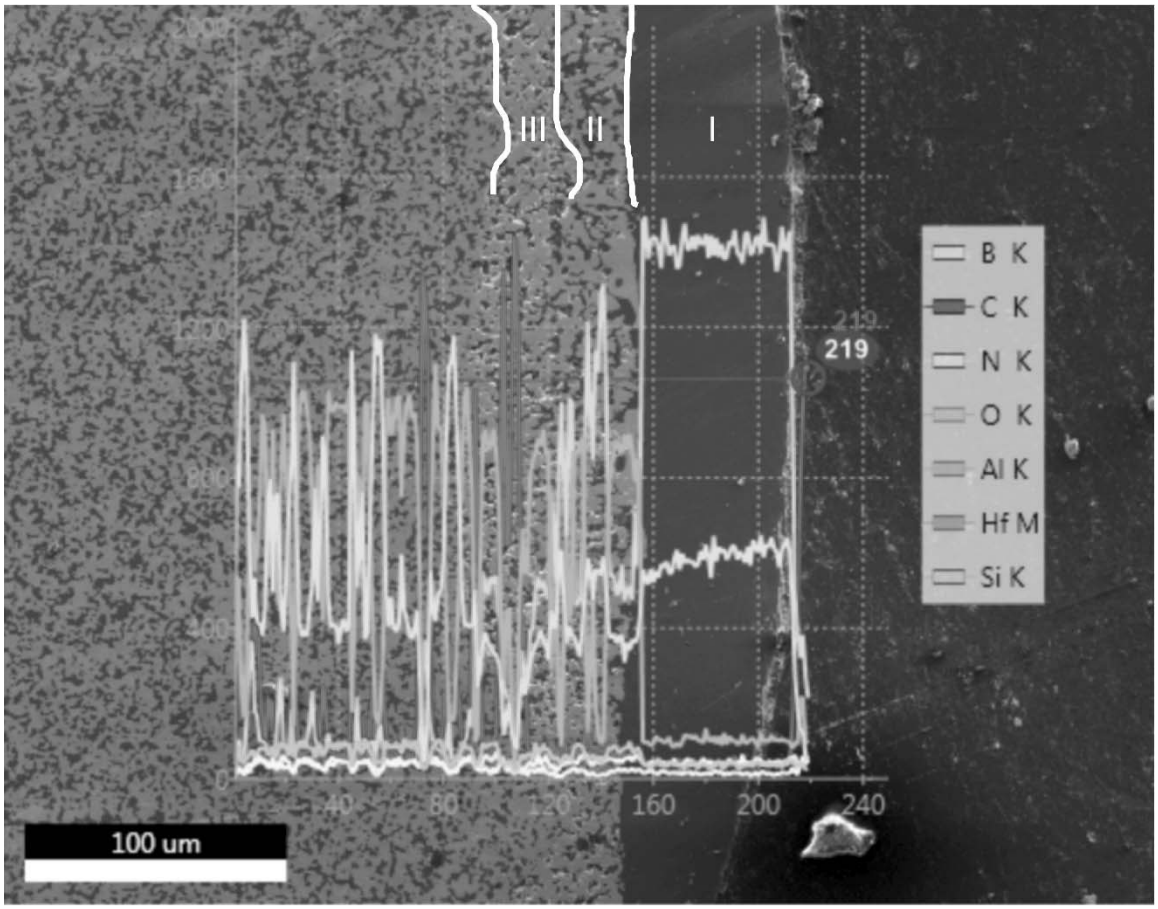

Figure 22. Cross-sectional SEM micrograph of the HfB_2-30 vol% SiC specimen subjected to 8.8 h of compression creep at 100 MPa at 1500°C in air. Note three distinct regions: I - (presumably) borosilicate glass, II - HfO_2-SiO_2 and III –.HfO_2 with Si-O-C inclusions. The EDS line analysis shows presence of (I) Si and O in the borosilicate glass, of (II) Hf, O and Si in the HfO_2-SiO_2 scale, and (III) Hf and O in the HfO_2 layer.

While the boundaries of the unoxidized HfB_2 and of the HfO_2 scale are readily discernible in the SEM micrograph of the HfB_2 specimen in Figure 21, it is more difficult to identify boundaries between different regions in the oxidized HfB_2-SiC specimens. The EDS line analysis was extremely useful in determining the regional boundaries of the various oxide layers. The borosilicate glass that forms on the surface of HfB_2-SiC specimens is not uniform and has numerous cracks making it difficult for the mounting epoxy to adhere to the outermost surface layer, sometimes resulting in a gap between the outermost surface layer and the rest of the sample. This gap, when viewed in an SEM, charges and shows as a bright surface. It is important to confirm with the EDS analysis that this brightness in the SEM image is indeed a gap and not a part of the oxidized sample.

In addition to the difficulty in finding the edge of the oxide scale in specimens with SiC additives, the presence of the SiC-depleted layer can be elusive to detect. The SiC-depleted layer is not readily confirmed via EDS due to the small amount of SiC. Only by observing a general reduction in the distribution of SiC particles can we identify the approximate boundaries of the SiC-depleted layer. In some instances, the SiC-depleted layer is readily apparent, whereas in others it is not. Shugart *et. al.* documented SiC grain removal from sections of ZrO_2 during polishing and the presence of carbon in samples when mounted in epoxy, creating the potential for mistaken SiC depletion [24]. While the removal of SiC grains from the prepared specimen during polishing certainly contributes to the overall appearance SiC depletion, the limited SiC distribution of SiC concentration in portions of the HfB_2-SiC parent material clearly reflects SiC depletion. DeGregoria [17] identified SiC depletion in only one of his samples, a HfB_2-20% SiC

sample oxidized at 1500°C for 5 h. DeGregoria did not report observing SiC depletion in any other tests, not even in the 90-hr baseline oxidation test performed in a box furnace. As described in Section II, Carney documented the active oxidation of Si in HfB_2-20% SiC specimens by identifying of a Si-O-C inclusion zone, including the partial depletion of SiC at 1500°C [25]. Figure 23 shows a multi-zonal oxidation layer reported by Carney for a HfB_2-20% SiC specimen heat treated at 1800°C.

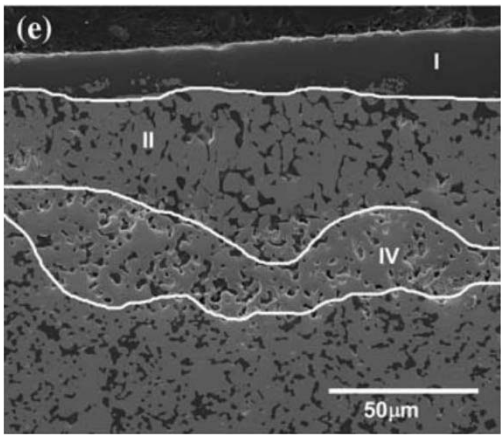

Figure 23. Oxidation of HfB_2-20% SiC at 1800°C (I: SiO_2, II: SiO_2 filled HfO_2, IV: HfB_2 with Si-O-C Inclusions and SiO_2 Filling), reproduced from [25] with permission from Springer.

Figure 24 identifies SiC depletion in specimen HfB_2-10SiC-5 as shown by EDS. Note the similarity of the identified zone IV in Figure 23 to zone IV in Figure 24, paying particular attention to the edge charging of the voids.

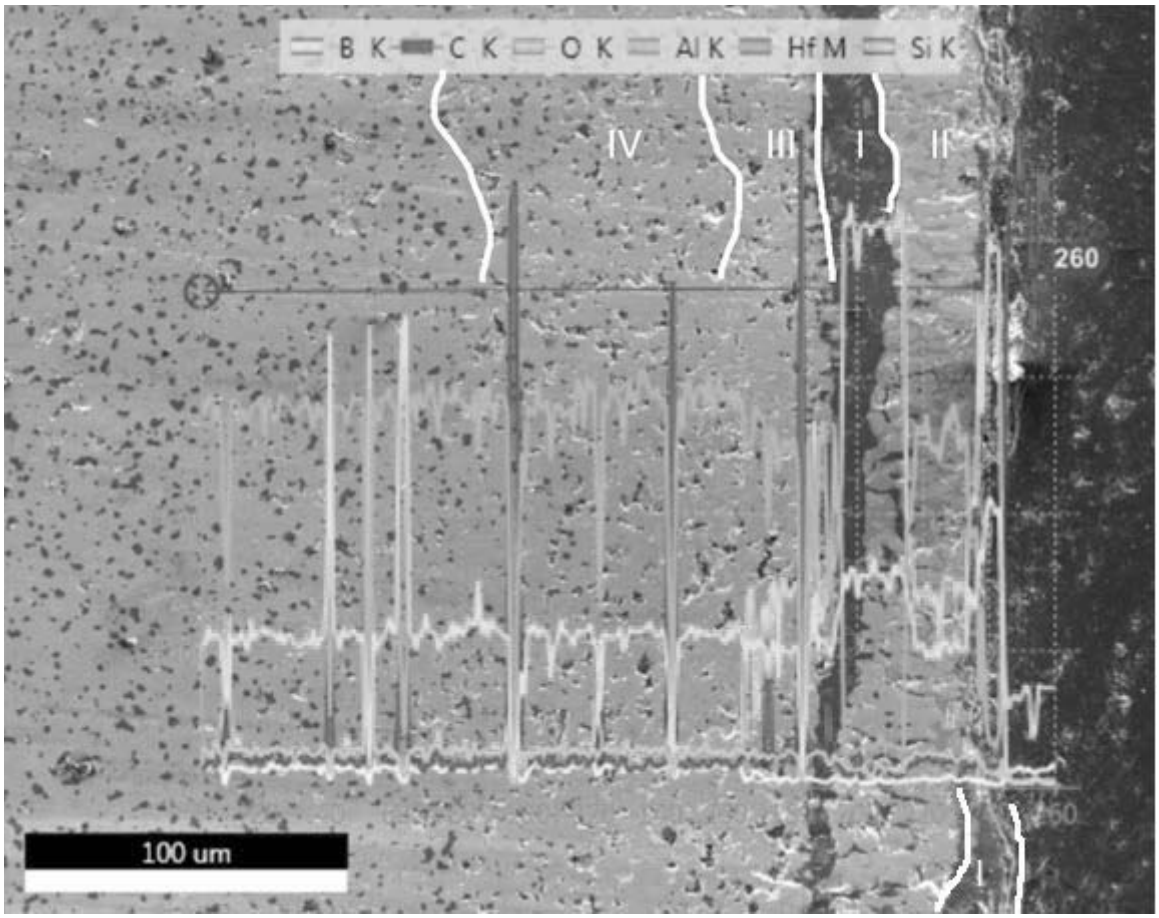

Figure 24. Cross-sectional SEM micrograph of the HfB_2-10 vol% SiC specimen subjected to 66.3 h of compression creep at 75 MPa at 1500°C in air. Note all four regions: I - borosilicate glass, II - HfO_2-SiO_2, III –.HfO_2 with Si-O-C inclusions and IV HfB_2 with Si-O-C inclusions (SiC depleted region). The EDS line analysis shows presence of (I) Si and O in the borosilicate glass, of (II) Hf, O and Si in the HfO_2-SiO_2 scale, and (III) Hf and O in the HfO_2 layer and (IV) Hf and Si with C and O inclusions in the HfB_2-SiC depleted region.

Note in Figure 24 the multi-zonal oxidation layers. Zone I represents the SiO_2 and B_2O_3, zone II represents HfO_2 with the columnar structure filled with SiO_2, zone III is HfO_2 with Si-O-C inclusions and zone IV is HfB_2 with intermixed Si-O-C inclusions along with SiO_2. In zone IV there are significant number of holes, darker than the otherwise grey spots representing SiC particles. These holes are the result of SiC depletion (active oxidation). In Figure 24, the region is identifiable by comparing the SiC

distribution of the parent material HfB_2-10% SiC at left to that in the depleted region IV. Simply, there are fewer dark spots in the depleted region than in the parent material and there are holes, distinguishable from SiC by carbon spikes on the EDS and slight charging at the edges. This is evident by the EDS data in Figures 25-28.

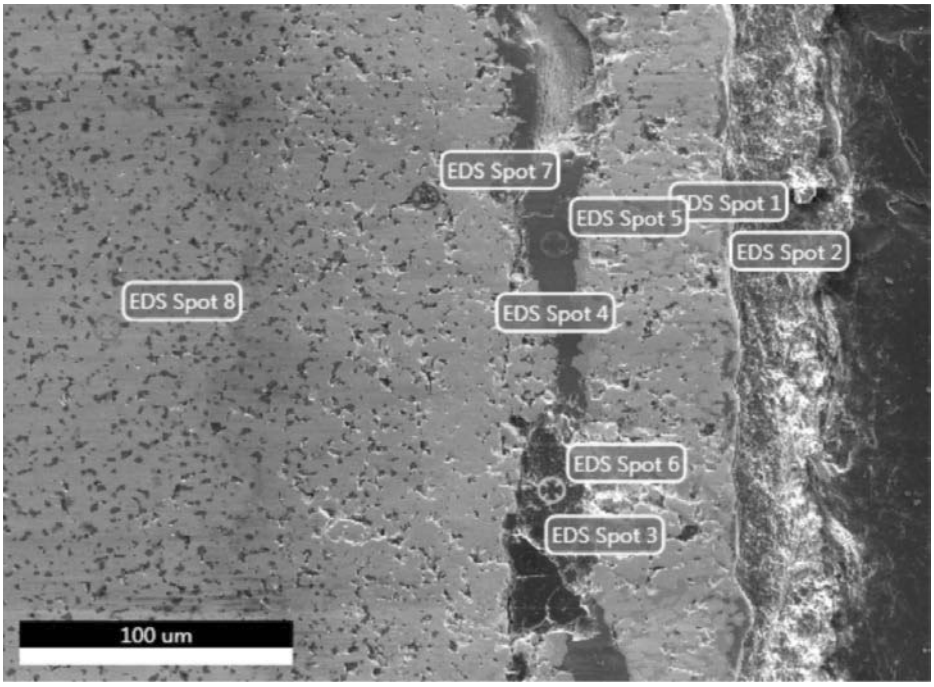

Figure 25. Cross-sectional SEM micrograph of the HfB_2-10 vol% SiC specimen subjected to 66.3 h of compression creep at 75 MPa at 1500°C in air. The EDS spot analysis confirms further refines the regions identified in Figure 24.

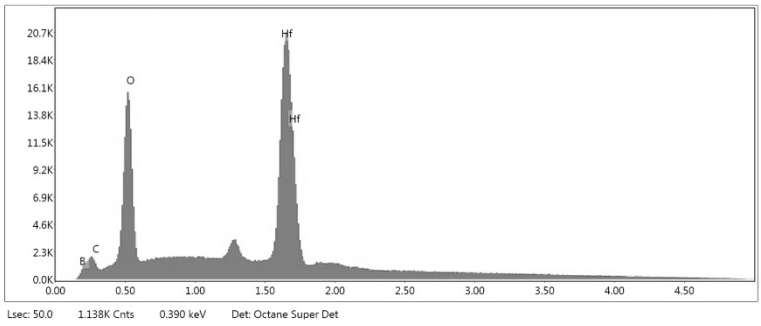

Figure 26. EDS spot analysis on cross-section of a HfB_2-10 vol% SiC specimen subjected to 66.3 h of compression creep at 75 MPa at 1500°C in air, spot 1 HfO_2

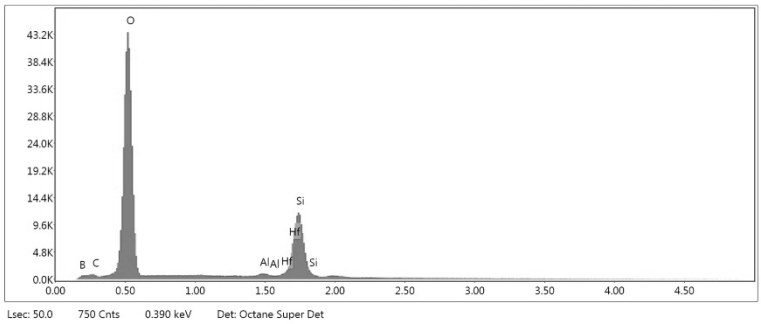

Figure 27. EDS spot analysis on cross-section of a HfB_2-10 vol% SiC specimen subjected to 66.3 h of compression creep at 75 MPa at 1500°C in air, spot 5 SiO_2+$B2O_3$

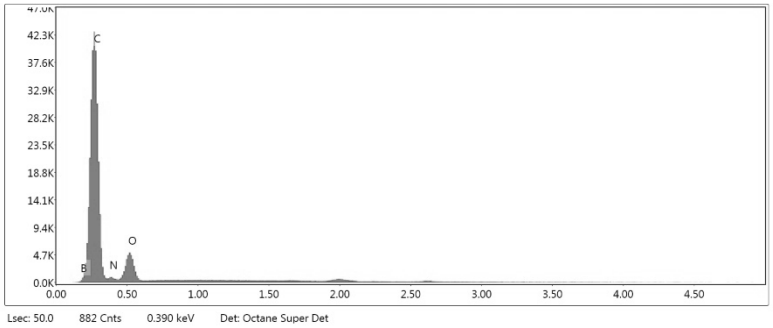

Figure 28. EDS spot analysis on cross-section of a HfB_2-10 vol% SiC specimen subjected to 66.3 h of compression creep at 75 MPa at 1500°C in air, spot 7 C

The EDS spot analysis confirms the information from the EDS line scan and further identifies the black marks as carbon, a result of active Si oxidation (one element to SiC depletion). For reference Figure 29 shows EDS data for silicon carbide particles and their corresponding micrograph.

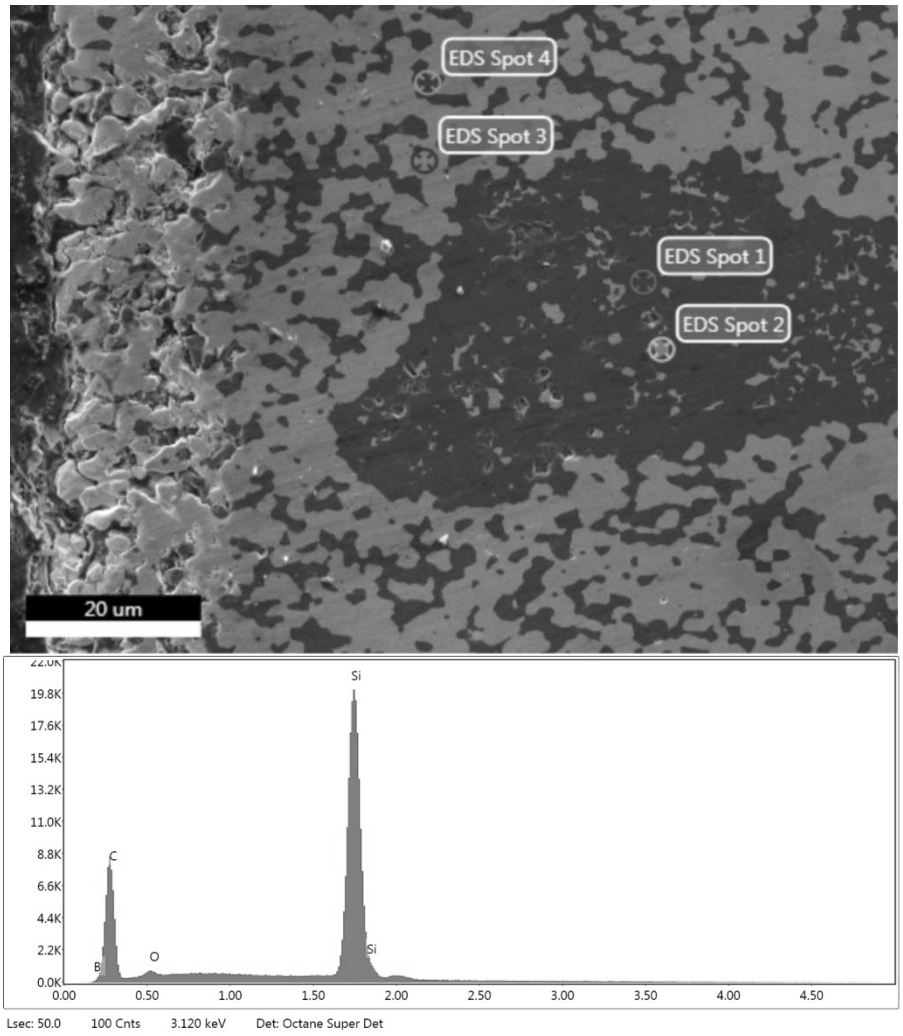

Figure 29. Cross-sectional SEM micrograph of the HfB_2-30 vol% SiC specimen subjected to 8.8 h of compression creep at 100 MPa at 1500°C in air. The EDS spot analysis identifies spot 1 as a SiC particle.

The average oxide thickness was plotted along with DeGregoria's [17] baseline oxidation results and Parthasarathy model [26, 27] as shown in Figure 30.

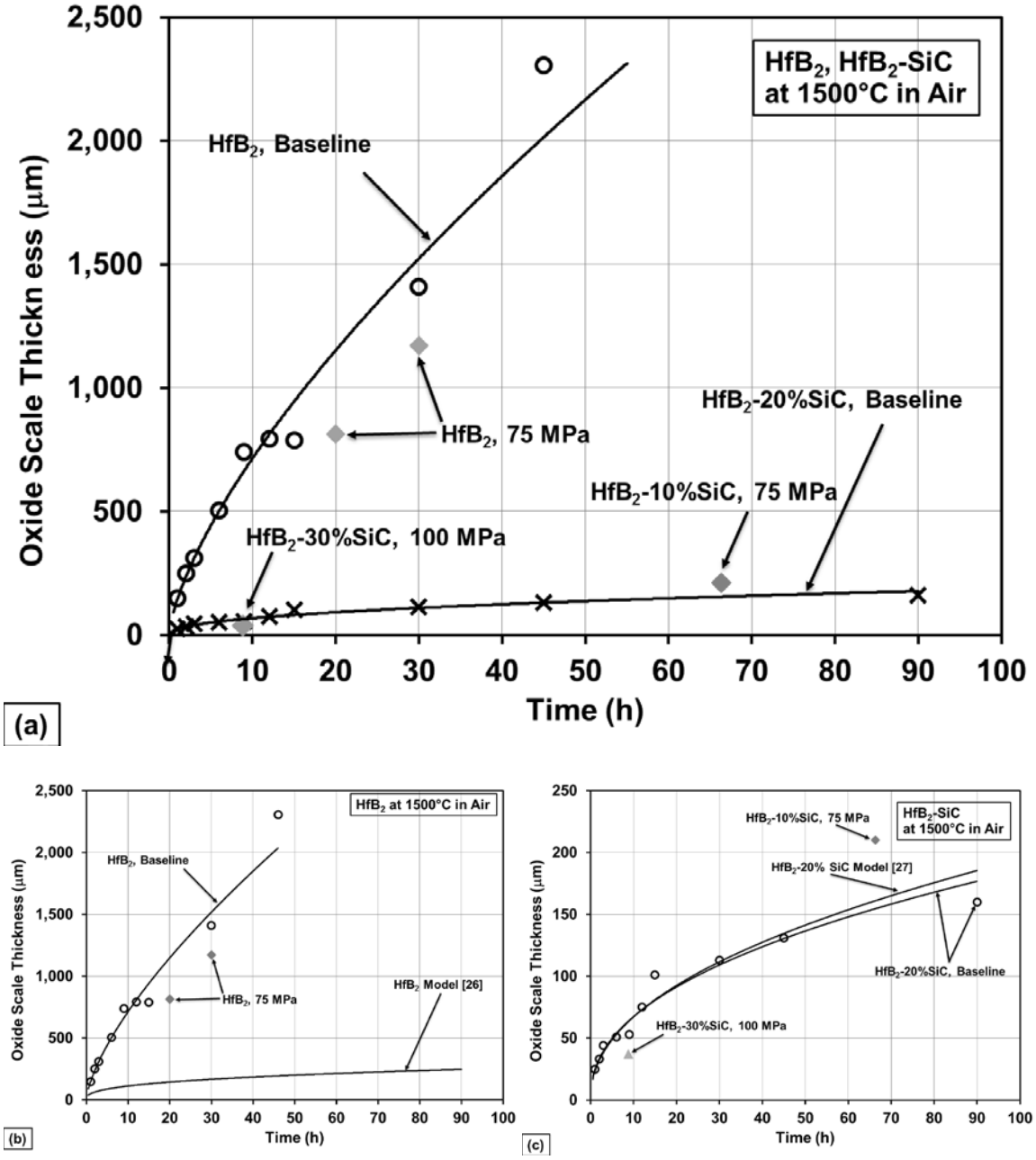

Figure 30. (a) Mean oxide scale thickness of HfB_2 and HfB_2-SiC stressed and unstressed specimens at 1500°C in air plotted against time in hours. (b) Mean oxide scale thickness of HfB_2 stressed, unstressed (baseline) and unstressed (model prediction) specimens at 1500°C in air plotted against time in hours. (c) Mean oxide scale thickness of HfB_2-SiC stressed, unstressed (baseline) and unstressed (model prediction) specimens at 1500°C in air plotted against time in hours. Unstressed data from DeGregoria box furnace testing [17], model of HfB_2 from Parthasarathy [26] and model of HfB_2-20% SiC from Parthasarathy [27].

The baseline results emanated from a box furnace test in which a single specimen subjected to 1500°C and 0MPa was sectioned at various exposure times. Using the same specimen for the duration of the test provide oxidation-time data with no specimen-to-specimen variance. Unfortunately, DeGregoria [17] only performed such a baseline evaluation on the monolithic HfB_2 and 20% SiC by volume.

In comparing the stressed monolithic specimen oxidation with the box furnace trendline, it is evident the data points fall outside the expected range. While possible the trendline lacks sufficient data points to provide definitive zero load results, the stressed samples are more than 3 standard deviations removed. It must be stated that DeGregoria's own unstressed 30hr specimen was one standard deviation from the trendline, thereby reducing the difference in stressed to unstressed to 2 standard deviations. Therefore it is possible the stressed oxidation results are two standard deviations lower than unstressed due to the closure of oxygen entry points assuming there are cracks present in the scale, or a decrease in the oxidation driving force due to compressive loads. With no historical oxidation results with which to compare, the results from tests HfB_2-10SiC-5 (10% SiC, 75MPa, 66.3 h, 1500°C) and HfB_2-30SiC-3 (30% SiC, 100MPa, 8.8 h, 1500°C) must be qualitatively compared to the 20% baseline.

Due to the reduction in oxidation susceptibility with the addition of SiC, it stands to reason that 10% SiC will have thicker oxide scale than 20% SiC which in turn will be thicker than 30% SiC. Taking a cursory look at Figure 30 confirms this theory with the 10% data point above the 20% baseline and 30% data point below. It should be noted the 20% baseline is a much better fit to DeGregoria's own data points than that of the monolithic.

The 30% data point is relatively near to the 20% baseline, within half of one standard deviation. However, with thin oxide layers and only one data point with which to compare to the baseline, it is not possible to correlate the two further than expecting the 30% oxide layer to be less than that of the 20% baseline. However with the 10% SiC, the fact the stressed oxidation thickness is two standard deviation lower than unstressed, one can postulate this is a result of the compressive loads. The closure of the extensometer groove as shown in Figure 31 highlights the 12.18% strain observed during the 66.3 h testing of specimen HfB_2-10SiC-5 at 75MPa.

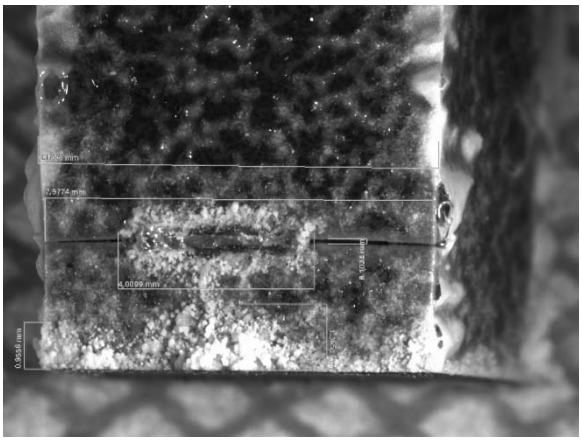

Figure 31. Optical micrograph of the lower extensometer groove, collapsed after 66.3 h 75MPa compressive load at 1500°C in air.

4.3.1 Anomalous Scale Surface Deposit

In both HfB_2 specimens, substantial scale buildup in proximity to the sapphire spacers was observed, as highlighted in Figure 32. Furthermore, a reddish discoloration of the scale was observed, that prompted EDS analysis.

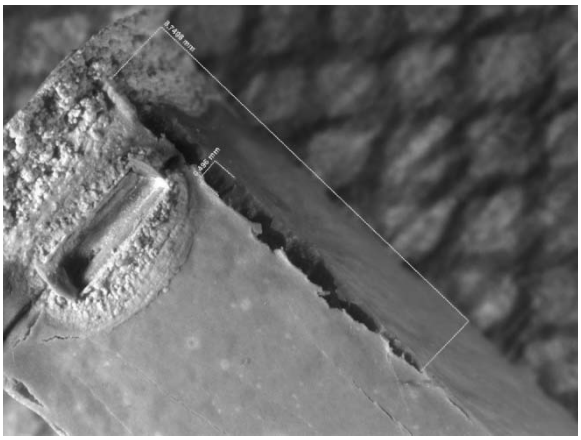

Figure 32. Optical micrograph of HfB_2 specimen after undergoing compression creep test of 75MPa for 20 h at 1500°C in air. Scale buildup and reddish hue near sapphire spacer contact.

Figure 33 highlights the longitudinal sectioning, in contrast to the other specimens sectioned laterally at the midpoint. Within Figure 33 are three distinct regions that formed the basis of the EDS analysis.

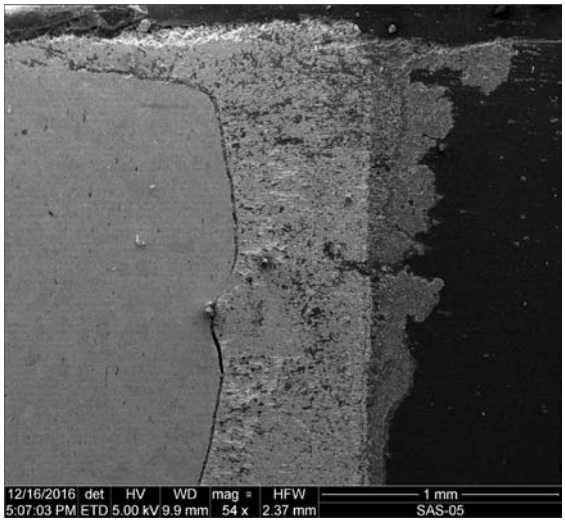

Figure 33. SEM micrograph of longitudinal section HfB_2 specimen after undergoing compression creep at 75MPa for 30 h at 1500°C in air. Top of specimen was in contact with sapphire spacer.

The composition analysis revealed the presence of aluminum in portions of the scale as seen in Figures 35- 38. Winder [23] observed similar reddish aluminum containing deposits during HfB_2 proximity testing to YAG in an alumina tube furnace as shown in Figure 34.

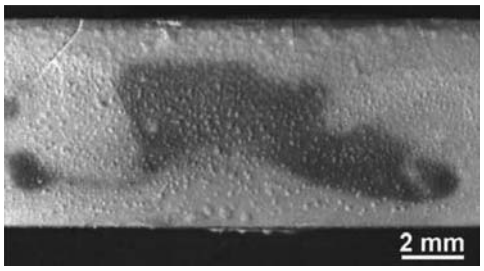

Figure 34. Optical micrograph of HfB_2 specimen oxidized in box furnace at 1500°C in air in close proximity to YAG in an alumina tube furnace. Reddish discoloration is a deposit containing aluminum, reproduced from Winder [23] with permission from Elsevier.

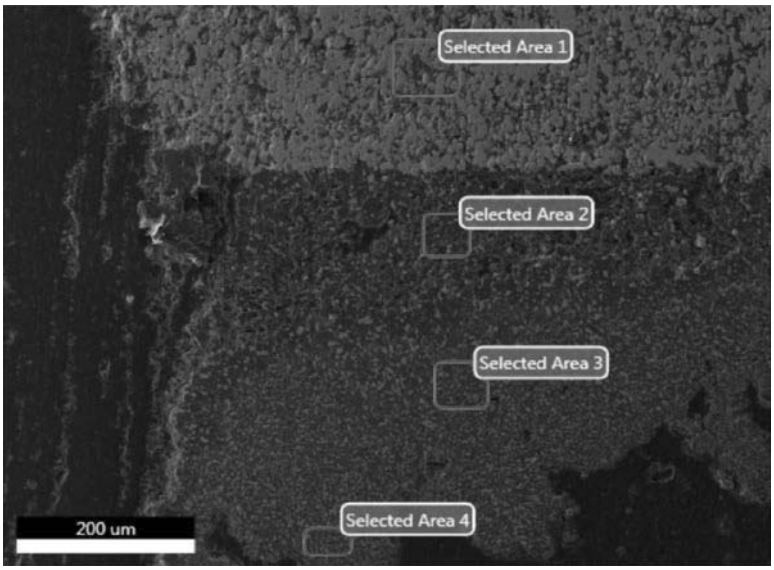

Figure 35. SEM micrograph depicting EDS area analysis of longitudinal sectioned HfB_2 specimen after undergoing compression creep at 75MPa for 30 h at 1500°C in air with left most portion of specimen in contact with sapphire (Al_2O_3) spacer.

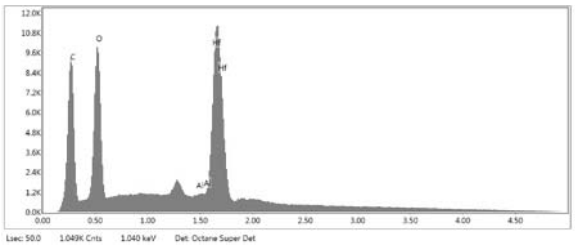

Figure 36. EDS area analysis on cross-section of a HfB_2 specimen subjected to 30 h of compression creep at 75 MPa at 1500°C in air, area 1: HfO_2 with C inclusion.

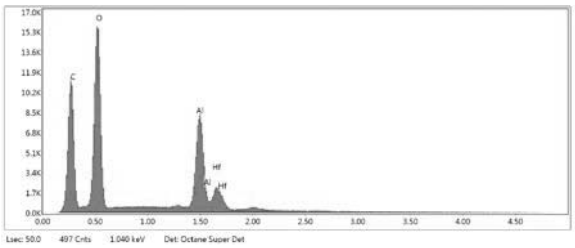

Figure 37. EDS area analysis on cross-section of a HfB_2 specimen subjected to 30 h of compression creep at 75 MPa at 1500°C in air, area 2: Likely Al_2O_3 with C inclusions and traces of HfO_2.

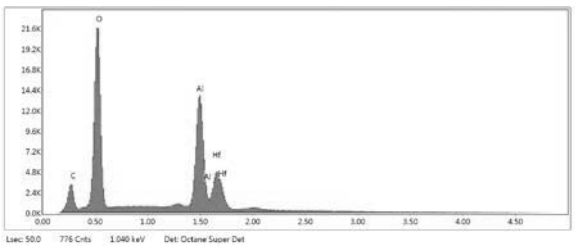

Figure 38. EDS area analysis on cross-section of a HfB_2 specimen subjected to 30 h of compression creep at 75 MPa at 1500°C in air, area 3: Likely Al_2O_3 with C inclusions and traces of HfO_2 (identical to area 4).

Winder found crustaceous deposits comprised of both yttrium and aluminum [23]. However, the lack of yttrium found during the EDS analysis of HfB_2-0SiC-3 suggests the presence of aluminum is due to the sapphire spacers, of composition Al_2O_3 and not the YAG. Given the aluminum containing deposits were only on the monolithic HfB_2 and

none of the SiC additive specimens, it is likely due to a thermo-chemical interaction between the sapphire spacers and HfB_2.

4.4 Analysis of Compression Creep at 1500 °C in Air

Results in Table 4 demonstrate that four creep tests of prolonged duration were completed in this work. In all tests, time, temperature and stress-strain data were recorded during heating to test temperature, 1-h soak at test temperature, loading to the creep stress level, and the actual creep period. Thus, creep strain vs. time behavior can be isolated and examined.

While creep analysis was not an objective of this research, creep data were analyzed and compared to historical data. This research may only be compared directly to Winder's research as all of DeGregoria's creep tests were conducted in an inert environment [17]. Winder found the minimum creep rate of a HfB_2-10% SiC sample compressed with 25 MPa for 1.6 h in air at 1500°C to be 1.68 $x10^{-6}$ 1/h [12]. It should be noted DeGregoria calculated minimum creep rates for HfB_2-10% SiC samples tested at stress levels between 25 and 75 MPa for durations of 0.5 to 12 h in argon at 1500°C to be the same order of magnitude as that observed by Winder [12,17].

Comparative creep tests from this research for HfB_2-10% SiC samples were an order of magnitude longer in duration than any previous HfB_2-10% SiC tests. This longer duration appears to have a significant impact on the minimum creep rate and could explain the three orders of magnitude difference between historical minimum creep rates found for HfB_2-10% SiC samples and those calculated in this research. Figure 39 highlights the difference in calculated minimum creep rates approaching the 3-hour mark

and 58-hour mark. Note that a creep rate similar to both DeGregoria and Winder is found in the early stages of the experiment whereas a test minimum creep rate is found much later in the experiment and yields a creep rate several orders of magnitude lower.

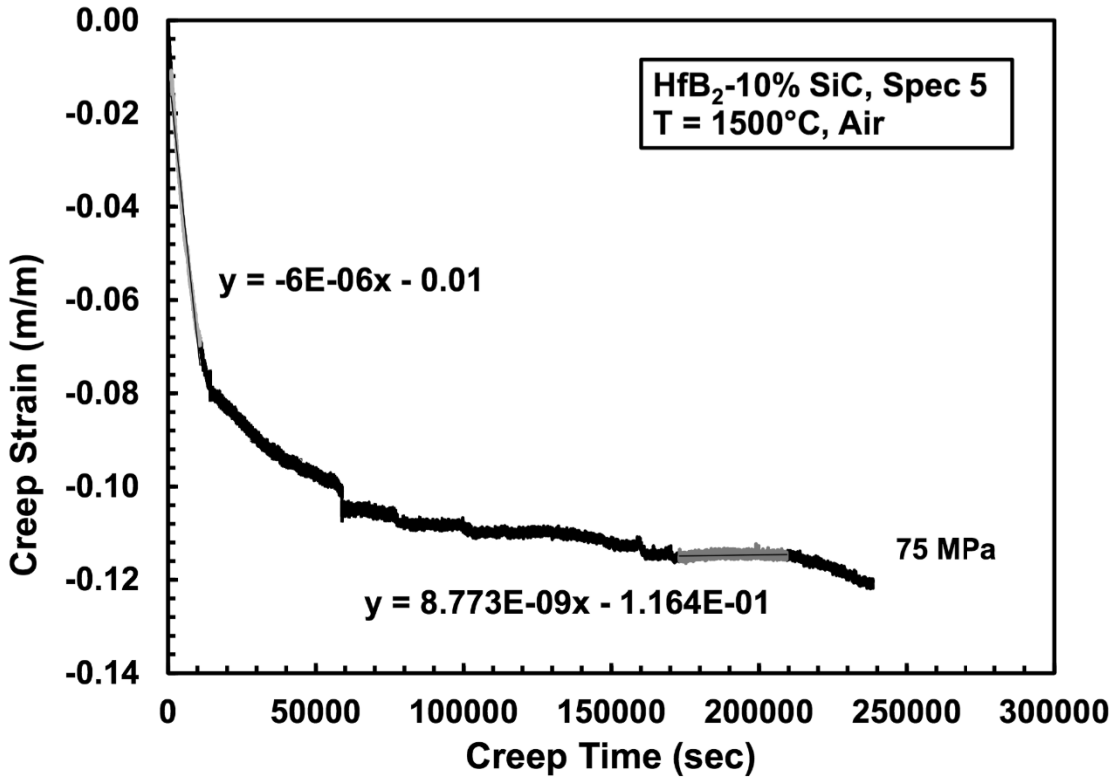

Figure 39. Creep Curve from HfB_2-10% SiC specimen subjected to 75 MPa compressive load for 66.3 h at 1500°C in air.

Therefore, while the minimum creep rates from the previous research were the initial creep rates for that particular experiment; it may be they were in fact not minimum rates for the material at the given stress as demonstrated by Figure 39.

V. Conclusion

This series of creep testing and oxidation analysis of HfB_2 and HfB_2–SiC was of significant importance primarily due to the ability to sustain higher loads for significantly longer durations. The replacement of alumina spacers with sapphire spacers is the leading reason for the improvement. The strength difference observed between random crystallographic orientation and c-plane orientations highlight the importance of sapphire spacer selection. In addition, the redesign of the custom YAG holders and new alignment tool allowed for even loading that also contributed to longer tests. *Further testing with random, a-plane and m-plane crystallographic orientations is required to maximize the load bearing abilities of the test facility.*

Additionally, the refinement of automatic shutdown procedures facilitated the sustainability of long duration single-man testing allowing the experiment to run unmonitored. These improvements allowed for testing ten times longer than previously achieved at similar stress levels. Creep data from the longer tests suggest that previous minimum creep rates were in-fact only initial creep rates. *Therefore in subsequent tests in which minimum creep rates are important, tests must run for a minimum of 18 hours, though ideally 48 hours or longer.*

Microstructural analysis of the tested specimens showed a reduction in the oxidation of SiC containing samples compared to monolithic by up to 95%. It also enabled the identification of large SiC depletion regions. Additionally stressed monolithic specimens exhibited 32% thinner oxide layers than the unstressed specimens suggesting that sustained compression restricts oxygen transfer. It was routinely observed that the corners regularly had thicker oxide layers, in some cases up to 230% larger than the

average. While the regions near corners were excluded in average thickness measurements, large fluctuations approaching the corners may have impacted the average thickness. *Therefore utilizing cylindrical specimens could foster uniform oxide growth and ensure accurate average measurements provided the scale thickness to specimen radius ratio was low.*

These results represent a significant advancement in the high temperature stressed oxidation testing of hafnium diboride. Additional the testing of hafnium diboride will allow for additional understanding of its behavior and feasibility as a structural-thermal protective material in hypersonic aerospace vehicles.

Appendix A: Images

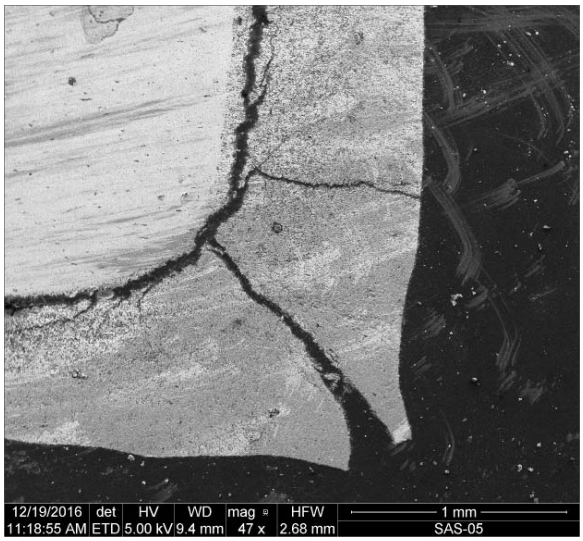

Figure A-1. Cross-sectional SEM micrograph of the HfB_2 specimen subjected to 20 h of compression creep at 75 MPa at 1500°C in air. Cracking at of the scale near corners was commonly observed.

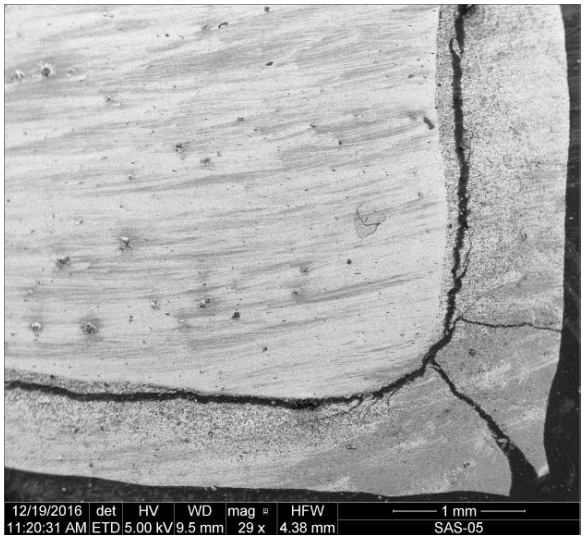

Figure A-2. Cross-sectional SEM micrograph of the HfB_2 specimen subjected to 20 h of compression creep at 75 MPa at 1500°C in air.

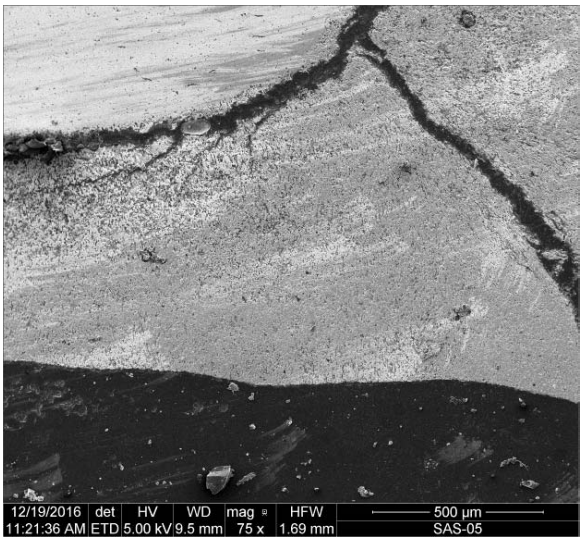

Figure A-3. Cross-sectional SEM micrograph of the HfB_2 specimen subjected to 20 h of compression creep at 75 MPa at 1500°C in air.

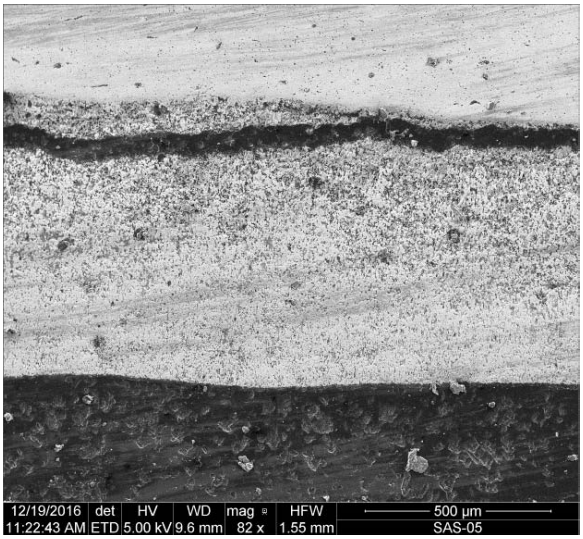

Figure A-4. Cross-sectional SEM micrograph of the HfB_2 specimen subjected to 20 h of compression creep at 75 MPa at 1500°C in air.

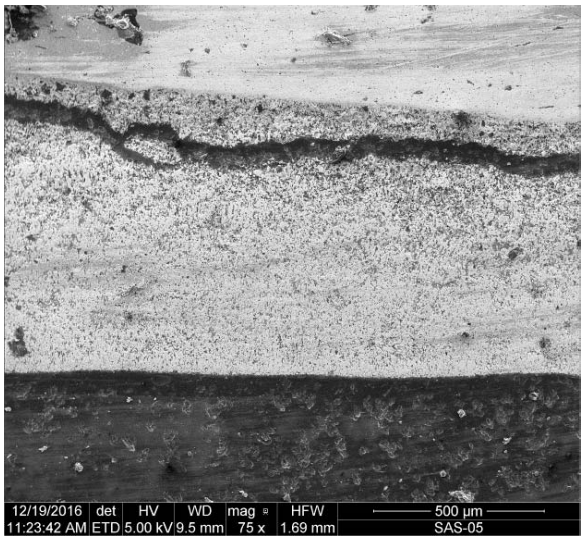

Figure A-5. Cross-sectional SEM micrograph of the HfB_2 specimen subjected to 20 h of compression creep at 75 MPa at 1500°C in air.

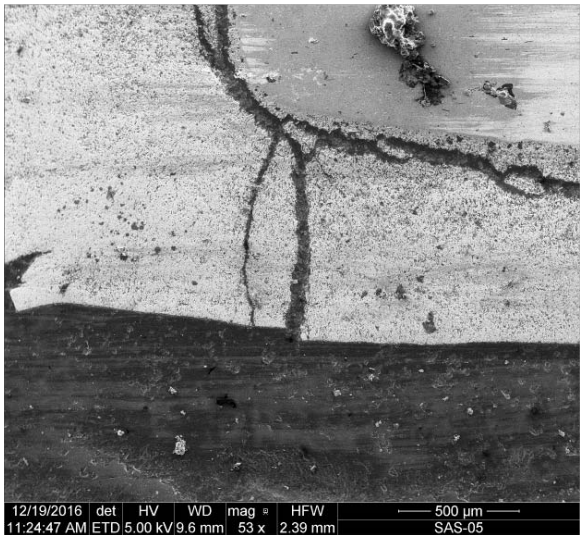

Figure A-6. Cross-sectional SEM micrograph of the HfB_2 specimen subjected to 20 h of compression creep at 75 MPa at 1500°C in air.

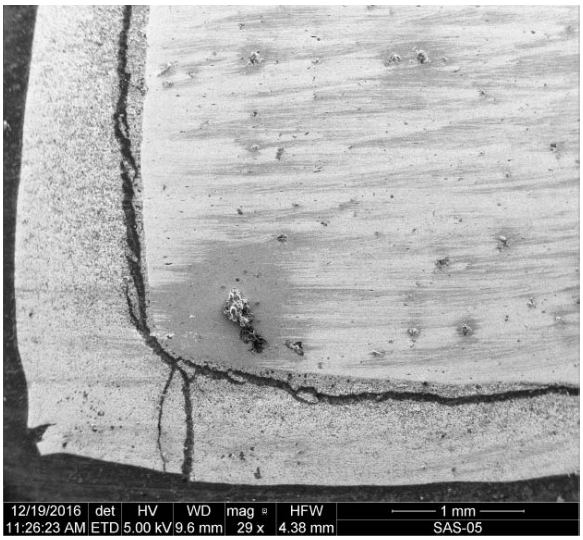

Figure A-7. Cross-sectional SEM micrograph of the HfB_2 specimen subjected to 20 h of compression creep at 75 MPa at 1500°C in air.

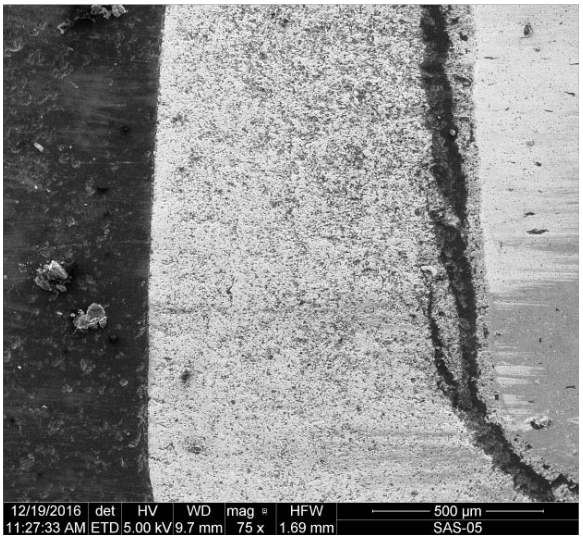

Figure A-8. Cross-sectional SEM micrograph of the HfB_2 specimen subjected to 20 h of compression creep at 75 MPa at 1500°C in air.

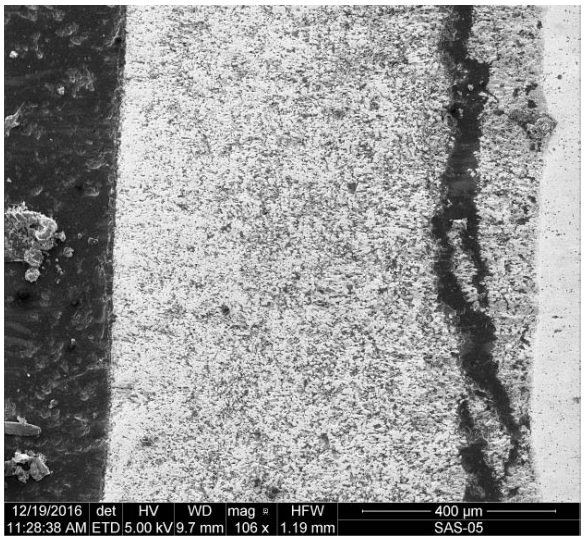

Figure A-9. Cross-sectional SEM micrograph of the HfB_2 specimen subjected to 20 h of compression creep at 75 MPa at 1500°C in air.

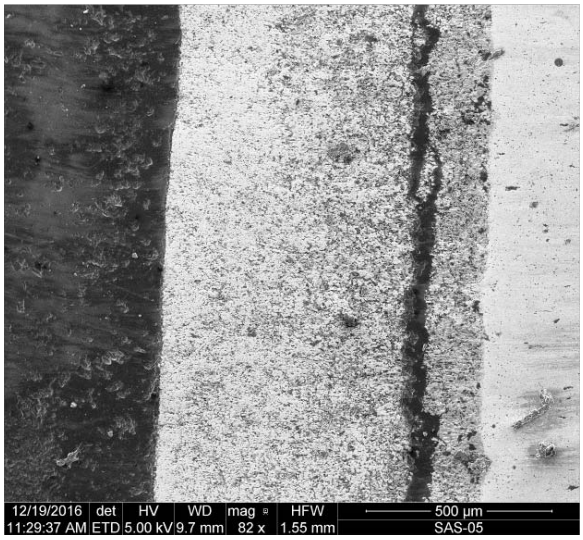

Figure A-10. Cross-sectional SEM micrograph of the HfB_2 specimen subjected to 20 h of compression creep at 75 MPa at 1500°C in air.

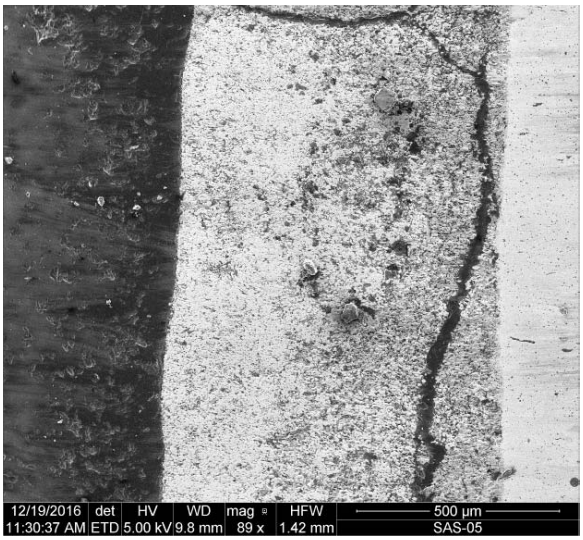

Figure A-11. Cross-sectional SEM micrograph of the HfB_2 specimen subjected to 20 h of compression creep at 75 MPa at 1500°C in air.

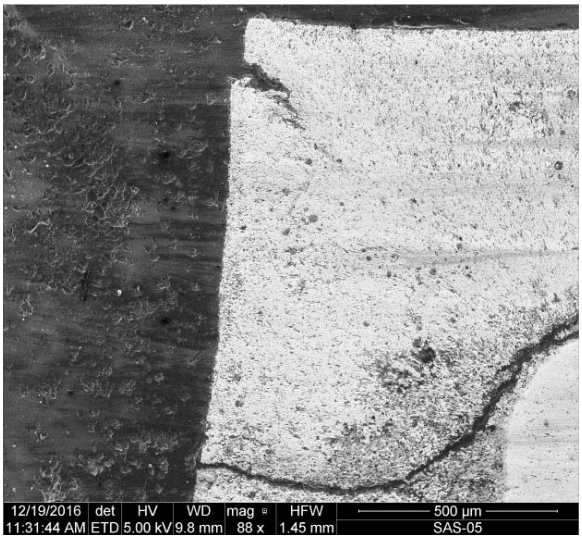

Figure A-12. Cross-sectional SEM micrograph of the HfB_2 specimen subjected to 20 h of compression creep at 75 MPa at 1500°C in air.

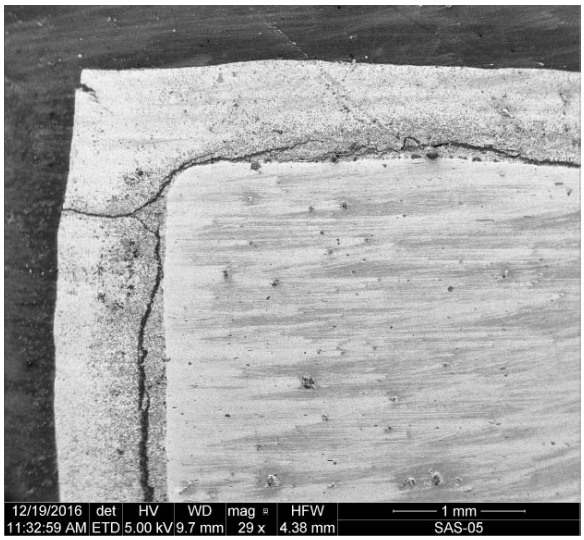

Figure A-13. Cross-sectional SEM micrograph of the HfB_2 specimen subjected to 20 h of compression creep at 75 MPa at 1500°C in air.

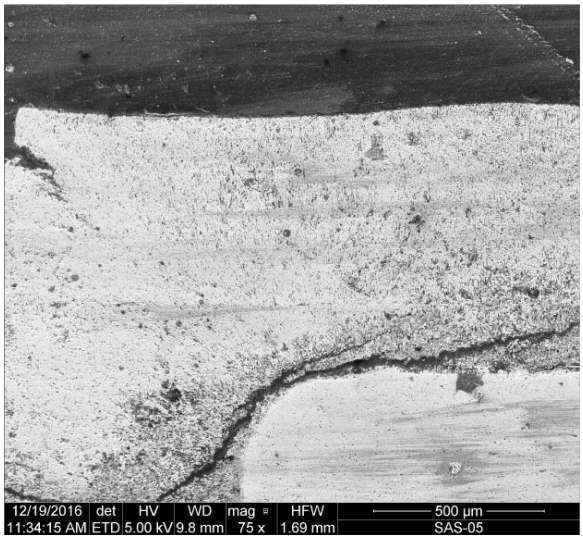

Figure A-14. Cross-sectional SEM micrograph of the HfB_2 specimen subjected to 20 h of compression creep at 75 MPa at 1500°C in air.

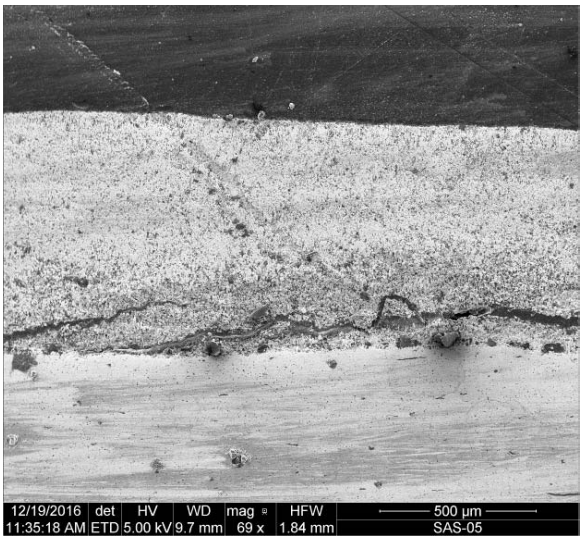

Figure A-15. Cross-sectional SEM micrograph of the HfB_2 specimen subjected to 20 h of compression creep at 75 MPa at 1500°C in air.

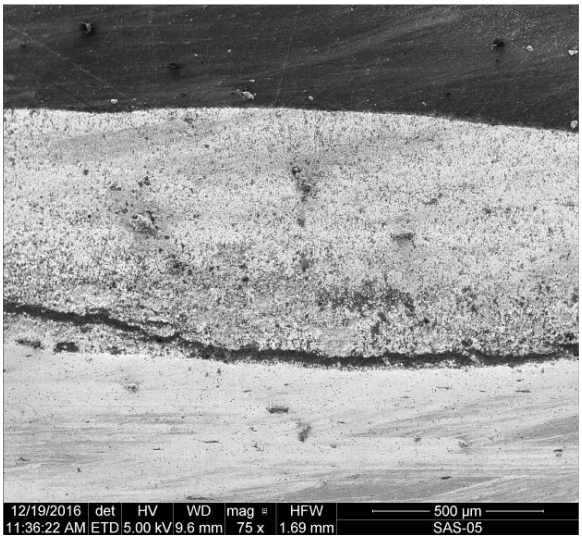

Figure A-16. Cross-sectional SEM micrograph of the HfB_2 specimen subjected to 20 h of compression creep at 75 MPa at 1500°C in air.

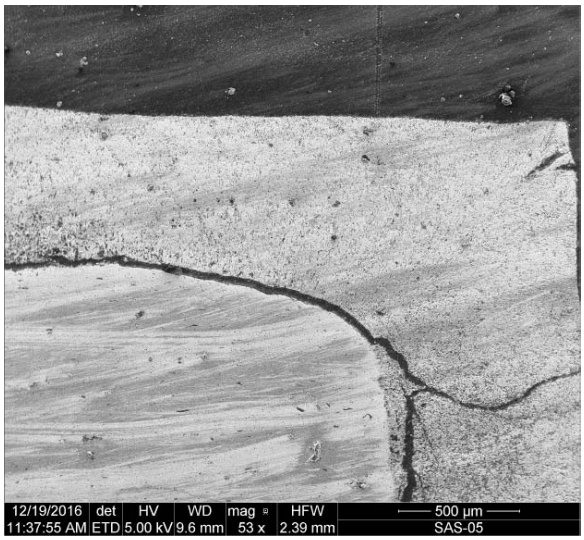

Figure A-17. Cross-sectional SEM micrograph of the HfB_2 specimen subjected to 20 h of compression creep at 75 MPa at 1500°C in air.

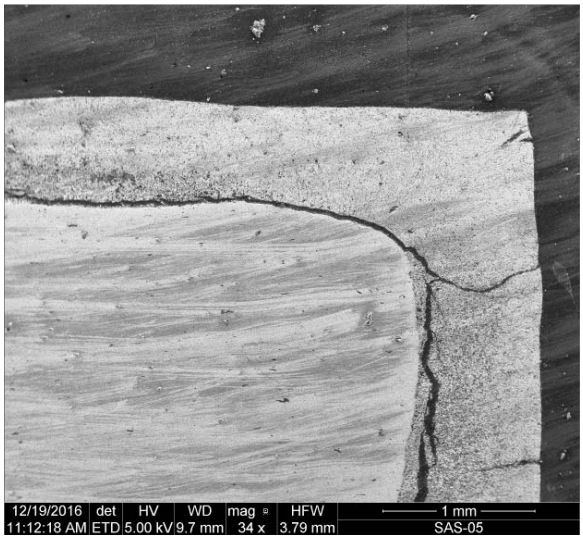

Figure A-18. Cross-sectional SEM micrograph of the HfB_2 specimen subjected to 20 h of compression creep at 75 MPa at 1500°C in air.

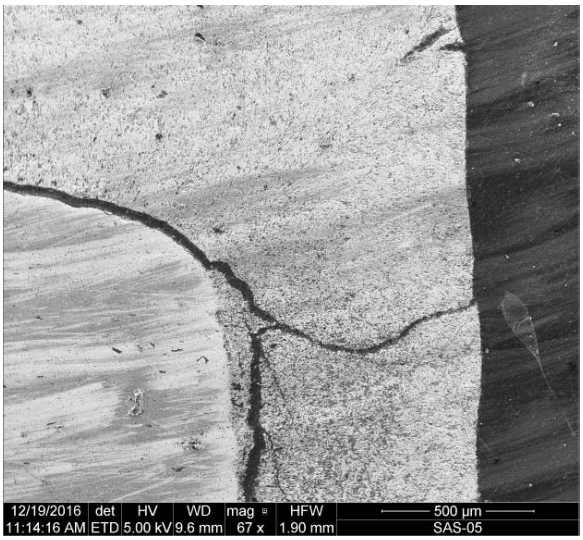

Figure A-19. Cross-sectional SEM micrograph of the HfB_2 specimen subjected to 20 h of compression creep at 75 MPa at 1500°C in air.

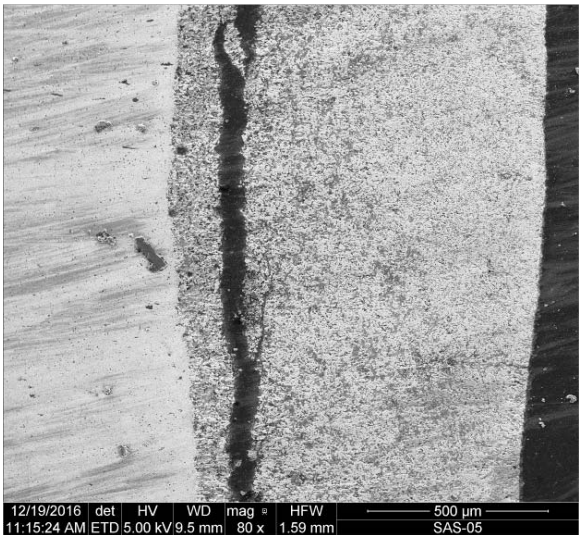

Figure A-20. Cross-sectional SEM micrograph of the HfB_2 specimen subjected to 20 h of compression creep at 75 MPa at 1500°C in air.

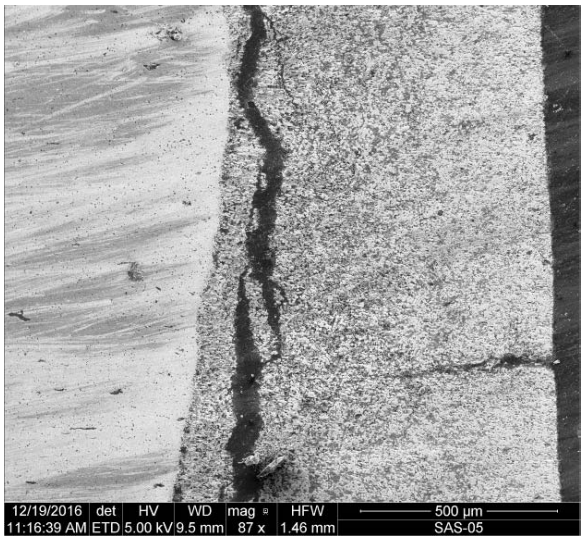

Figure A-21. Cross-sectional SEM micrograph of the HfB_2 specimen subjected to 20 h of compression creep at 75 MPa at 1500°C in air.

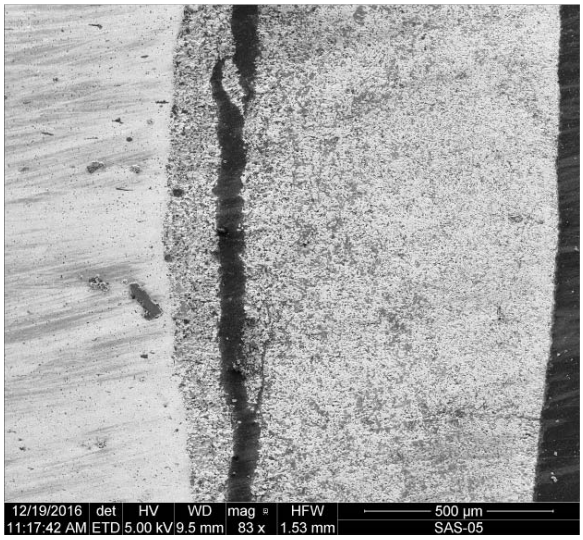

Figure A-22. Cross-sectional SEM micrograph of the HfB_2 specimen subjected to 20 h of compression creep at 75 MPa at 1500°C in air.

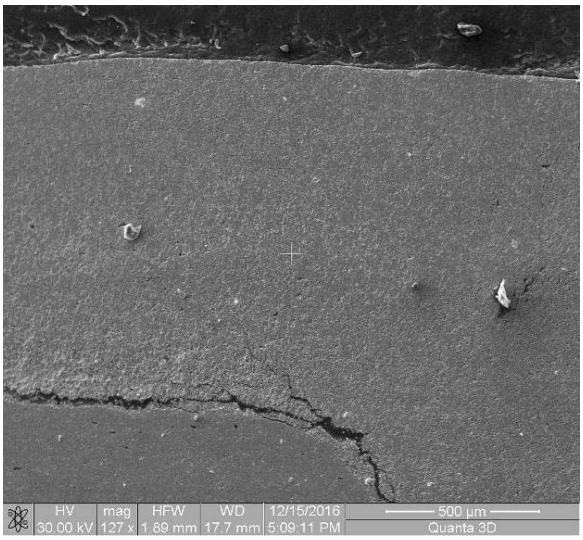

Figure A-23. Cross-sectional SEM micrograph of the HfB_2 specimen subjected to 30 h of compression creep at 75 MPa at 1500°C in air.

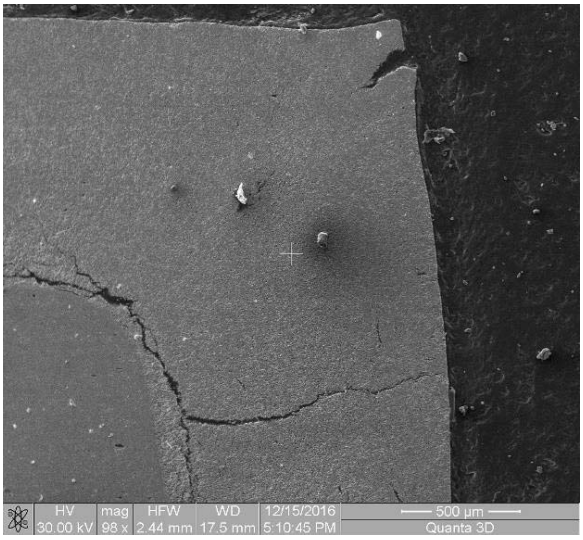

Figure A-24. Cross-sectional SEM micrograph of the HfB_2 specimen subjected to 30 h of compression creep at 75 MPa at 1500°C in air.

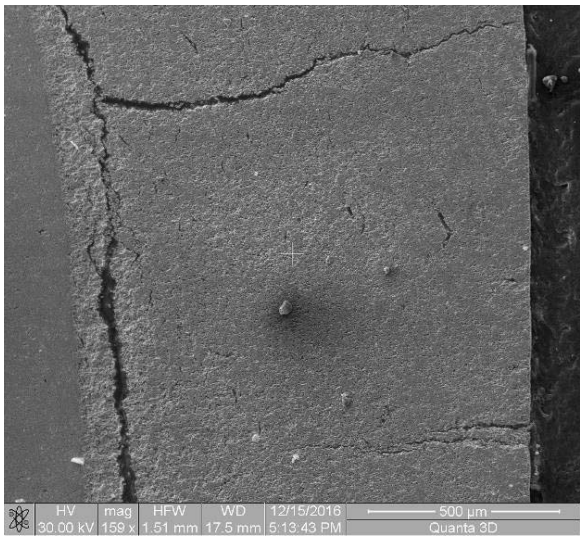

Figure A-25. Cross-sectional SEM micrograph of the HfB_2 specimen subjected to 30 h of compression creep at 75 MPa at 1500°C in air.

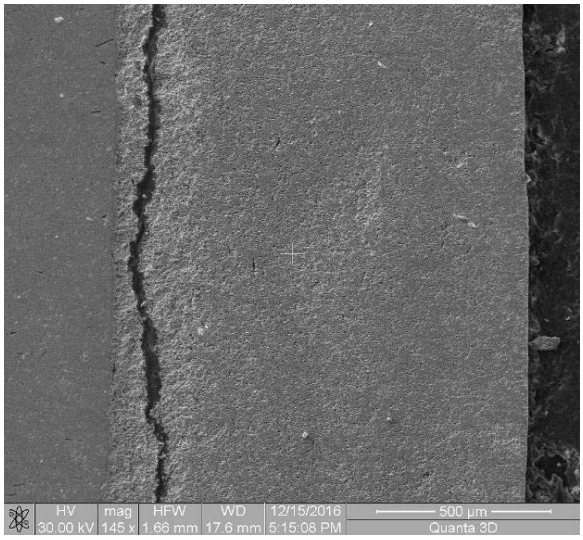

Figure A-26. Cross-sectional SEM micrograph of the HfB_2 specimen subjected to 30 h of compression creep at 75 MPa at 1500°C in air.

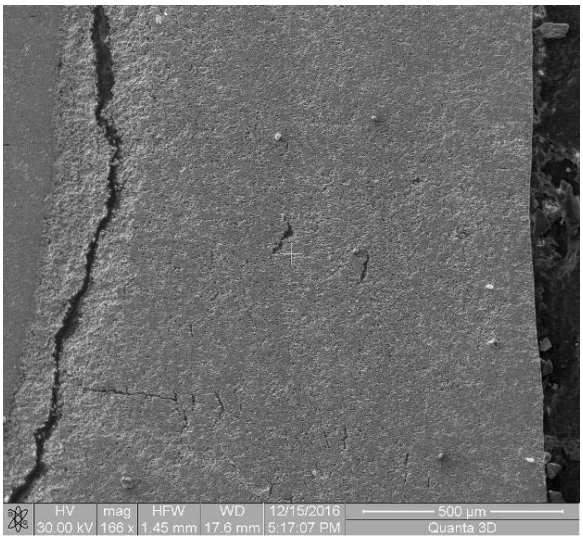

Figure A-27. Cross-sectional SEM micrograph of the HfB_2 specimen subjected to 30 h of compression creep at 75 MPa at 1500°C in air.

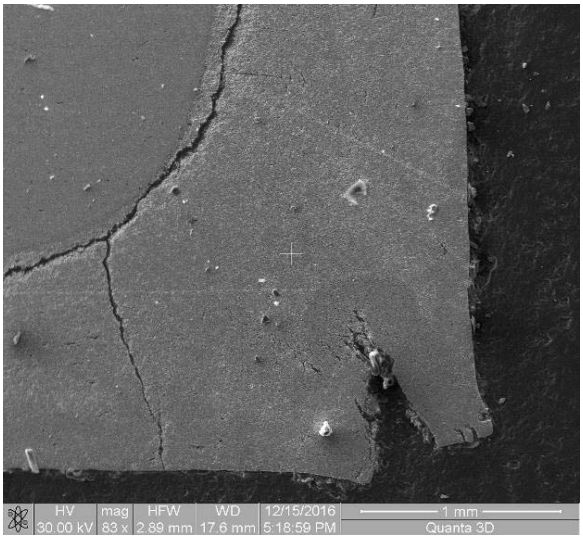

Figure A-28. Cross-sectional SEM micrograph of the HfB_2 specimen subjected to 30 h of compression creep at 75 MPa at 1500°C in air.

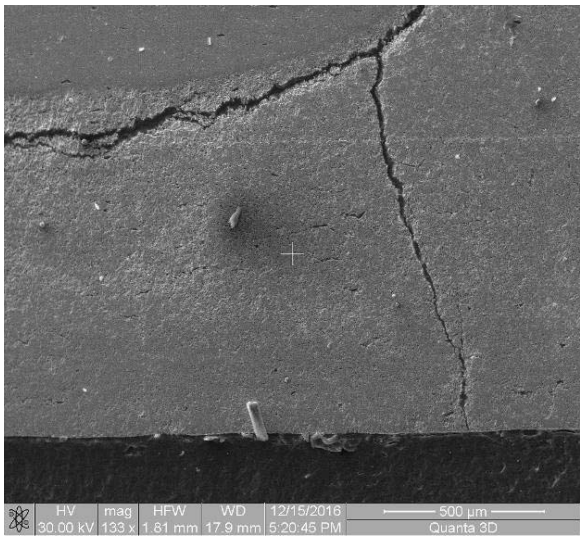

Figure A-29. Cross-sectional SEM micrograph of the HfB_2 specimen subjected to 30 h of compression creep at 75 MPa at 1500°C in air.

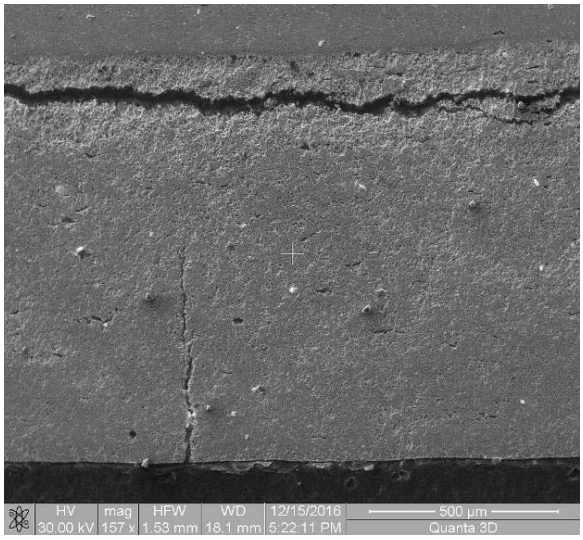

Figure A-30. Cross-sectional SEM micrograph of the HfB_2 specimen subjected to 30 h of compression creep at 75 MPa at 1500°C in air.

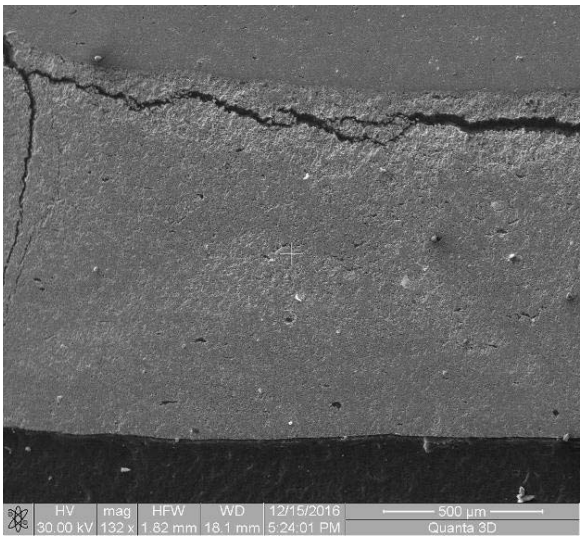

Figure A-31. Cross-sectional SEM micrograph of the HfB_2 specimen subjected to 30 h of compression creep at 75 MPa at 1500°C in air.

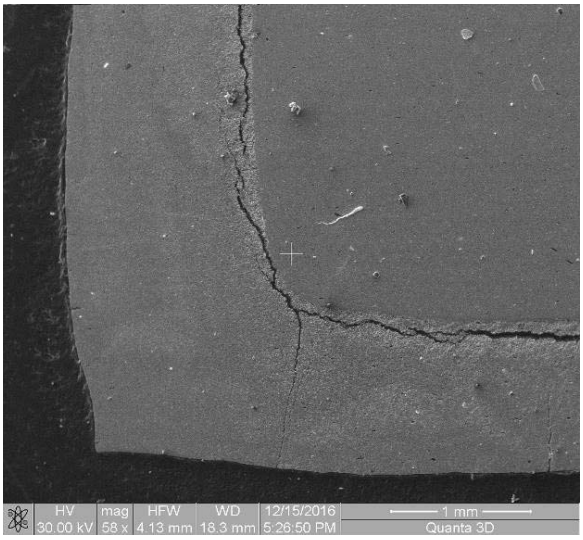

Figure A-32. Cross-sectional SEM micrograph of the HfB_2 specimen subjected to 30 h of compression creep at 75 MPa at 1500°C in air.

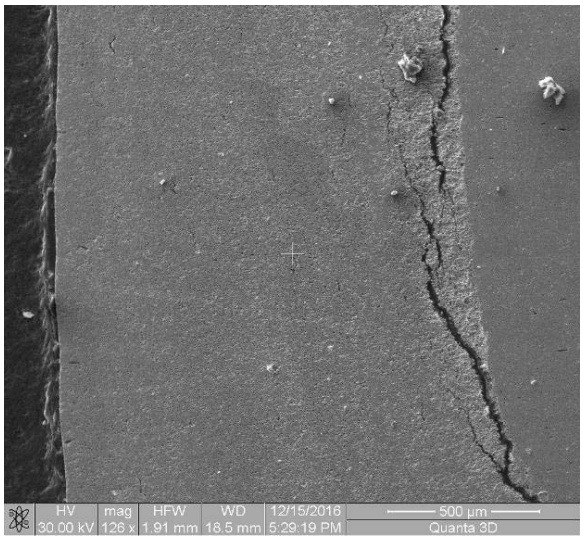

Figure A-33. Cross-sectional SEM micrograph of the HfB_2 specimen subjected to 30 h of compression creep at 75 MPa at 1500°C in air.

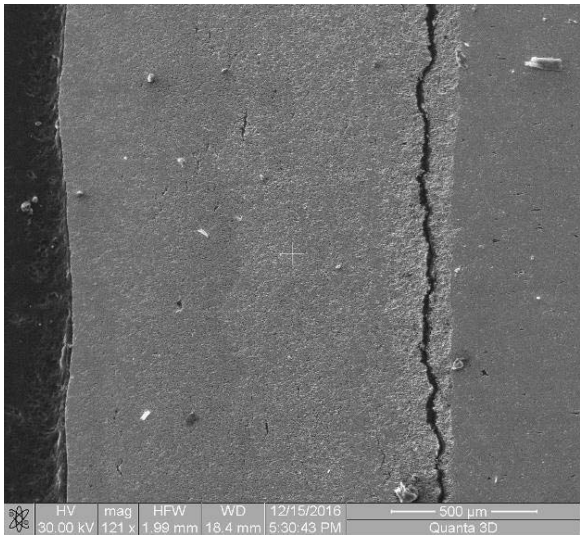

Figure A-34. Cross-sectional SEM micrograph of the HfB_2 specimen subjected to 30 h of compression creep at 75 MPa at 1500°C in air.

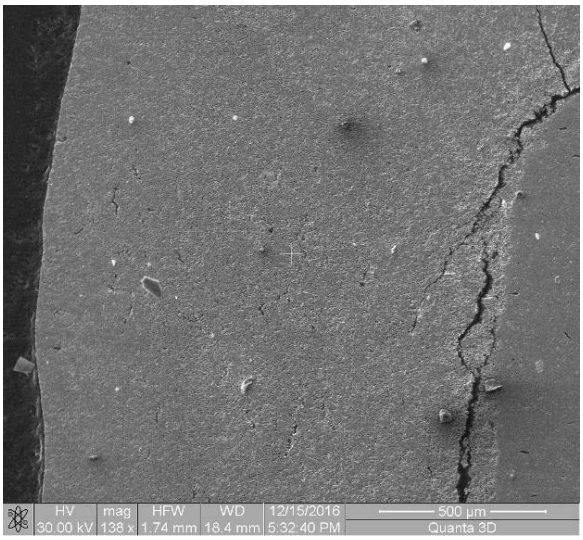

Figure A-35. Cross-sectional SEM micrograph of the HfB_2 specimen subjected to 30 h of compression creep at 75 MPa at 1500°C in air.

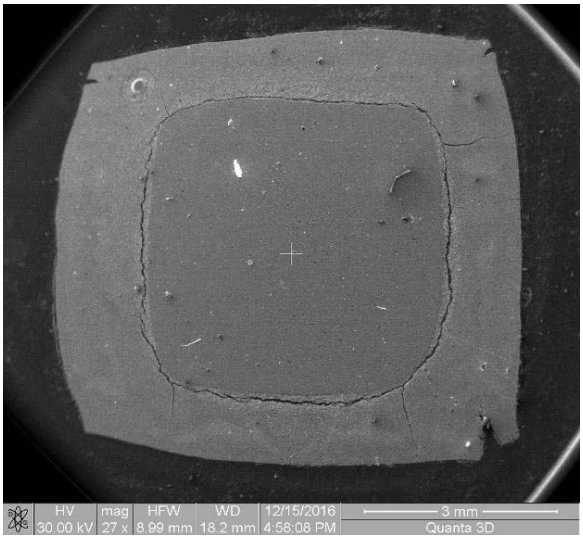

Figure A-36. Cross-sectional SEM micrograph of the HfB_2 specimen subjected to 30 h of compression creep at 75 MPa at 1500°C in air.

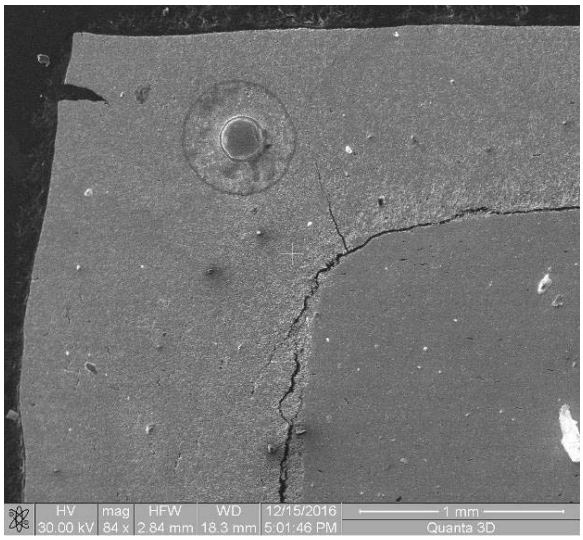

Figure A-37. Cross-sectional SEM micrograph of the HfB_2 specimen subjected to 30 h of compression creep at 75 MPa at 1500°C in air.

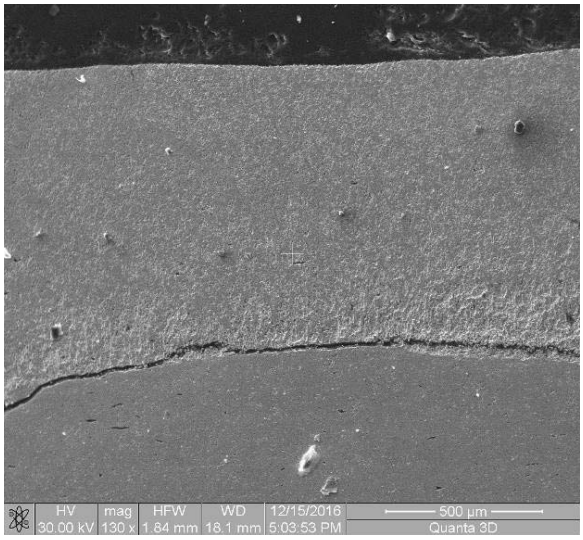

Figure A-38. Cross-sectional SEM micrograph of the HfB_2 specimen subjected to 30 h of compression creep at 75 MPa at 1500°C in air.

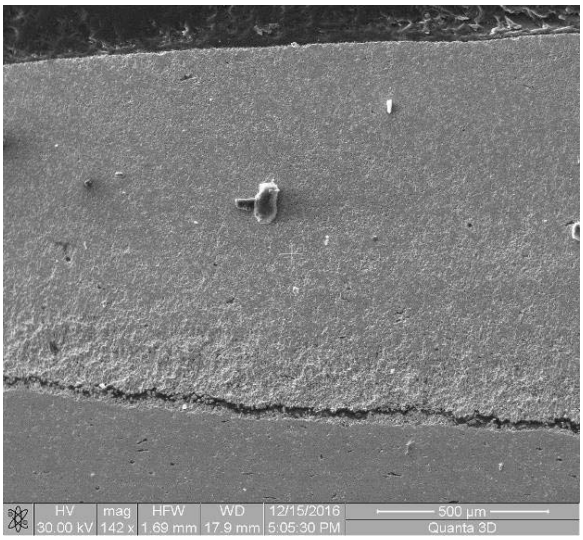

Figure A-39. Cross-sectional SEM micrograph of the HfB_2 specimen subjected to 30 h of compression creep at 75 MPa at 1500°C in air.

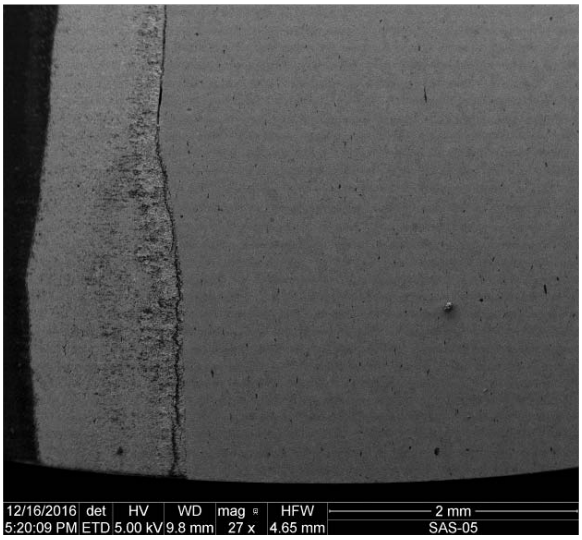

Figure A-40. Longitudinal-section SEM micrograph of the HfB_2 specimen subjected to 30 h of compression creep at 75 MPa at 1500°C in air.

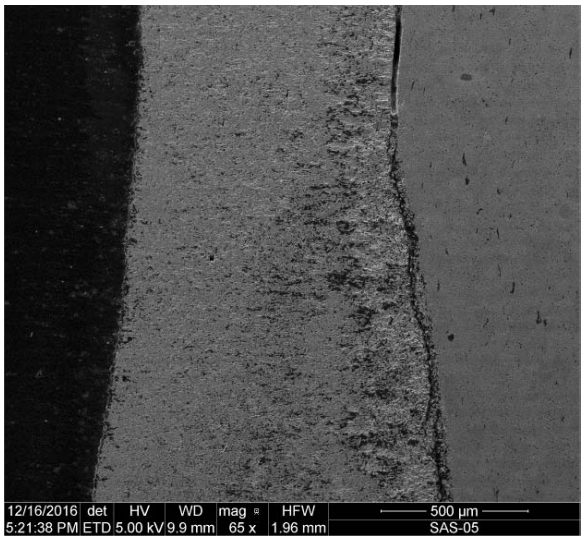

Figure A-41. Longitudinal-section SEM micrograph of the HfB_2 specimen subjected to 30 h of compression creep at 75 MPa at 1500°C in air.

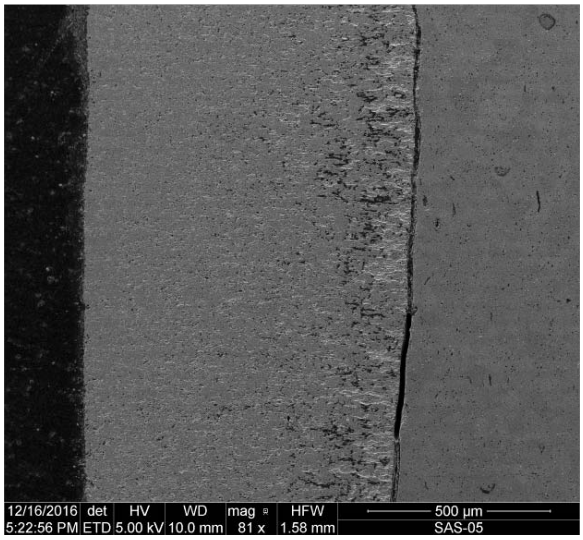

Figure A-42. Longitudinal-section SEM micrograph of the HfB_2 specimen subjected to 30 h of compression creep at 75 MPa at 1500°C in air.

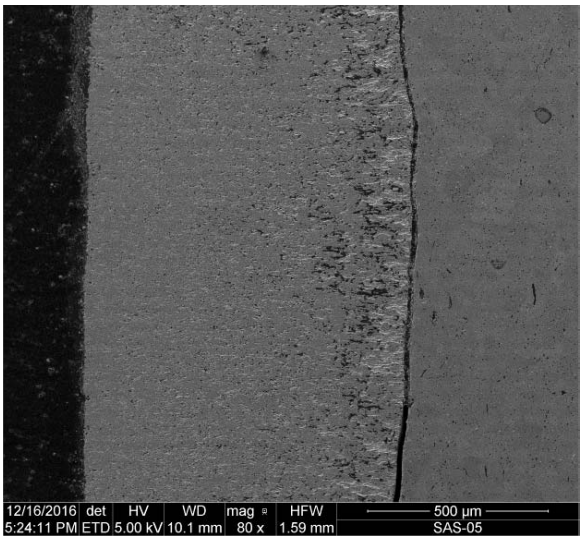

Figure A-43. Longitudinal-section SEM micrograph of the HfB_2 specimen subjected to 30 h of compression creep at 75 MPa at 1500°C in air.

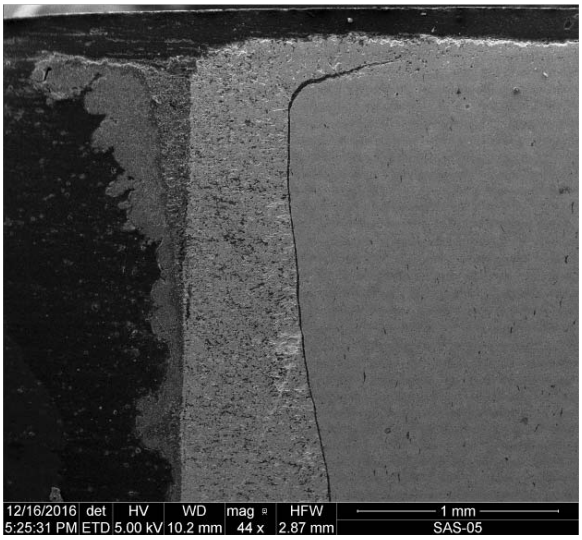

Figure A-44. Longitudinal-section SEM micrograph of the HfB_2 specimen subjected to 30 h of compression creep at 75 MPa at 1500°C in air.

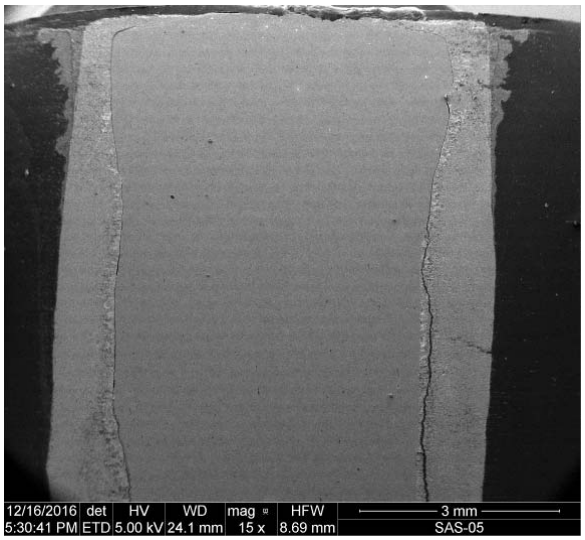

Figure A-45. Longitudinal-section SEM micrograph of the HfB_2 specimen subjected to 30 h of compression creep at 75 MPa at 1500°C in air.

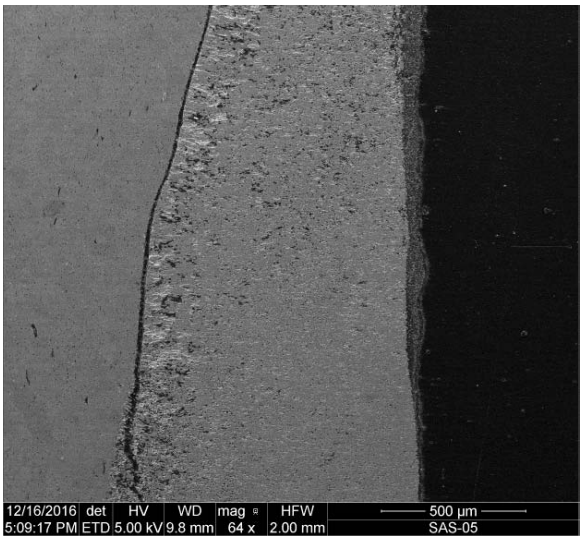

Figure A-47. Longitudinal-section SEM micrograph of the HfB_2 specimen subjected to 30 h of compression creep at 75 MPa at 1500°C in air.

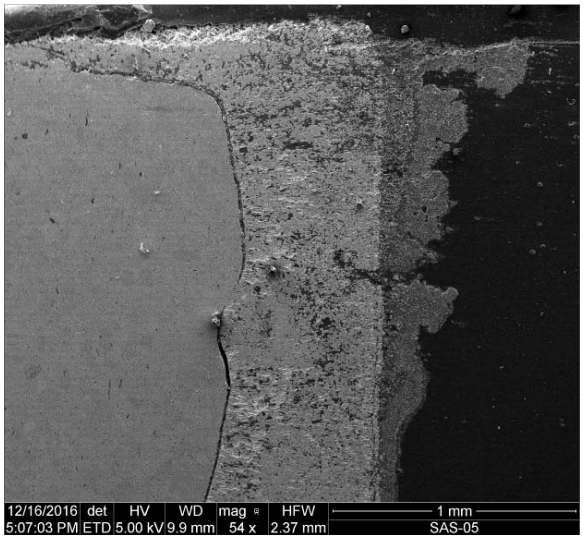

Figure A-46. Longitudinal-section SEM micrograph of the HfB_2 specimen subjected to 30 h of compression creep at 75 MPa at 1500°C in air.

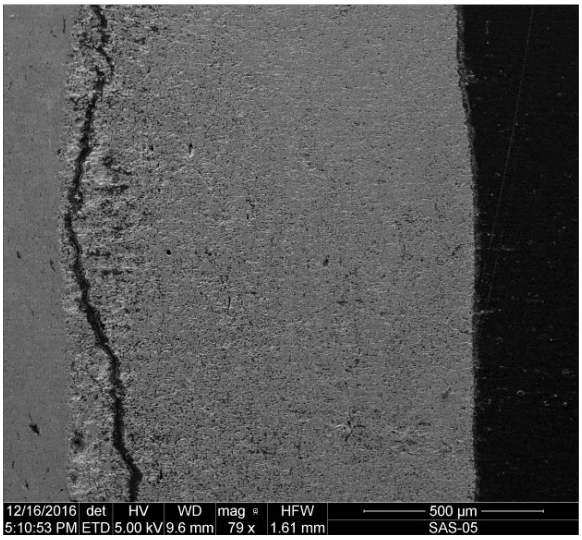

Figure A-48. Longitudinal-section SEM micrograph of the HfB_2 specimen subjected to 30 h of compression creep at 75 MPa at 1500°C in air.

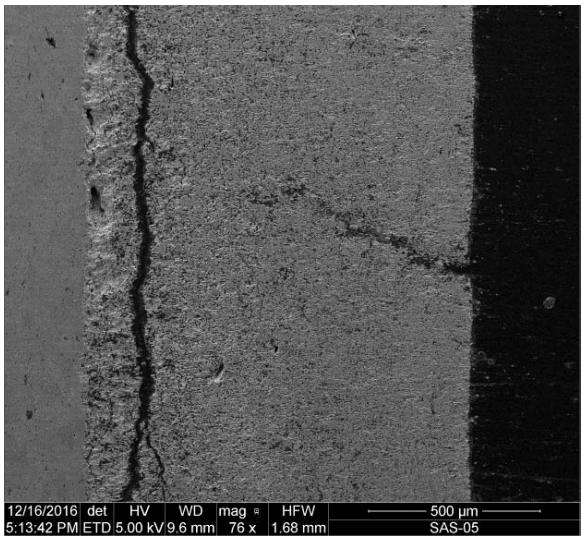

Figure A-49. Longitudinal-section SEM micrograph of the HfB_2 specimen subjected to 30 h of compression creep at 75 MPa at 1500°C in air.

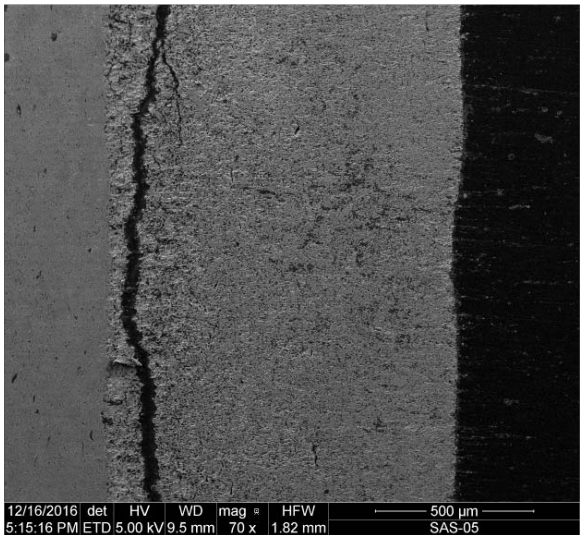

Figure A-50. Longitudinal-section SEM micrograph of the HfB_2 specimen subjected to 30 h of compression creep at 75 MPa at 1500°C in air.

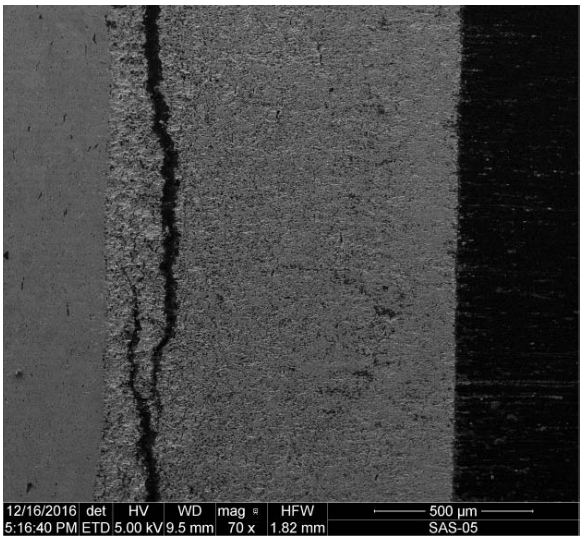

Figure A-51. Longitudinal-section SEM micrograph of the HfB_2 specimen subjected to 30 h of compression creep at 75 MPa at 1500°C in air.

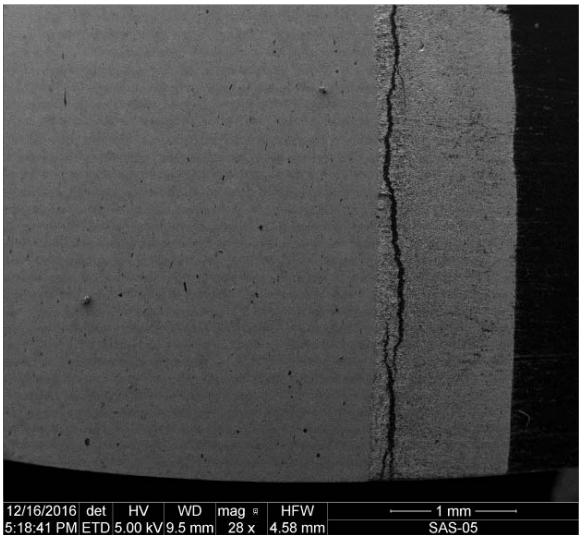

Figure A-52. Longitudinal-section SEM micrograph of the HfB_2 specimen subjected to 30 h of compression creep at 75 MPa at 1500°C in air.

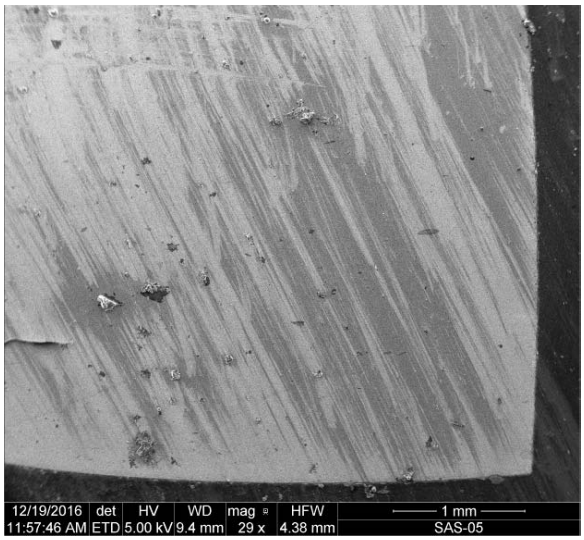

Figure A-53. Cross-sectional SEM micrograph of the HfB_2-10% SiC specimen subjected to 1 h of compression creep at 8 MPa at 1500°C in air (failed upon load-up to 100MPa).

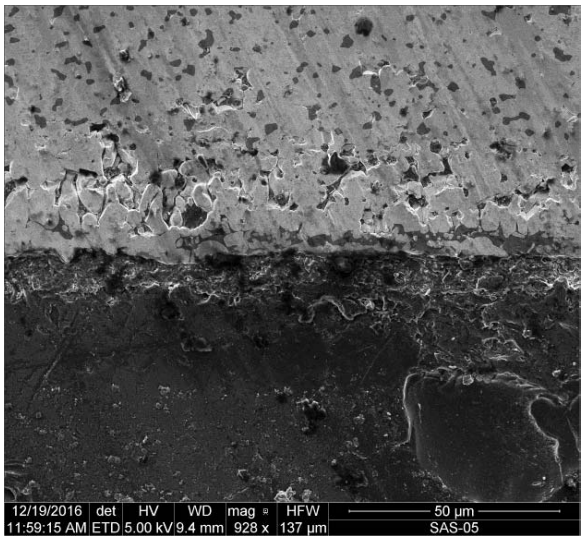

Figure A-54. Cross-sectional SEM micrograph of the HfB_2-10% SiC specimen subjected to 1 h of compression creep at 8 MPa at 1500°C in air (failed upon load-up to 100MPa).

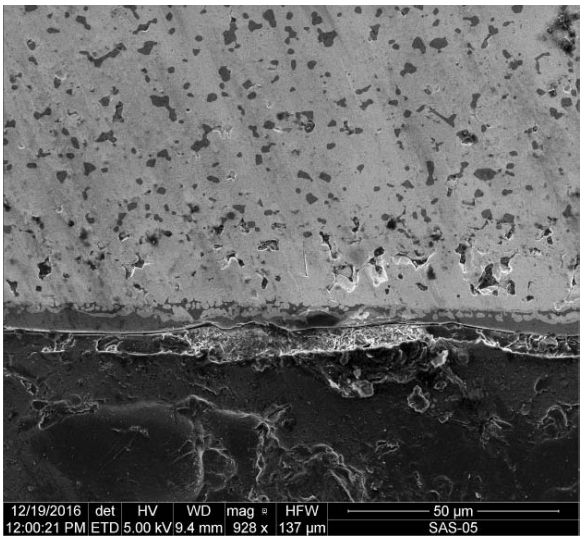

Figure A-55. Cross-sectional SEM micrograph of the HfB_2-10% SiC specimen subjected to 1 h of compression creep at 8 MPa at 1500°C in air (failed upon load-up to 100MPa).

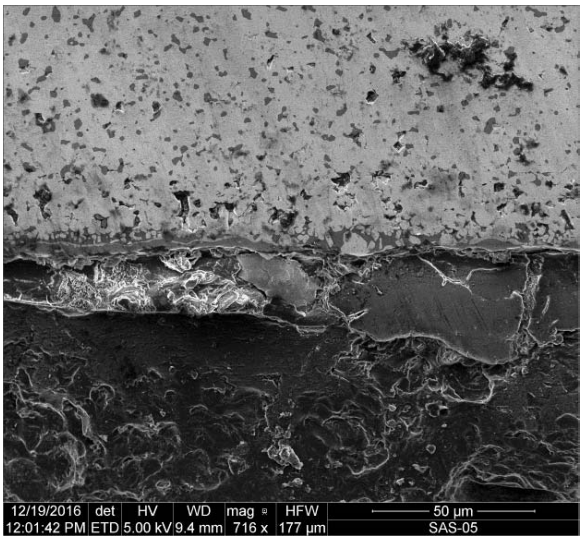

Figure A-56. Cross-sectional SEM micrograph of the HfB_2-10% SiC specimen subjected to 1 h of compression creep at 8 MPa at 1500°C in air (failed upon load-up to 100MPa).

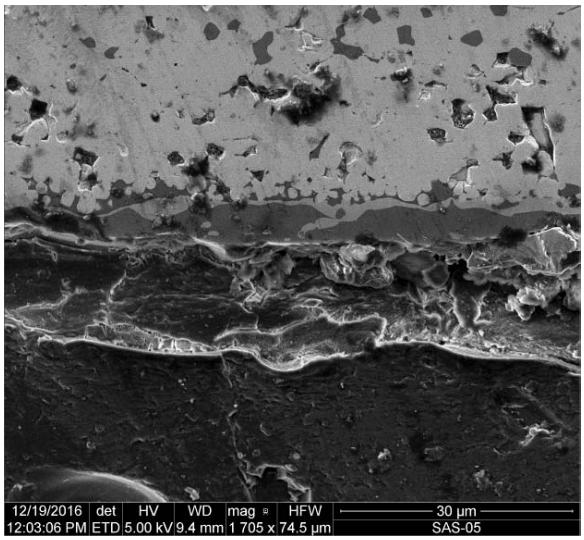

Figure A-57. Cross-sectional SEM micrograph of the HfB_2-10% SiC specimen subjected to 1 h of compression creep at 8 MPa at 1500°C in air (failed upon load-up to 100MPa).

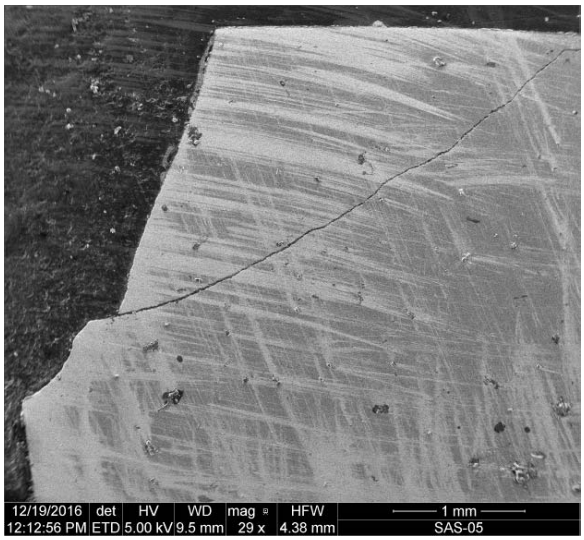

Figure A-58. Cross-sectional SEM micrograph of the HfB_2-10% SiC specimen subjected to 1 h of compression creep at 8 MPa at 1500°C in air (failed upon load-up to 100MPa).

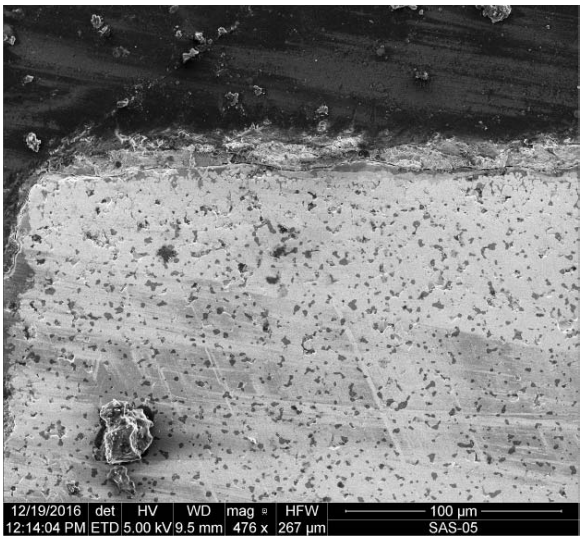

Figure A-59. Cross-sectional SEM micrograph of the HfB_2-10% SiC specimen subjected to 1 h of compression creep at 8 MPa at 1500°C in air (failed upon load-up to 100MPa).

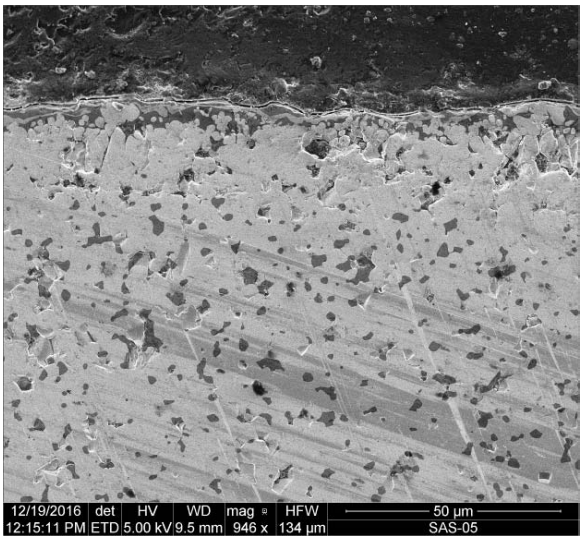

Figure A-60. Cross-sectional SEM micrograph of the HfB_2-10% SiC specimen subjected to 1 h of compression creep at 8 MPa at 1500°C in air (failed upon load-up to 100MPa).

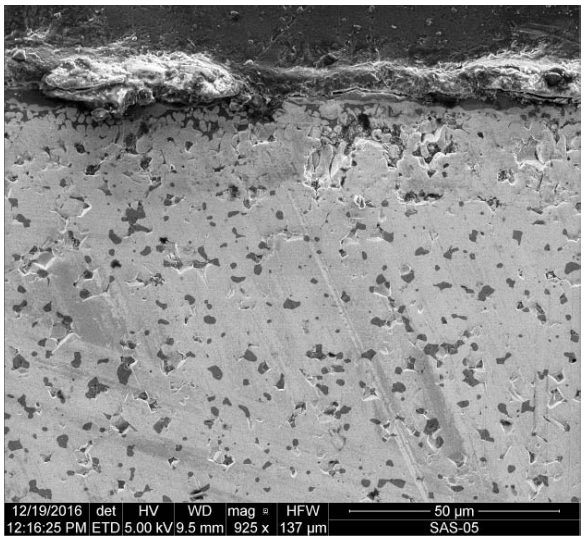

Figure A-61. Cross-sectional SEM micrograph of the HfB_2-10% SiC specimen subjected to 1 h of compression creep at 8 MPa at 1500°C in air (failed upon load-up to 100MPa).

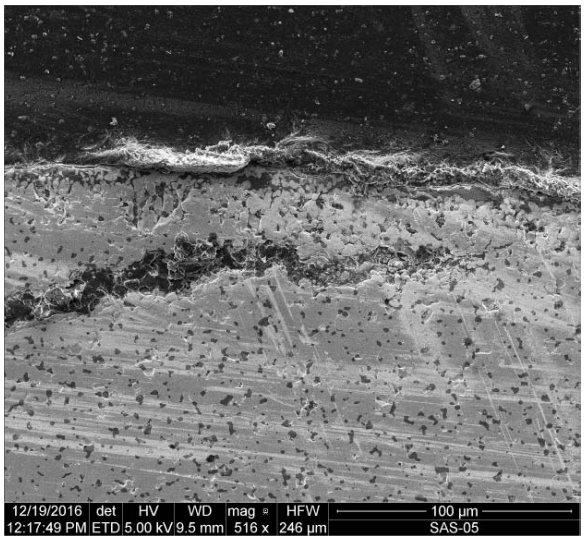

Figure A-62. Cross-sectional SEM micrograph of the HfB_2-10% SiC specimen subjected to 1 h of compression creep at 8 MPa at 1500°C in air (failed upon load-up to 100MPa).

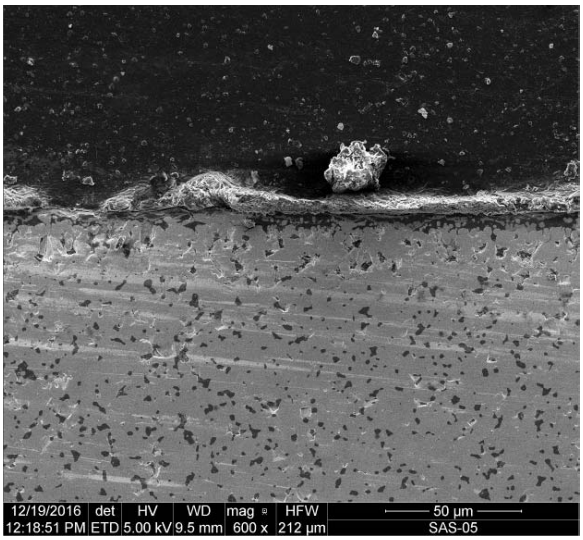

Figure A-63. Cross-sectional SEM micrograph of the HfB_2-10% SiC specimen subjected to 1 h of compression creep at 8 MPa at 1500°C in air (failed upon load-up to 100MPa).

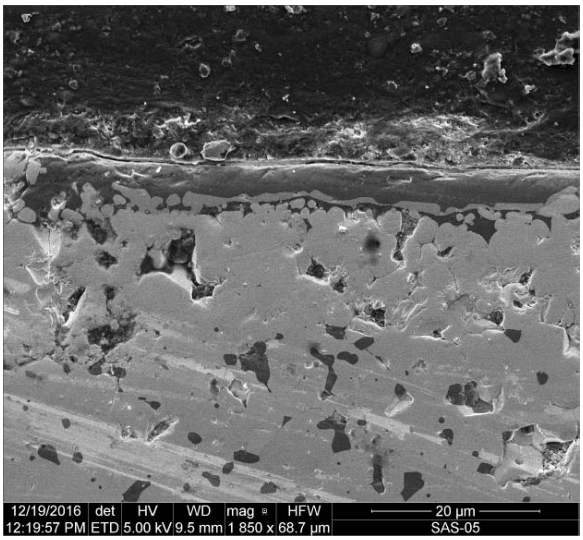

Figure A-64. Cross-sectional SEM micrograph of the HfB_2-10% SiC specimen subjected to 1 h of compression creep at 8 MPa at 1500°C in air (failed upon load-up to 100MPa).

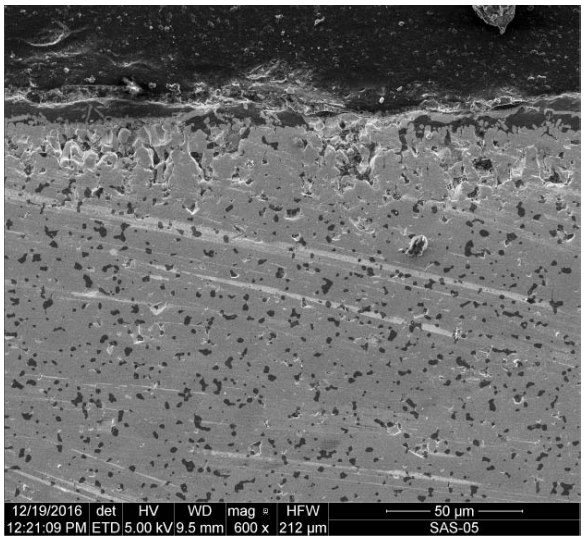

Figure A-65. Cross-sectional SEM micrograph of the HfB_2-10% SiC specimen subjected to 1 h of compression creep at 8 MPa at 1500°C in air (failed upon load-up to 100MPa).

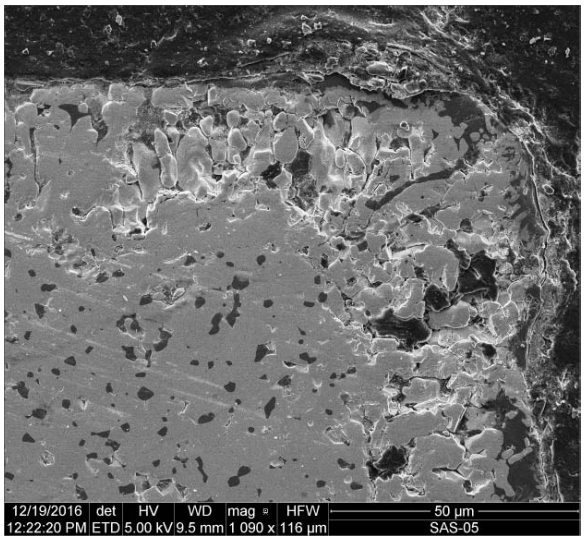

Figure A-66. Cross-sectional SEM micrograph of the HfB_2-10% SiC specimen subjected to 1 h of compression creep at 8 MPa at 1500°C in air (failed upon load-up to 100MPa).

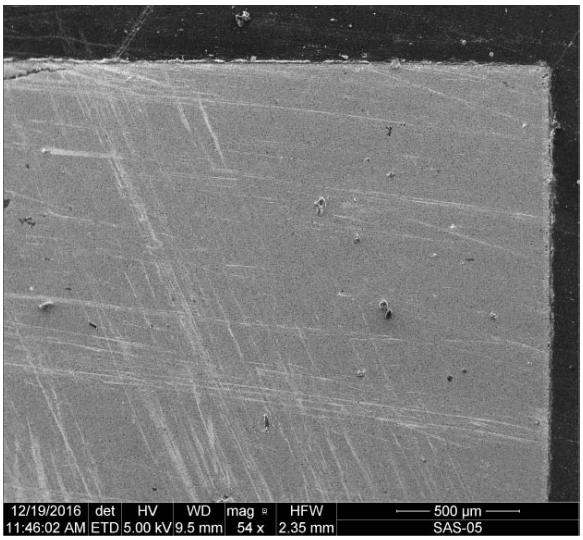

Figure A-67. Cross-sectional SEM micrograph of the HfB_2-10% SiC specimen subjected to 1 h of compression creep at 8 MPa at 1500°C in air (failed upon load-up to 100MPa).

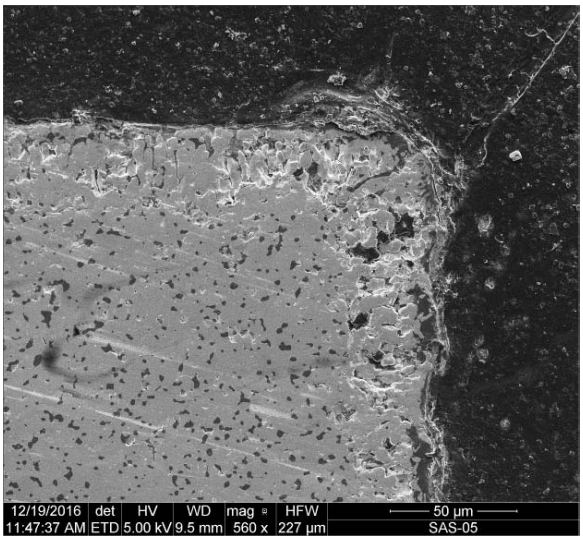

Figure A-68. Cross-sectional SEM micrograph of the HfB_2-10% SiC specimen subjected to 1 h of compression creep at 8 MPa at 1500°C in air (failed upon load-up to 100MPa).

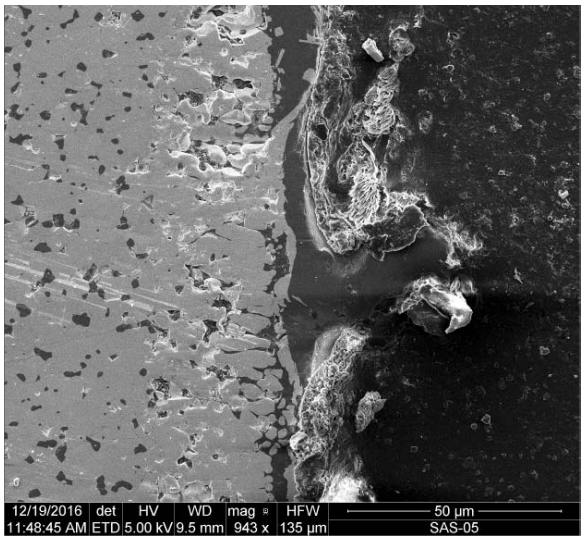

Figure A-69. Cross-sectional SEM micrograph of the HfB_2-10% SiC specimen subjected to 1 h of compression creep at 8 MPa at 1500°C in air (failed upon load-up to 100MPa).

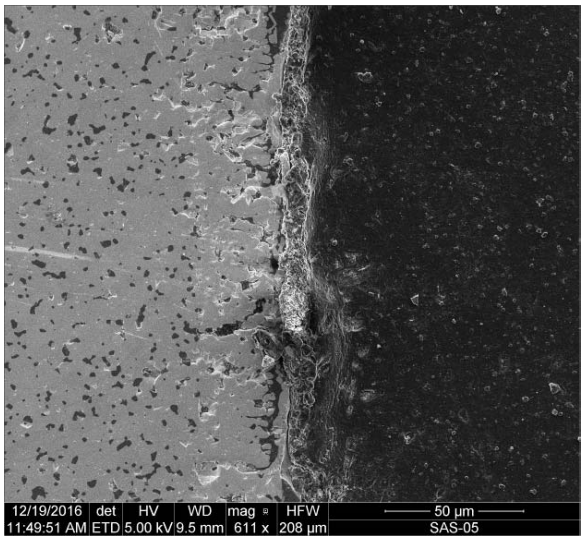

Figure A-70. Cross-sectional SEM micrograph of the HfB_2-10% SiC specimen subjected to 1 h of compression creep at 8 MPa at 1500°C in air (failed upon load-up to 100MPa).

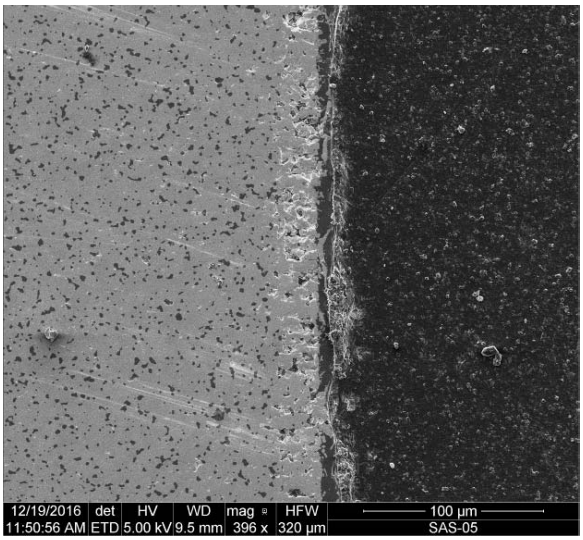

Figure A-71. Cross-sectional SEM micrograph of the HfB_2-10% SiC specimen subjected to 1 h of compression creep at 8 MPa at 1500°C in air (failed upon load-up to 100MPa).

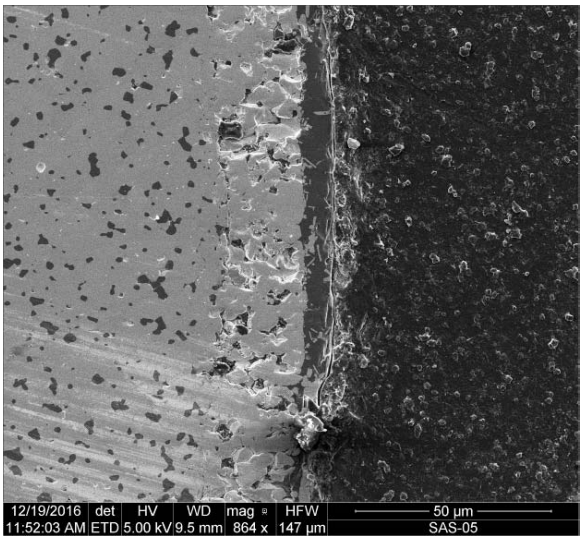

Figure A-72. Cross-sectional SEM micrograph of the HfB_2-10% SiC specimen subjected to 1 h of compression creep at 8 MPa at 1500°C in air (failed upon load-up to 100MPa).

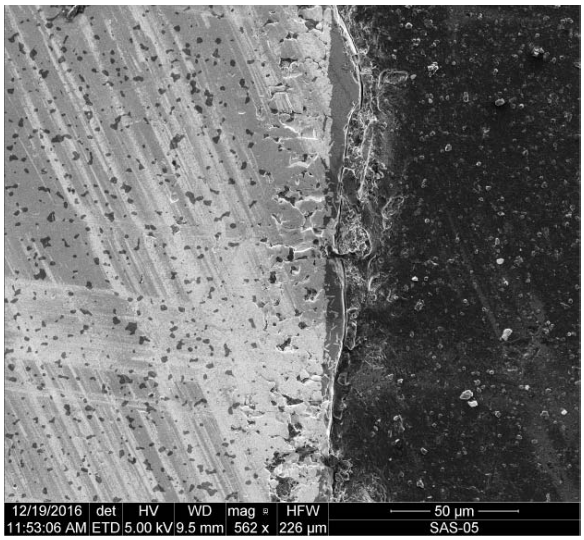

Figure A-73. Cross-sectional SEM micrograph of the HfB_2-10% SiC specimen subjected to 1 h of compression creep at 8 MPa at 1500°C in air (failed upon load-up to 100MPa).

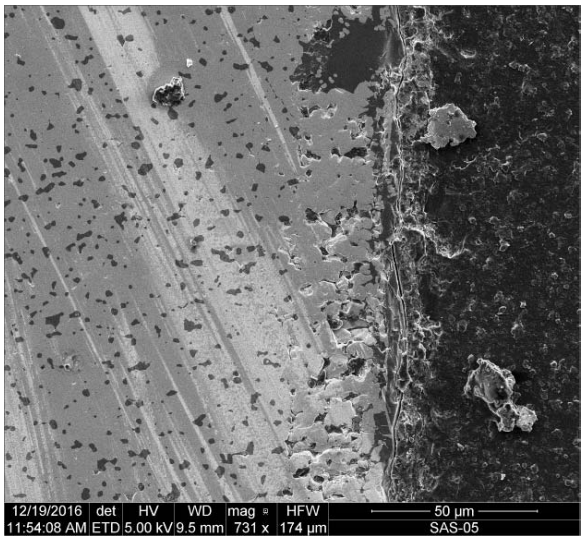

Figure A-74. Cross-sectional SEM micrograph of the HfB_2-10% SiC specimen subjected to 1 h of compression creep at 8 MPa at 1500°C in air (failed upon load-up to 100MPa).

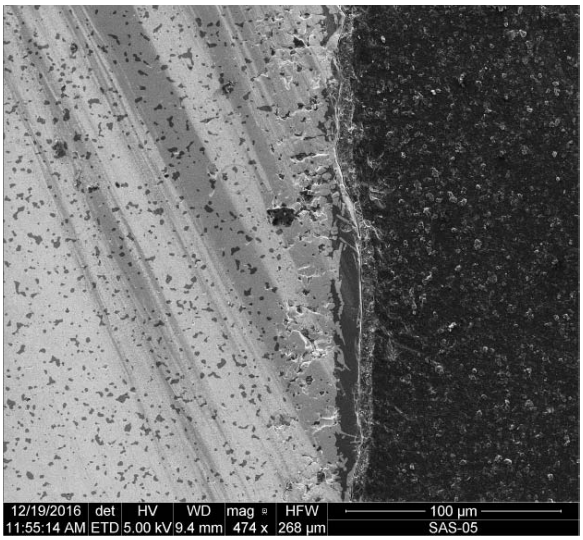

Figure A-75. Cross-sectional SEM micrograph of the HfB_2-10% SiC specimen subjected to 1 h of compression creep at 8 MPa at 1500°C in air (failed upon load-up to 100MPa).

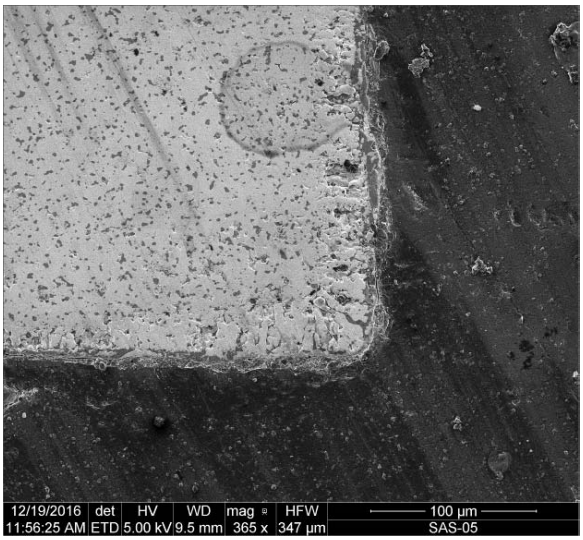

Figure A-76. Cross-sectional SEM micrograph of the HfB_2-10% SiC specimen subjected to 1 h of compression creep at 8 MPa at 1500°C in air (failed upon load-up to 100MPa).

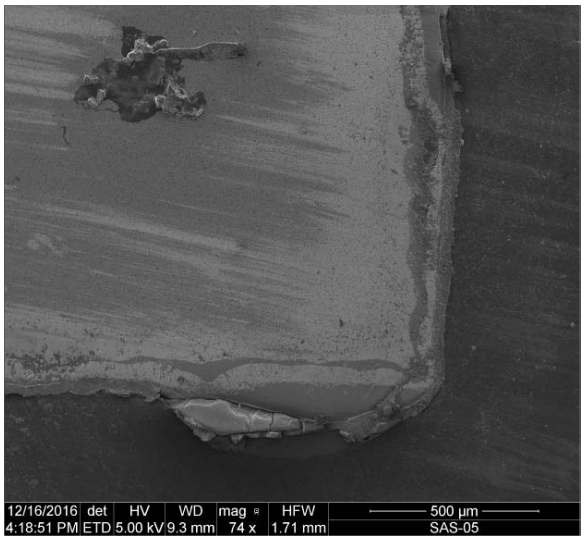

Figure A-77. Cross-sectional SEM micrograph of the HfB_2-10% SiC specimen subjected to 66.3 h of compression creep at 75 MPa at 1500°C.

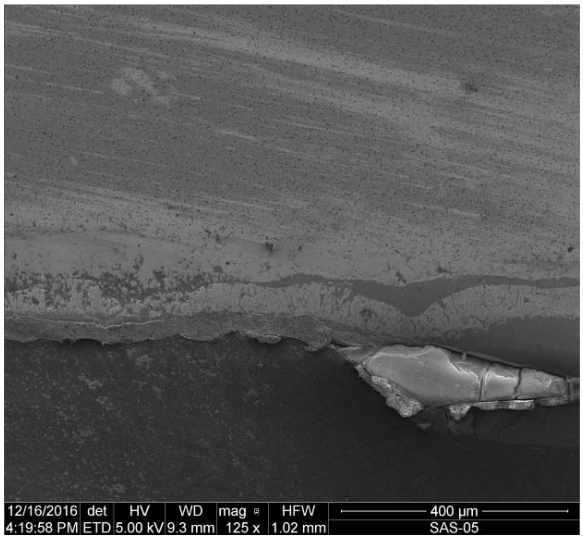

Figure A-78. Cross-sectional SEM micrograph of the HfB_2-10% SiC specimen subjected to 66.3 h of compression creep at 75 MPa at 1500°C.

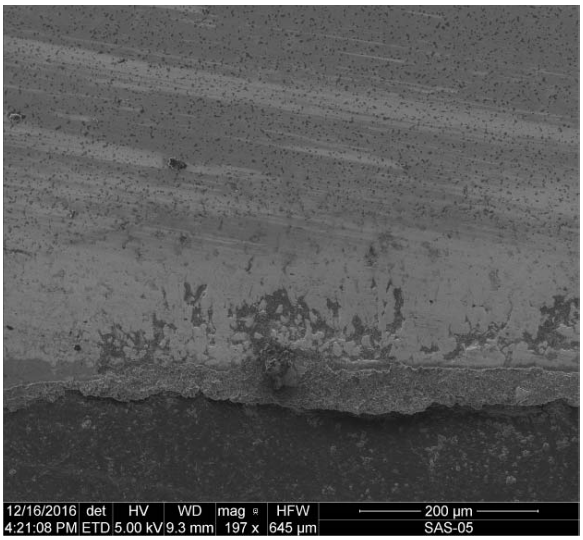

Figure A-79. Cross-sectional SEM micrograph of the HfB_2-10% SiC specimen subjected to 66.3 h of compression creep at 75 MPa at 1500°C.

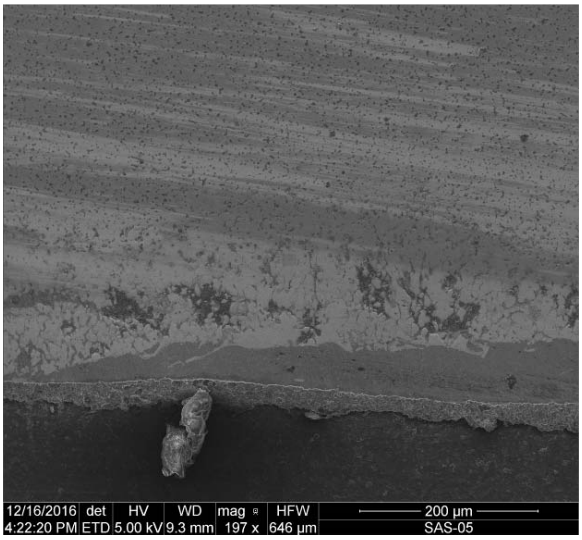

Figure A-80. Cross-sectional SEM micrograph of the HfB_2-10% SiC specimen subjected to 66.3 h of compression creep at 75 MPa at 1500°C.

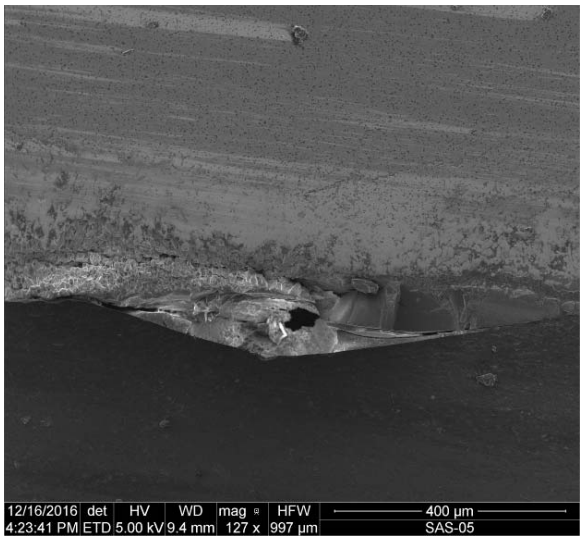

Figure A-81. Cross-sectional SEM micrograph of the HfB_2-10% SiC specimen subjected to 66.3 h of compression creep at 75 MPa at 1500°C.

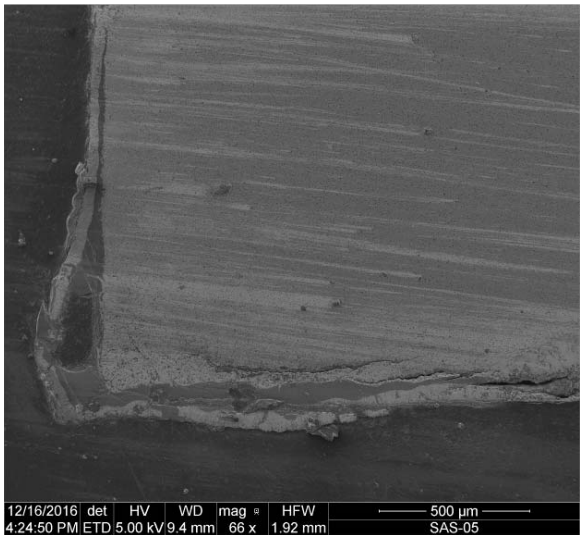

Figure A-82. Cross-sectional SEM micrograph of the HfB_2-10% SiC specimen subjected to 66.3 h of compression creep at 75 MPa at 1500°C.

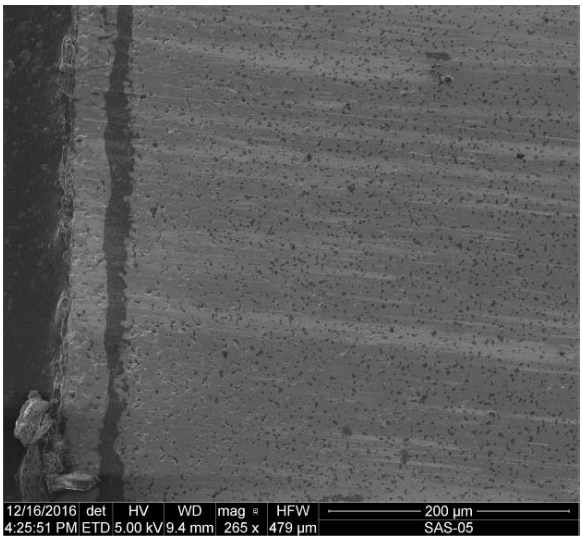

Figure A-83. Cross-sectional SEM micrograph of the HfB_2-10% SiC specimen subjected to 66.3 h of compression creep at 75 MPa at 1500°C.

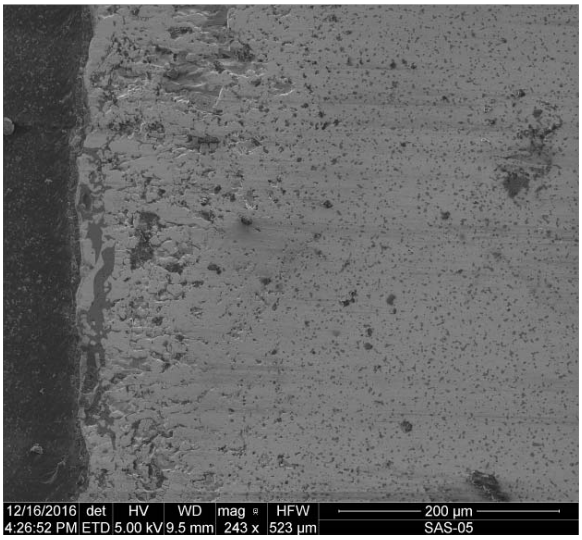

Figure A-84. Cross-sectional SEM micrograph of the HfB_2-10% SiC specimen subjected to 66.3 h of compression creep at 75 MPa at 1500°C.

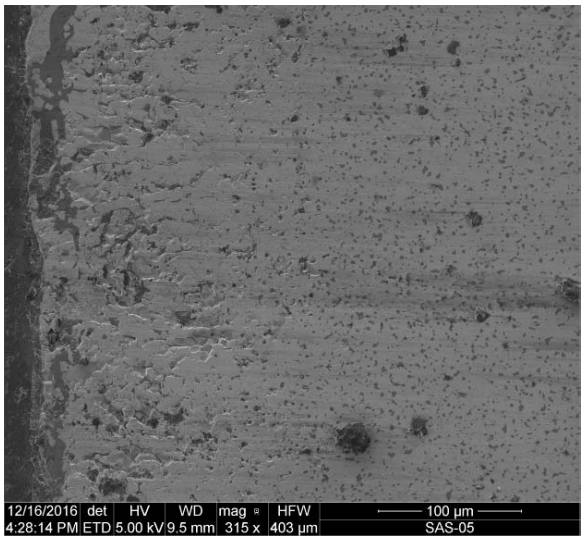

Figure A-85. Cross-sectional SEM micrograph of the HfB_2-10% SiC specimen subjected to 66.3 h of compression creep at 75 MPa at 1500°C.

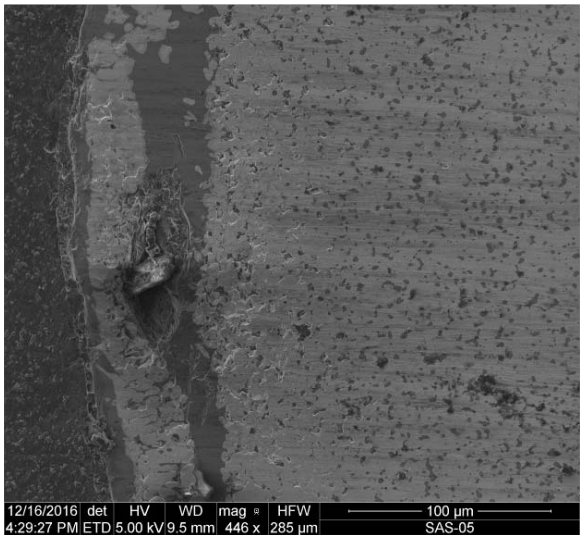

Figure A-86. Cross-sectional SEM micrograph of the HfB_2-10% SiC specimen subjected to 66.3 h of compression creep at 75 MPa at 1500°C.

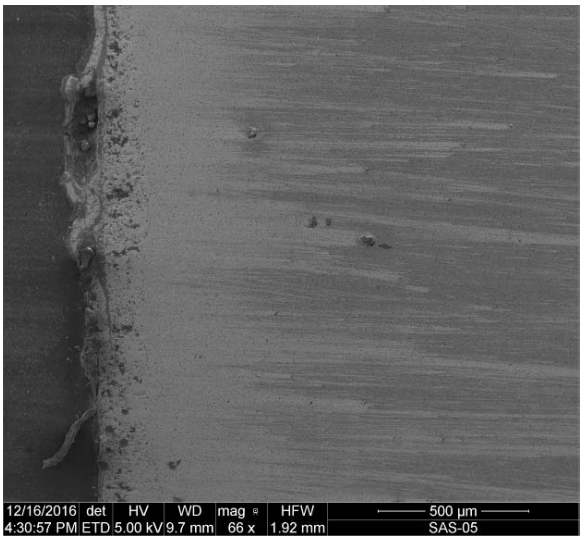

Figure A-87. Cross-sectional SEM micrograph of the HfB_2-10% SiC specimen subjected to 66.3 h of compression creep at 75 MPa at 1500°C.

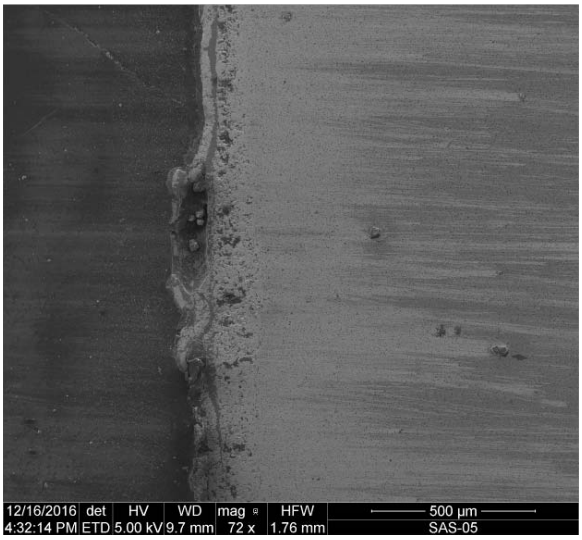

Figure A-88. Cross-sectional SEM micrograph of the HfB_2-10% SiC specimen subjected to 66.3 h of compression creep at 75 MPa at 1500°C.

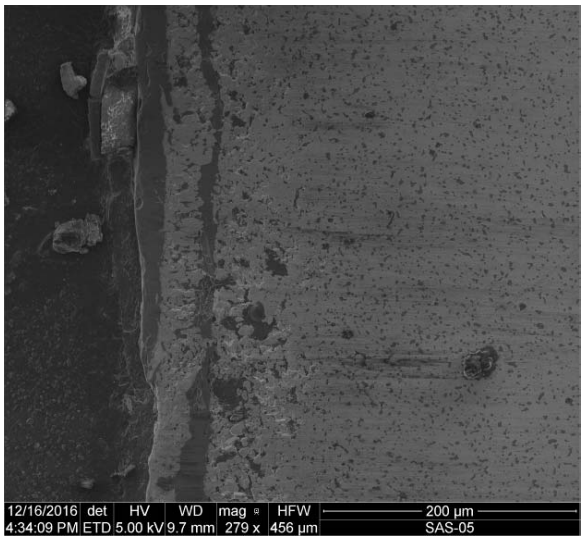

Figure A-89. Cross-sectional SEM micrograph of the HfB_2-10% SiC specimen subjected to 66.3 h of compression creep at 75 MPa at 1500°C.

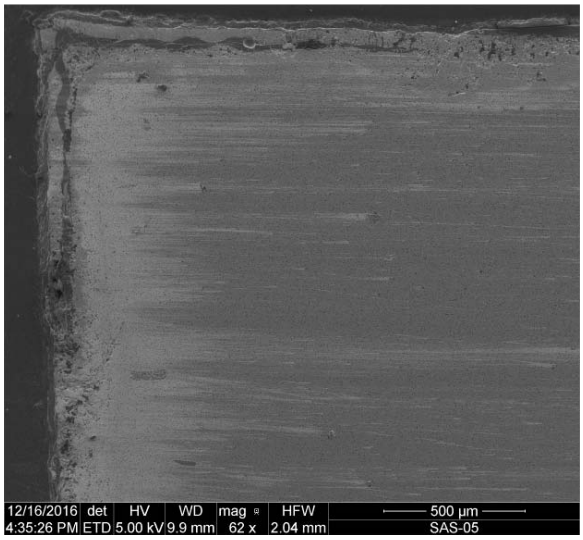

Figure A-90. Cross-sectional SEM micrograph of the HfB_2-10% SiC specimen subjected to 66.3 h of compression creep at 75 MPa at 1500°C.

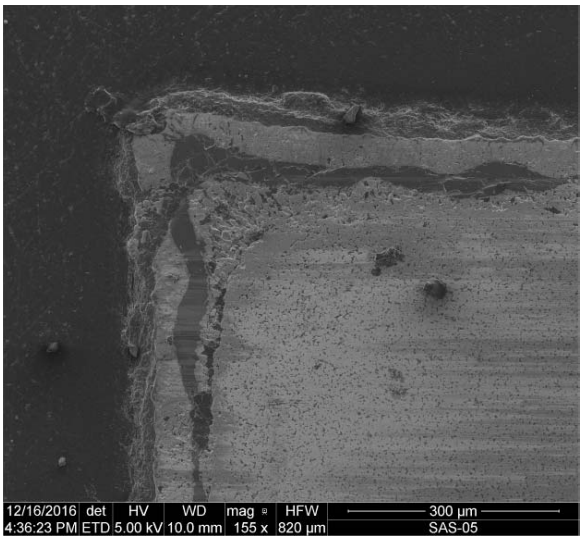

Figure A-91. Cross-sectional SEM micrograph of the HfB_2-10% SiC specimen subjected to 66.3 h of compression creep at 75 MPa at 1500°C.

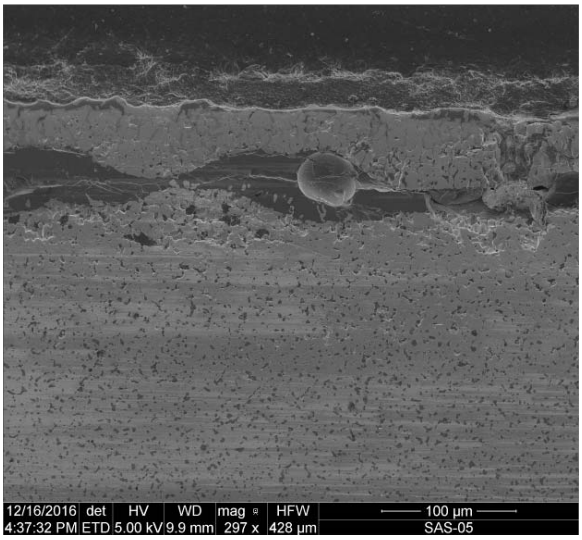

Figure A-92. Cross-sectional SEM micrograph of the HfB_2-10% SiC specimen subjected to 66.3 h of compression creep at 75 MPa at 1500°C.

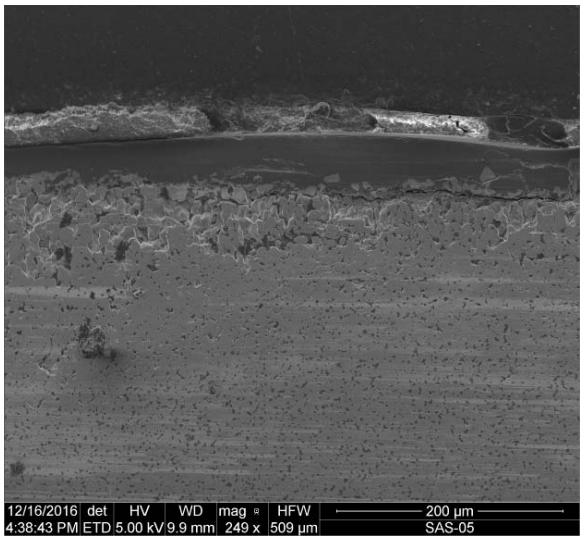

Figure A-93. Cross-sectional SEM micrograph of the HfB_2-10% SiC specimen subjected to 66.3 h of compression creep at 75 MPa at 1500°C.

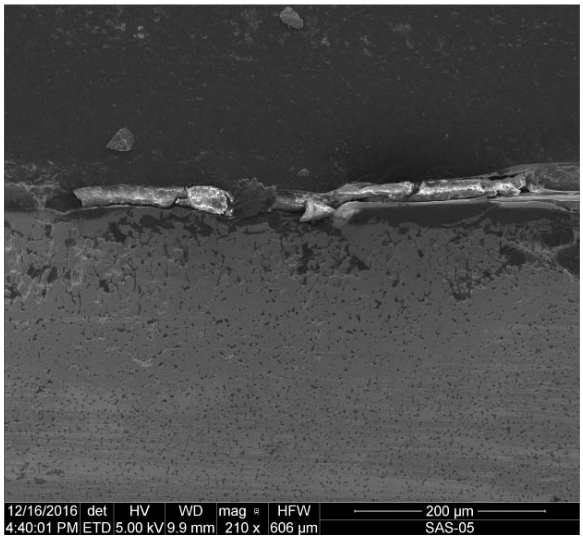

Figure A-94. Cross-sectional SEM micrograph of the HfB_2-10% SiC specimen subjected to 66.3 h of compression creep at 75 MPa at 1500°C.

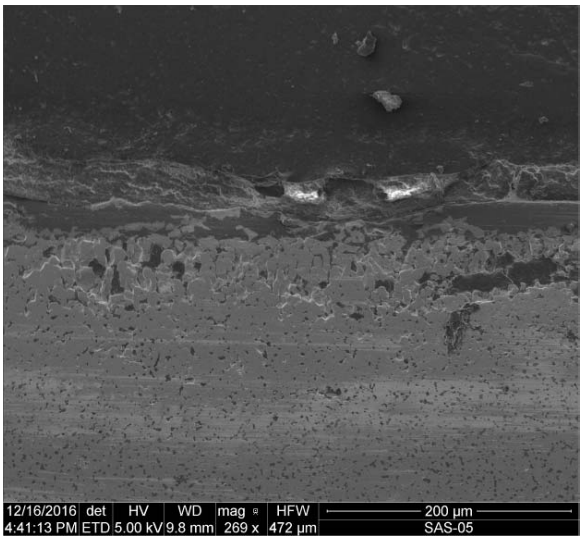

Figure A-95. Cross-sectional SEM micrograph of the HfB_2-10% SiC specimen subjected to 66.3 h of compression creep at 75 MPa at 1500°C.

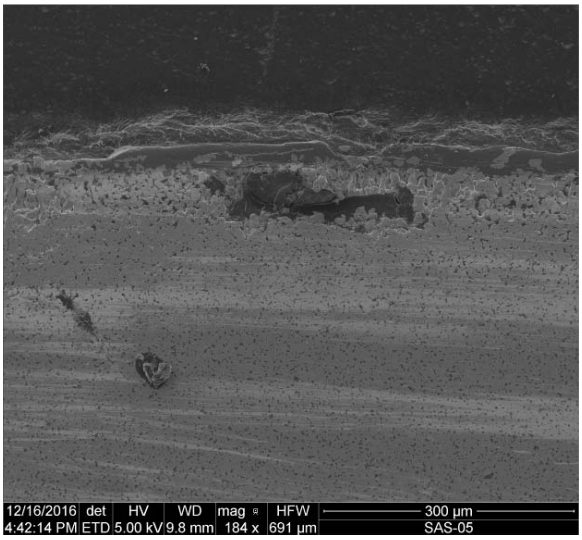

Figure A-96. Cross-sectional SEM micrograph of the HfB_2-10% SiC specimen subjected to 66.3 h of compression creep at 75 MPa at 1500°C.

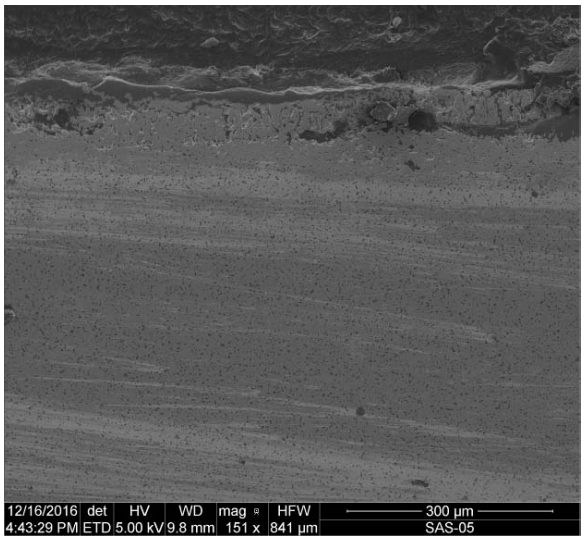

Figure A-97. Cross-sectional SEM micrograph of the HfB_2-10% SiC specimen subjected to 66.3 h of compression creep at 75 MPa at 1500°C.

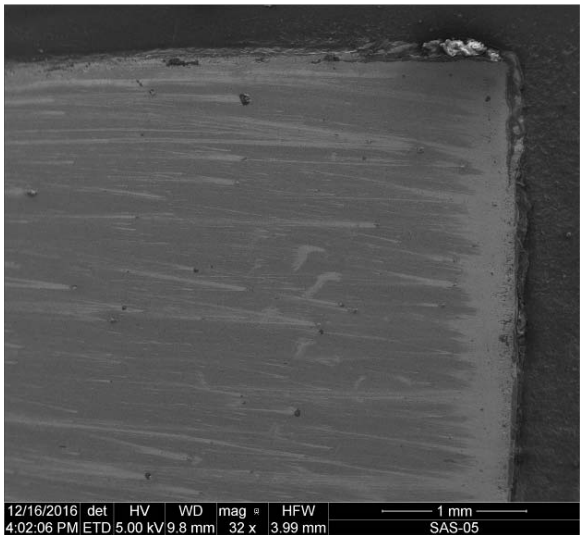

Figure A-98. Cross-sectional SEM micrograph of the HfB_2-10% SiC specimen subjected to 66.3 h of compression creep at 75 MPa at 1500°C.

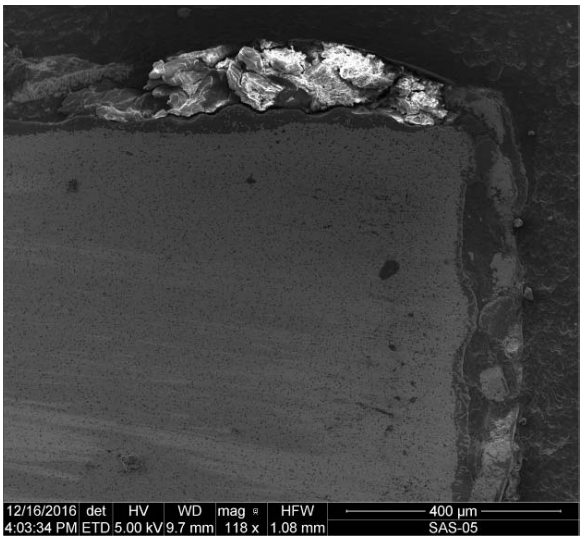

Figure A-99. Cross-sectional SEM micrograph of the HfB_2-10% SiC specimen subjected to 66.3 h of compression creep at 75 MPa at 1500°C.

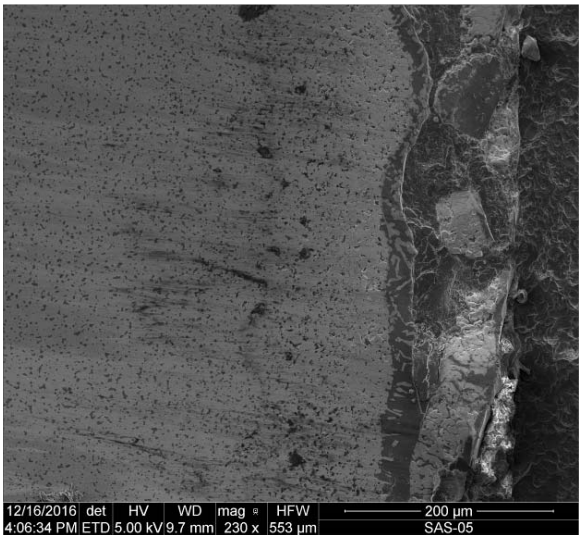

Figure A-100. Cross-sectional SEM micrograph of the HfB_2-10% SiC specimen subjected to 66.3 h of compression creep at 75 MPa at 1500°C.

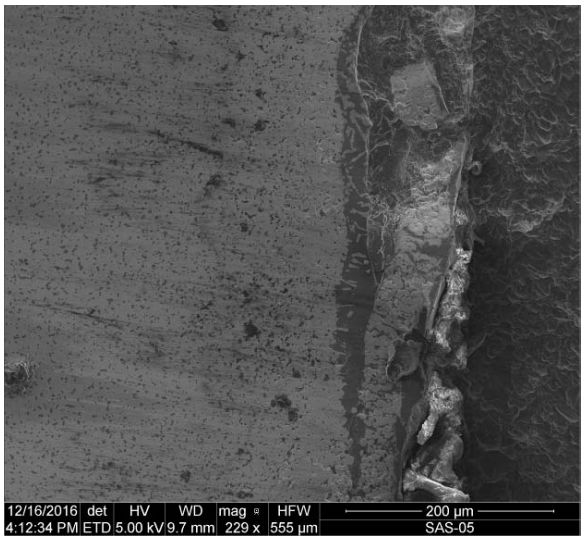

Figure A-101. Cross-sectional SEM micrograph of the HfB_2-10% SiC specimen subjected to 66.3 h of compression creep at 75 MPa at 1500°C.

Figure A-102. Cross-sectional SEM micrograph of the HfB_2-10% SiC specimen subjected to 66.3 h of compression creep at 75 MPa at 1500°C.

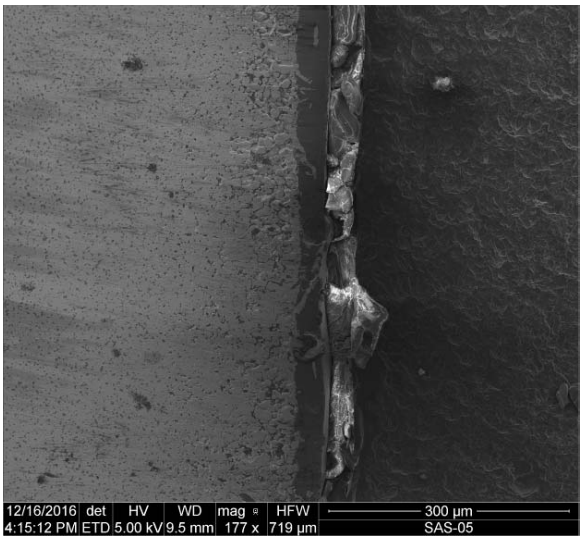

Figure A-103. Cross-sectional SEM micrograph of the HfB_2-10% SiC specimen subjected to 66.3 h of compression creep at 75 MPa at 1500°C.

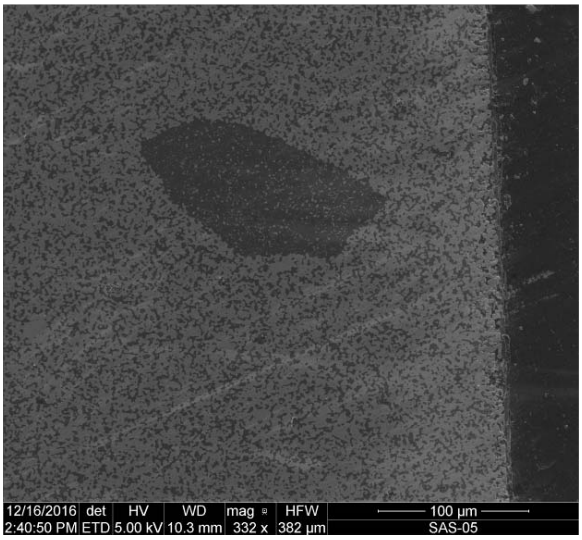

Figure A-104. Cross-sectional SEM micrograph of the HfB_2-30% SiC specimen subjected to 8.8 h of compression creep at 100 MPa at 1500°C. Dark blotch is a high concentration of SiC particles. Similar blotches were noted by Winder and DeGregoria [12, 17].

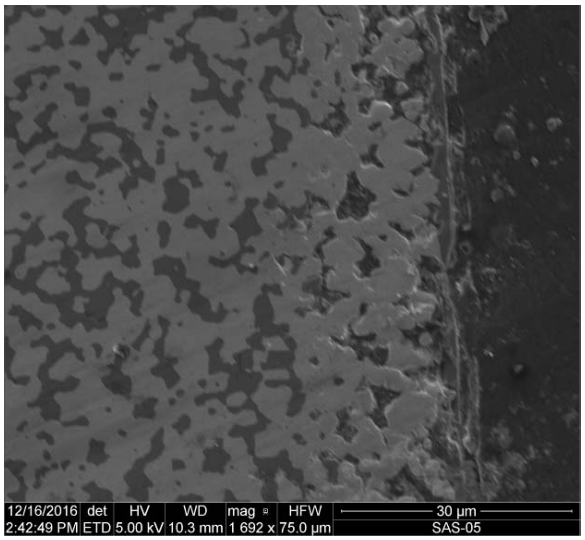

Figure A-105. Cross-sectional SEM micrograph of the HfB_2-30% SiC specimen subjected to 8.8 h of compression creep at 100 MPa at 1500°C.

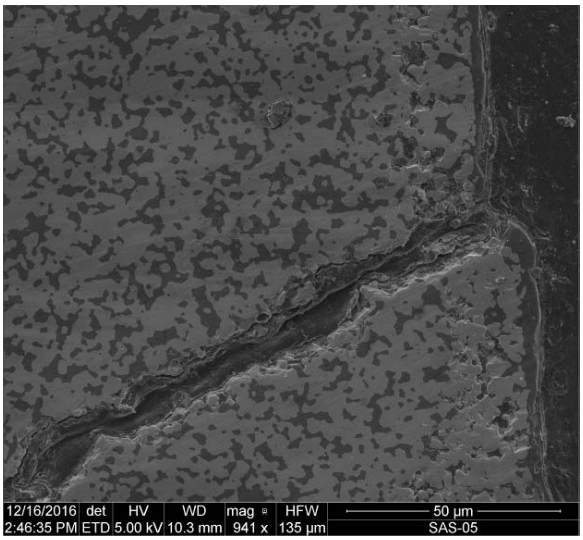

Figure A-107: Cross-sectional SEM micrograph of the HfB_2-30% SiC specimen subjected to 8.8 h of compression creep at 100 MPa at 1500°C.

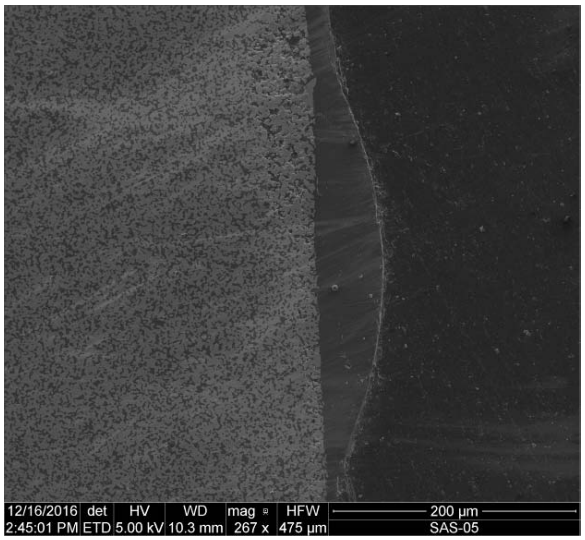

Figure A-106. Cross-sectional SEM micrograph of the HfB_2-30% SiC specimen subjected to 8.8 h of compression creep at 100 MPa at 1500°C.

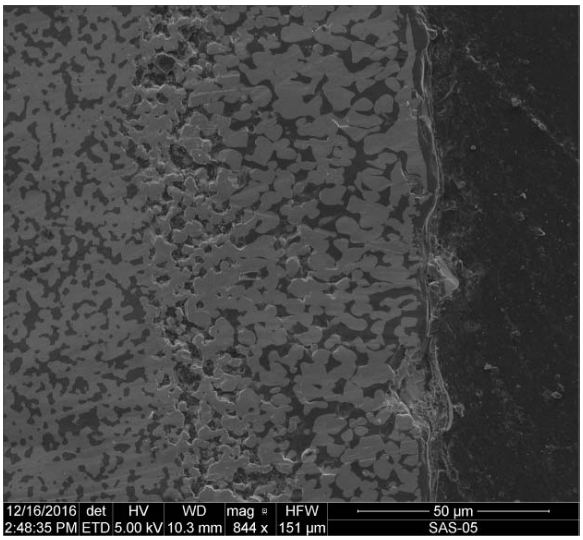

Figure A-108. Cross-sectional SEM micrograph of the HfB_2-30% SiC specimen subjected to 8.8 h of compression creep at 100 MPa at 1500°C.

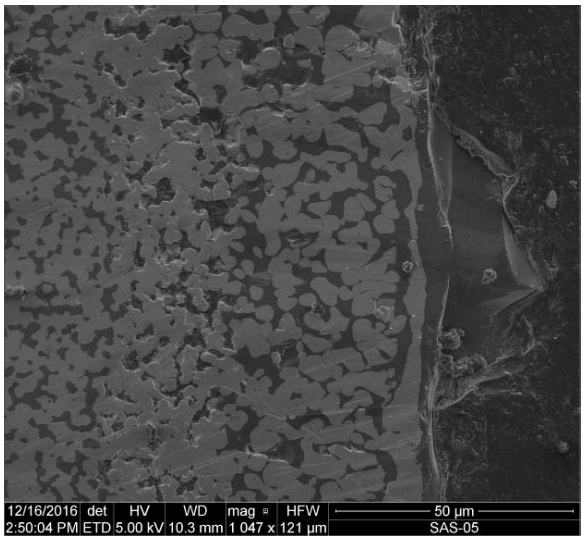

Figure A-109. Cross-sectional SEM micrograph of the HfB_2-30% SiC specimen subjected to 8.8 h of compression creep at 100 MPa at 1500°C.

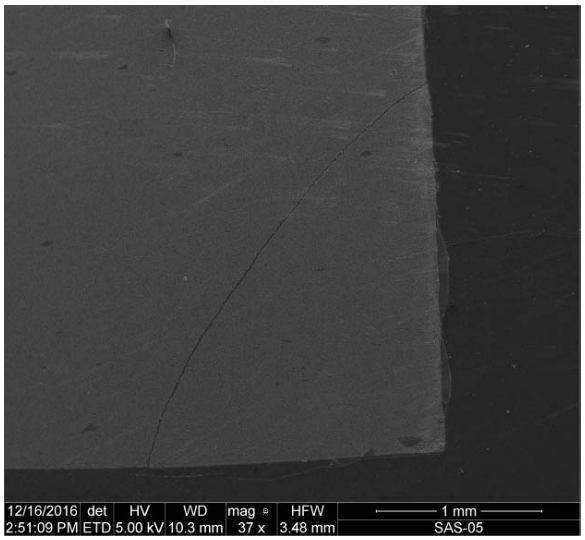

Figure A-110. Cross-sectional SEM micrograph of the HfB_2-30% SiC specimen subjected to 8.8 h of compression creep at 100 MPa at 1500°C.

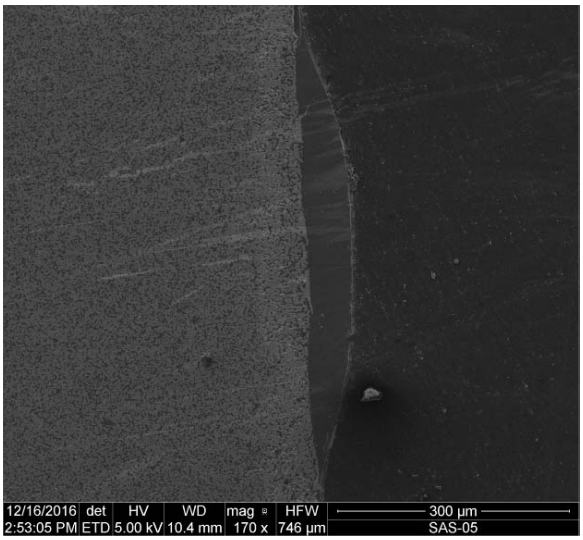

Figure A-111. Cross-sectional SEM micrograph of the HfB_2-30% SiC specimen subjected to 8.8 h of compression creep at 100 MPa at 1500°C.

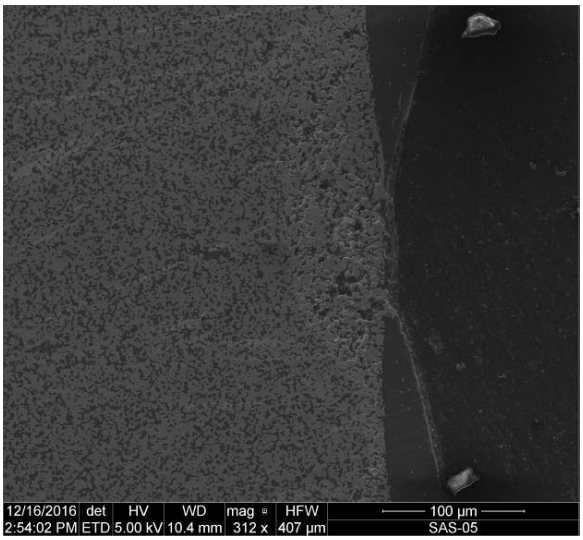

Figure A-112. Cross-sectional SEM micrograph of the HfB_2-30% SiC specimen subjected to 8.8 h of compression creep at 100 MPa at 1500°C.

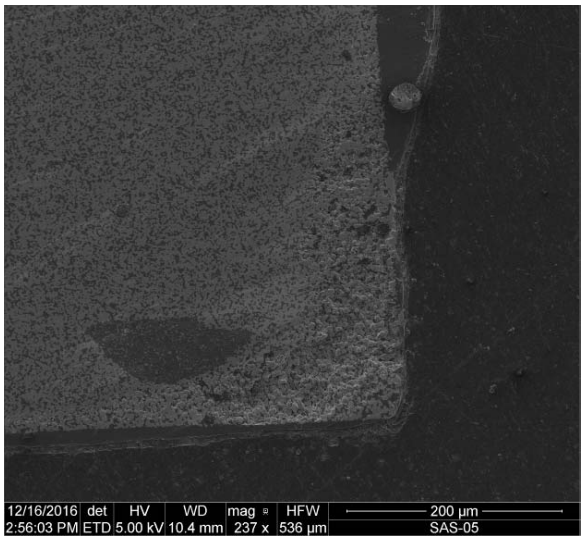

Figure A-113. Cross-sectional SEM micrograph of the HfB_2-30% SiC specimen subjected to 8.8 h of compression creep at 100 MPa at 1500°C.

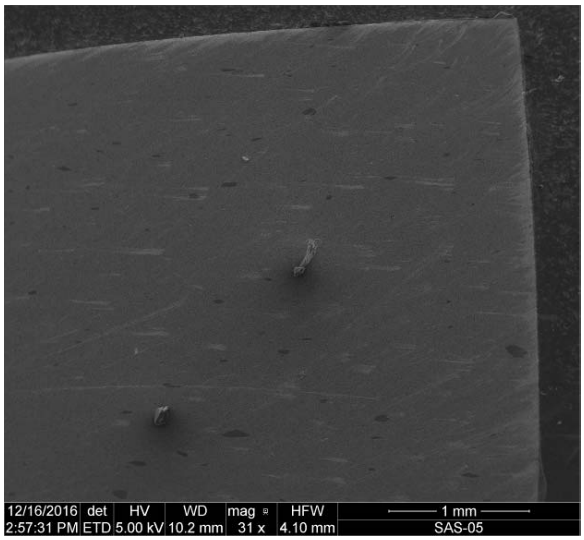

Figure A-114. Cross-sectional SEM micrograph of the HfB_2-30% SiC specimen subjected to 8.8 h of compression creep at 100 MPa at 1500°C.

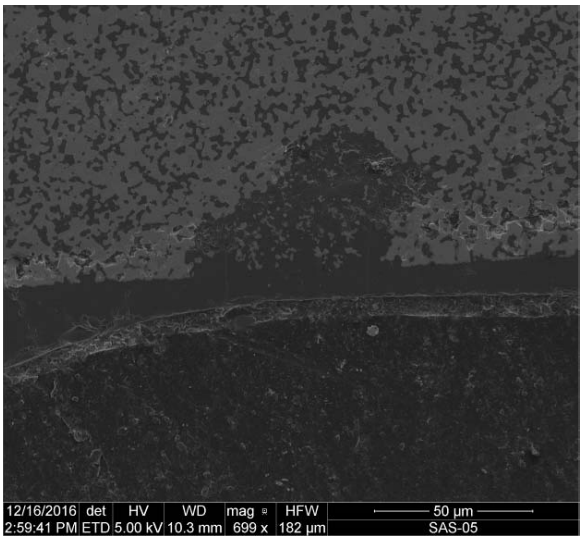

Figure A-115. Cross-sectional SEM micrograph of the HfB_2-30% SiC specimen subjected to 8.8 h of compression creep at 100 MPa at 1500°C.

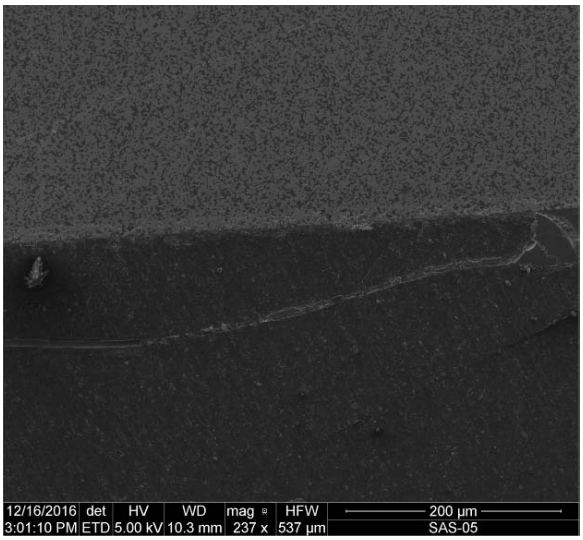

Figure A-116. Cross-sectional SEM micrograph of the HfB_2-30% SiC specimen subjected to 8.8 h of compression creep at 100 MPa at 1500°C.

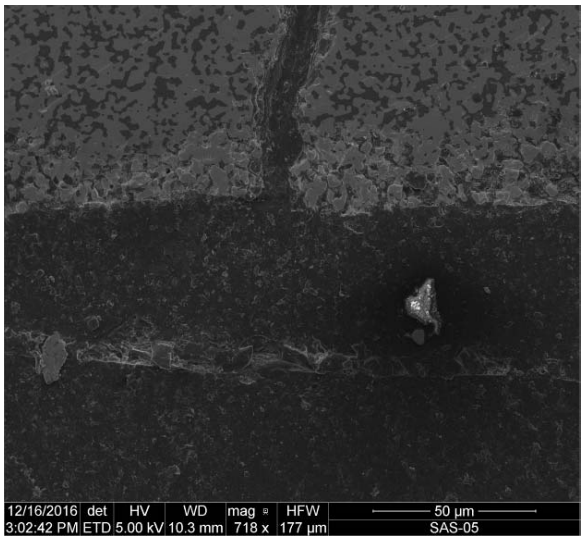

Figure A-117. Cross-sectional SEM micrograph of the HfB_2-30% SiC specimen subjected to 8.8 h of compression creep at 100 MPa at 1500°C.

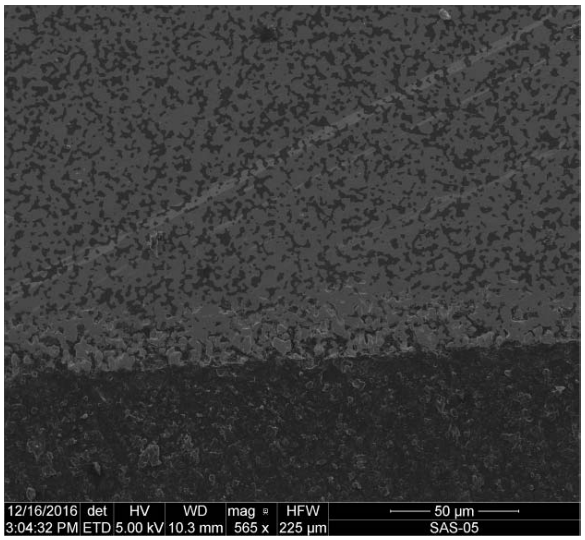

Figure A-118. Cross-sectional SEM micrograph of the HfB_2-30% SiC specimen subjected to 8.8 h of compression creep at 100 MPa at 1500°C.

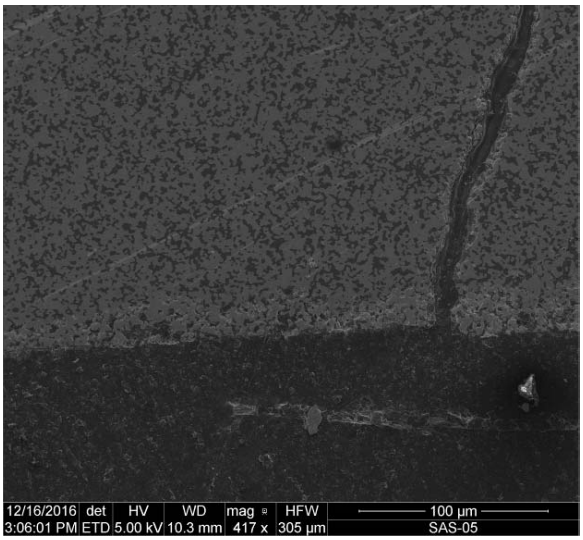

Figure A-119. Cross-sectional SEM micrograph of the HfB_2-30% SiC specimen subjected to 8.8 h of compression creep at 100 MPa at 1500°C.

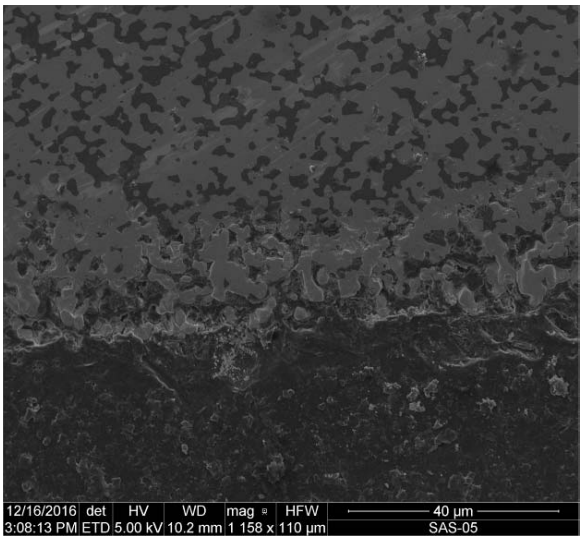

Figure A-120. Cross-sectional SEM micrograph of the HfB_2-30% SiC specimen subjected to 8.8 h of compression creep at 100 MPa at 1500°C.

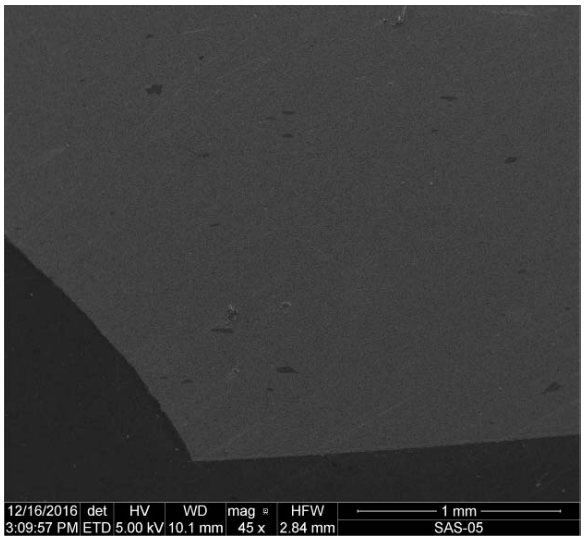

Figure A-121. Cross-sectional SEM micrograph of the HfB_2-30% SiC specimen subjected to 8.8 h of compression creep at 100 MPa at 1500°C.

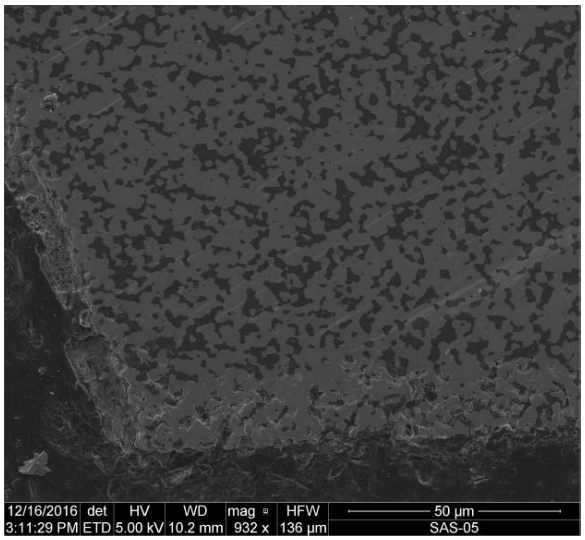

Figure A-122. Cross-sectional SEM micrograph of the HfB_2-30% SiC specimen subjected to 8.8 h of compression creep at 100 MPa at 1500°C.

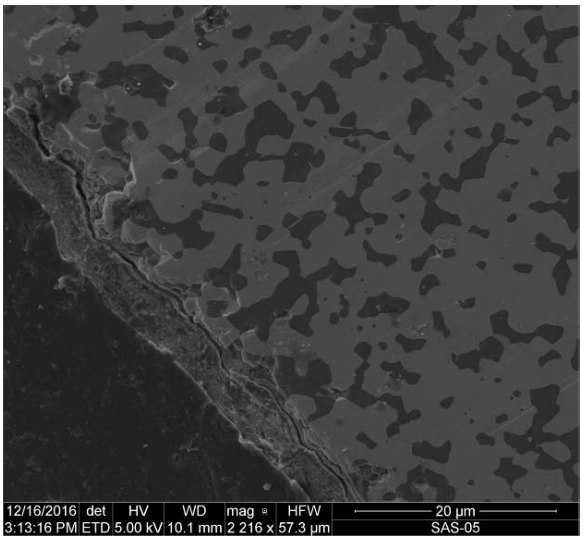

Figure A-123. Cross-sectional SEM micrograph of the HfB_2-30% SiC specimen subjected to 8.8 h of compression creep at 100 MPa at 1500°C.

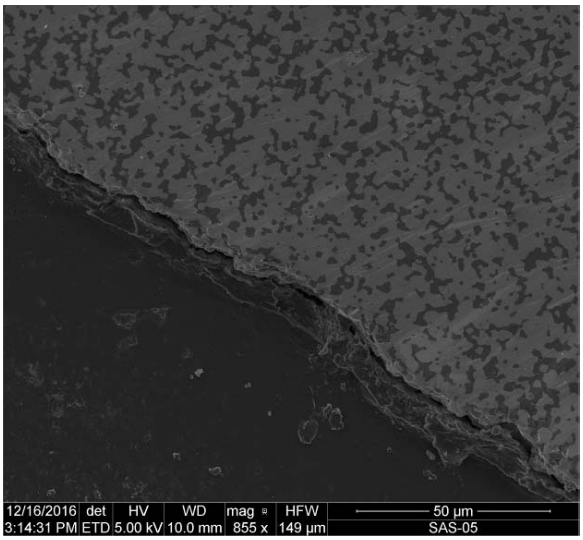

Figure A-124. Cross-sectional SEM micrograph of the HfB_2-30% SiC specimen subjected to 8.8 h of compression creep at 100 MPa at 1500°C.

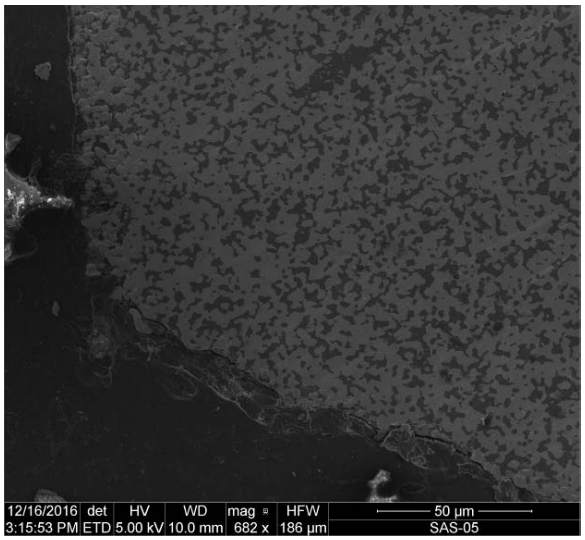

Figure A-125. Cross-sectional SEM micrograph of the HfB_2-30% SiC specimen subjected to 8.8 h of compression creep at 100 MPa at 1500°C.

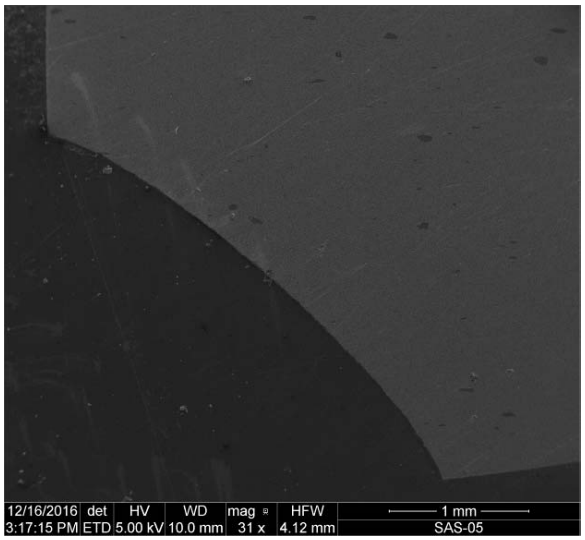

Figure A-126. Cross-sectional SEM micrograph of the HfB_2-30% SiC specimen subjected to 8.8 h of compression creep at 100 MPa at 1500°C.

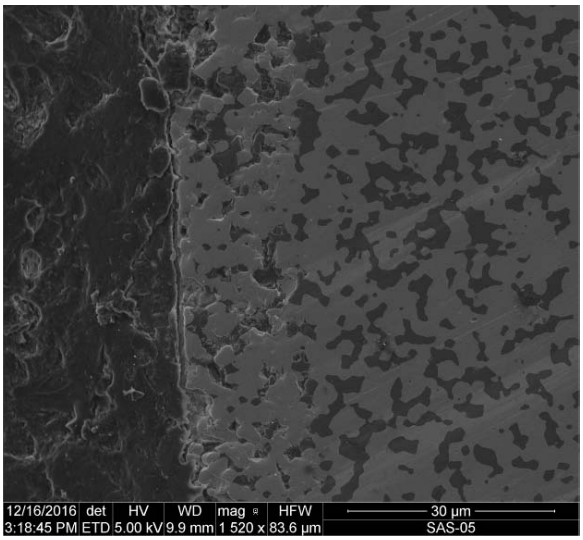

Figure A-127. Cross-sectional SEM micrograph of the HfB_2-30% SiC specimen subjected to 8.8 h of compression creep at 100 MPa at 1500°C.

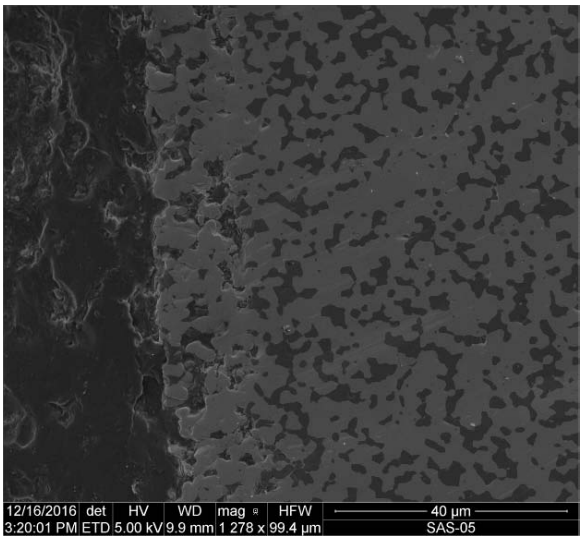

Figure A-128. Cross-sectional SEM micrograph of the HfB_2-30% SiC specimen subjected to 8.8 h of compression creep at 100 MPa at 1500°C.

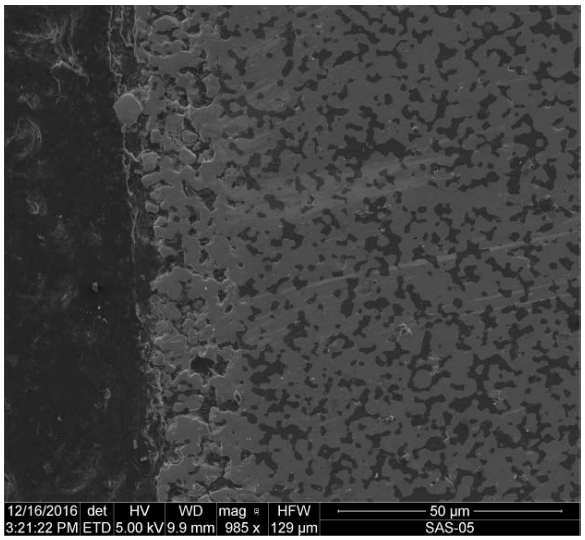

Figure A-129. Cross-sectional SEM micrograph of the HfB_2-30% SiC specimen subjected to 8.8 h of compression creep at 100 MPa at 1500°C.

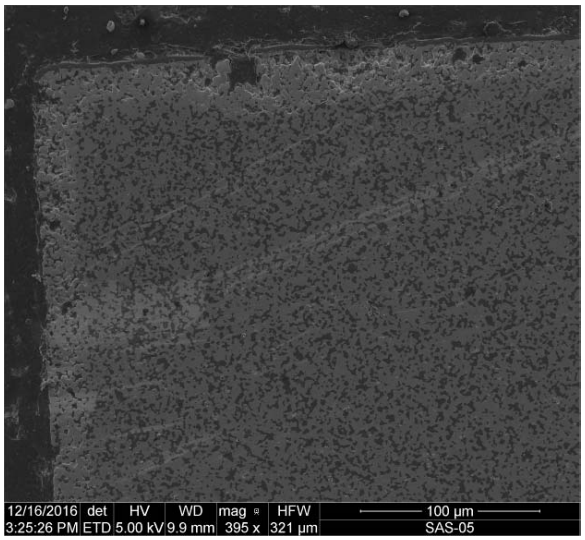

Figure A-130. Cross-sectional SEM micrograph of the HfB_2-30% SiC specimen subjected to 8.8 h of compression creep at 100 MPa at 1500°C.

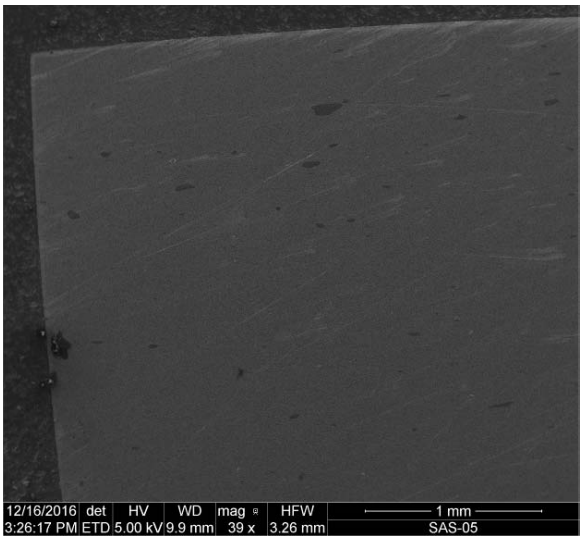

Figure A-131. Cross-sectional SEM micrograph of the HfB_2-30% SiC specimen subjected to 8.8 h of compression creep at 100 MPa at 1500°C.

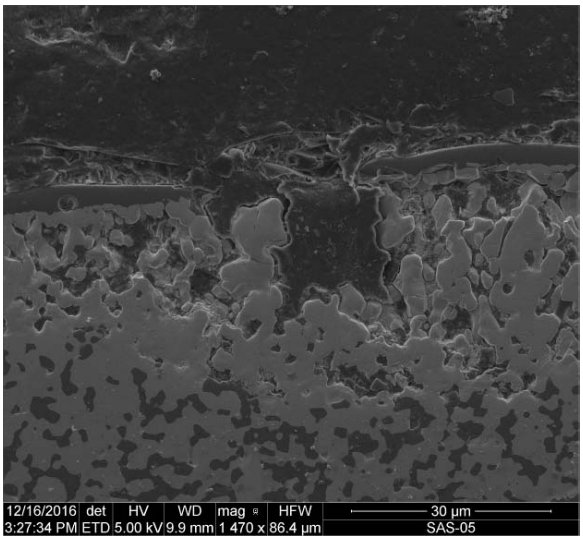

Figure A-132. Cross-sectional SEM micrograph of the HfB_2-30% SiC specimen subjected to 8.8 h of compression creep at 100 MPa at 1500°C.

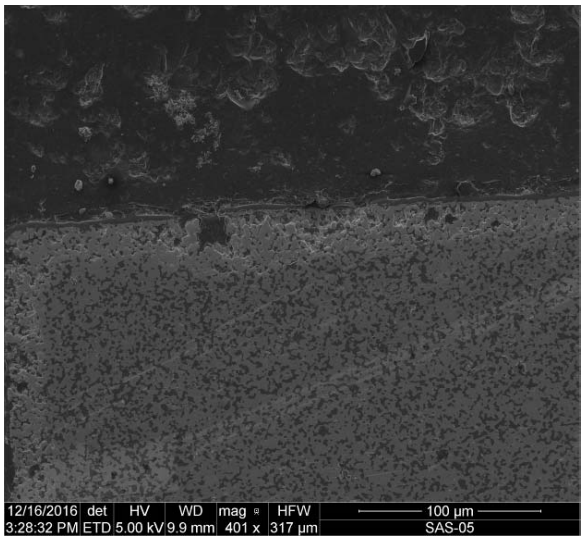

Figure A-133. Cross-sectional SEM micrograph of the HfB_2-30% SiC specimen subjected to 8.8 h of compression creep at 100 MPa at 1500°C.

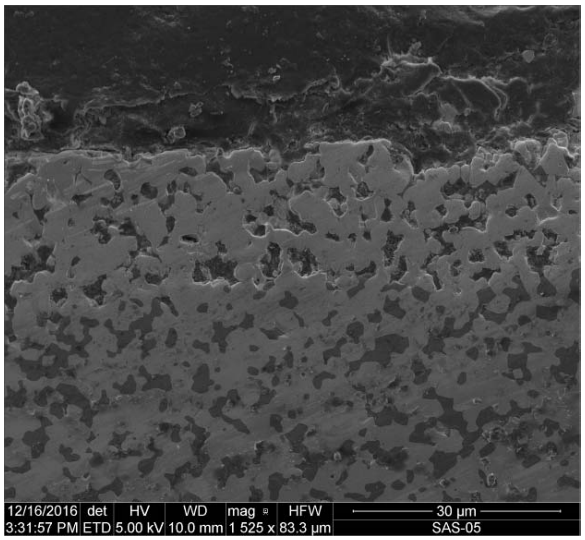

Figure A-134. Cross-sectional SEM micrograph of the HfB_2-30% SiC specimen subjected to 8.8 h of compression creep at 100 MPa at 1500°C.

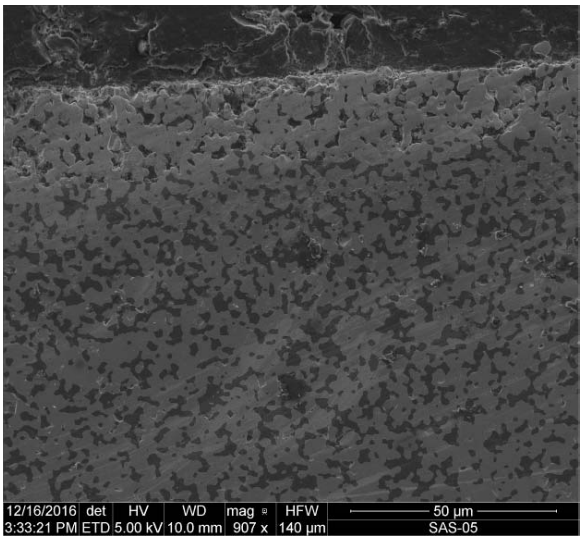

Figure A-135. Cross-sectional SEM micrograph of the HfB_2-30% SiC specimen subjected to 8.8 h of compression creep at 100 MPa at 1500°C.

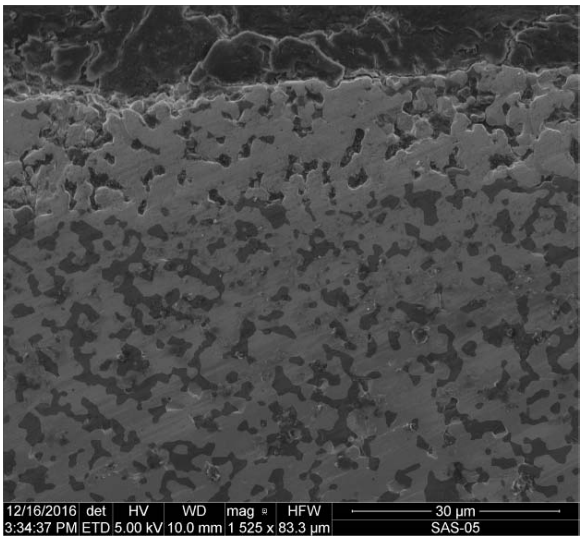

Figure A-136. Cross-sectional SEM micrograph of the HfB_2-30% SiC specimen subjected to 8.8 h of compression creep at 100 MPa at 1500°C.

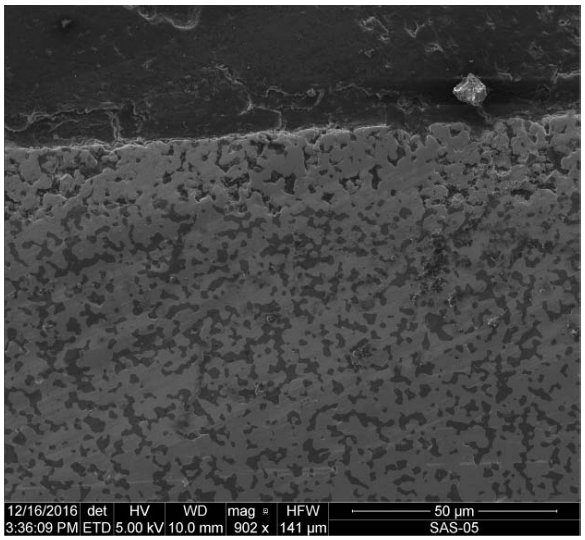

Figure A-137. Cross-sectional SEM micrograph of the HfB_2-30% SiC specimen subjected to 8.8 h of compression creep at 100 MPa at 1500°C.

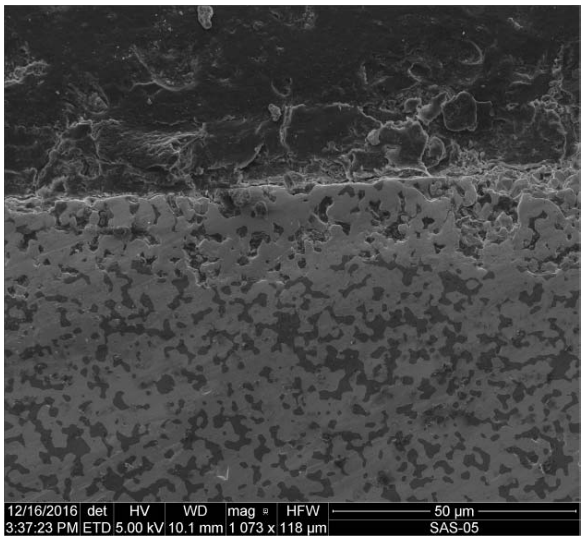

Figure A-138. Cross-sectional SEM micrograph of the HfB_2-30% SiC specimen subjected to 8.8 h of compression creep at 100 MPa at 1500°C.

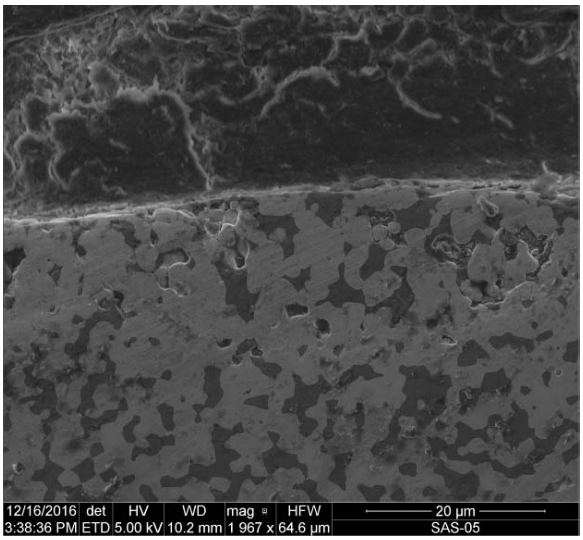

Figure A-139. Cross-sectional SEM micrograph of the HfB_2-30% SiC specimen subjected to 8.8 h of compression creep at 100 MPa at 1500°C.

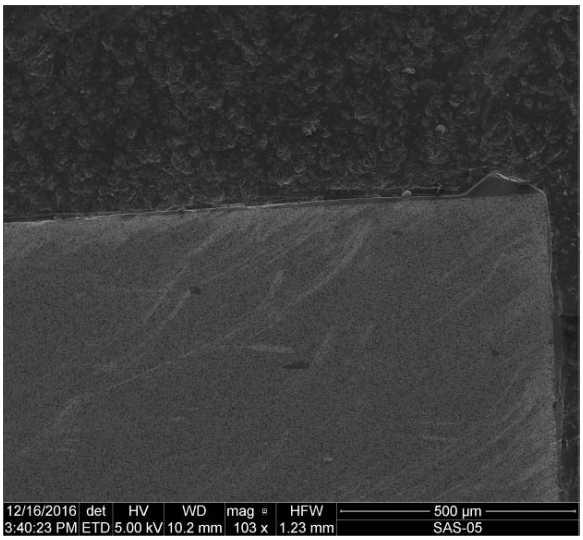

Figure A-140. Cross-sectional SEM micrograph of the HfB_2-30% SiC specimen subjected to 8.8 h of compression creep at 100 MPa at 1500°C.

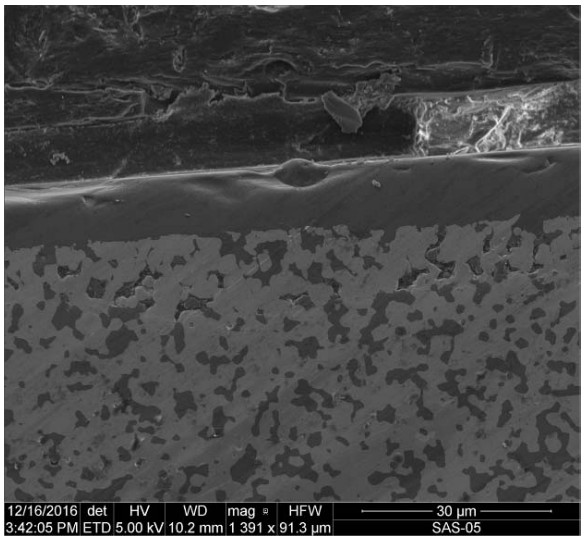

Figure A-141. Cross-sectional SEM micrograph of the HfB_2-30% SiC specimen subjected to 8.8 h of compression creep at 100 MPa at 1500°C.

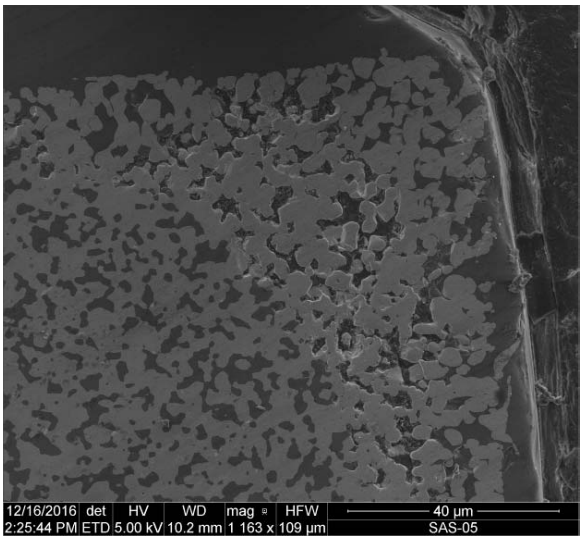

Figure A-143. Cross-sectional SEM micrograph of the HfB_2-30% SiC specimen subjected to 8.8 h of compression creep at 100 MPa at 1500°C.

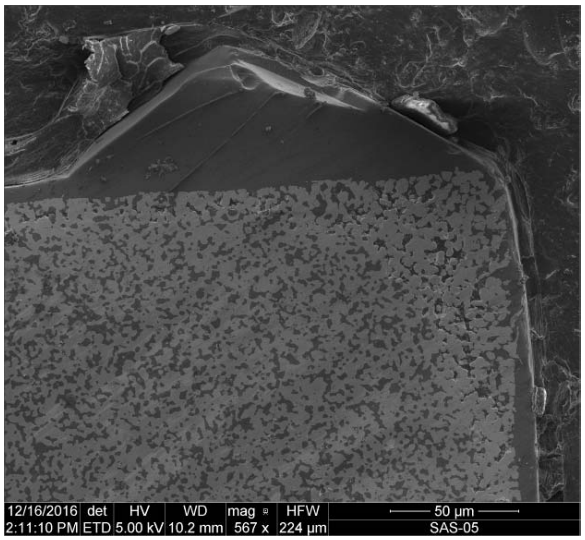

Figure A-142. Cross-sectional SEM micrograph of the HfB_2-30% SiC specimen subjected to 8.8 h of compression creep at 100 MPa at 1500°C.

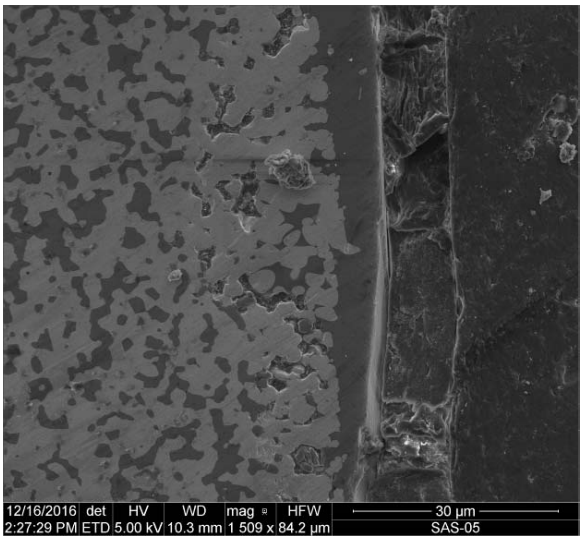

Figure A-144. Cross-sectional SEM micrograph of the HfB_2-30% SiC specimen subjected to 8.8 h of compression creep at 100 MPa at 1500°C.

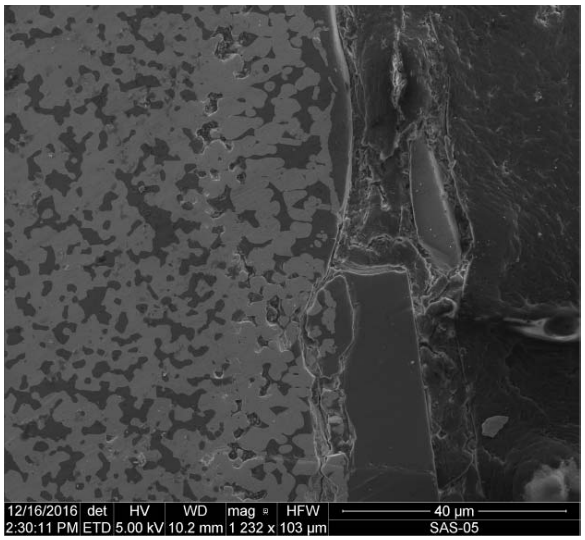

Figure A-145. Cross-sectional SEM micrograph of the HfB_2-30% SiC specimen subjected to 8.8 h of compression creep at 100 MPa at 1500°C.

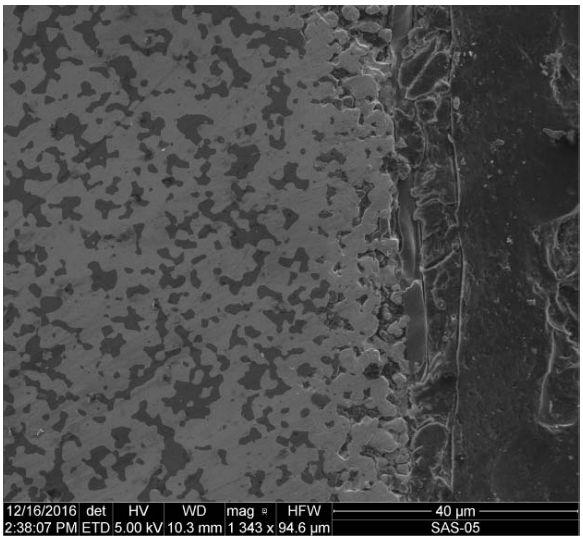

Figure A-147. Cross-sectional SEM micrograph of the HfB_2-30% SiC specimen subjected to 8.8 h of compression creep at 100 MPa at 1500°C.

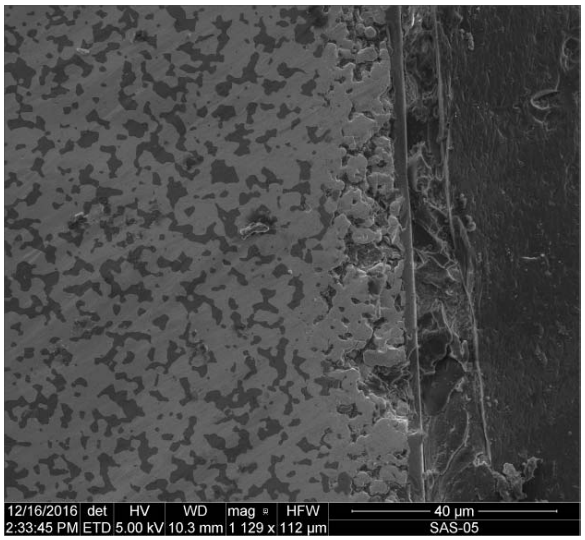

Figure A-146. Cross-sectional SEM micrograph of the HfB_2-30% SiC specimen subjected to 8.8 h of compression creep at 100 MPa at 1500°C.

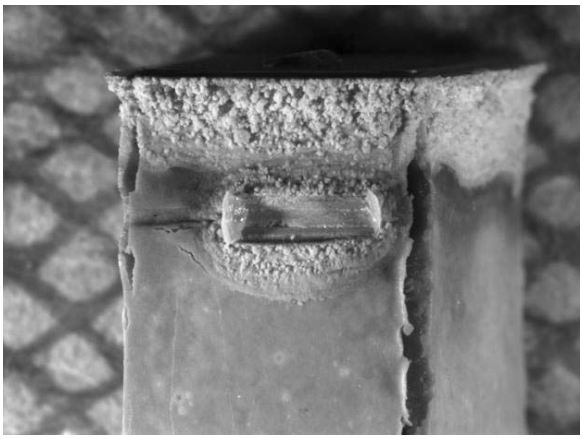

Figure A-148. Optical micrograph of the HfB_2 specimen subjected to 20 h of compression creep at 75 MPa at 1500°C. Note the scale buildup and discoloration near ends. Depression at extensometer groove includes two broken pieces of sapphire extensometer rod.

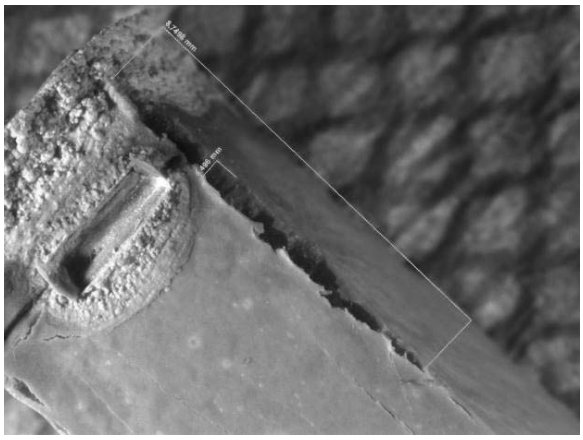

Figure A-149. Optical micrograph of the HfB_2 specimen subjected to 20 h of compression creep at 75 MPa at 1500°C. Scale cracking at corners was common with test specimens, particularly monolithic HfB_2.

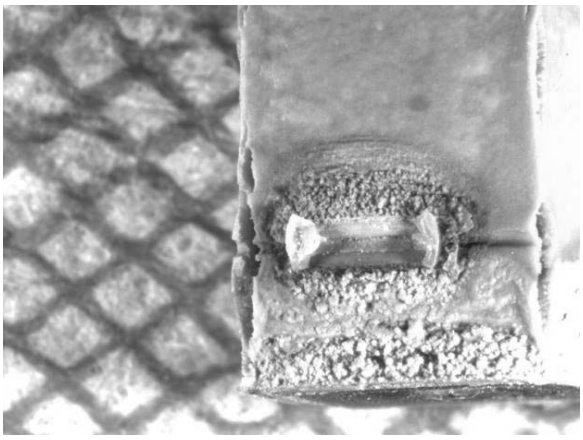

Figure A-151. Optical micrograph of the HfB_2 specimen subjected to 30 h of compression creep at 75 MPa at 1500°C. Note the scale buildup and discoloration near ends. Depression at extensometer groove includes two broken pieces of sapphire extensometer rod.

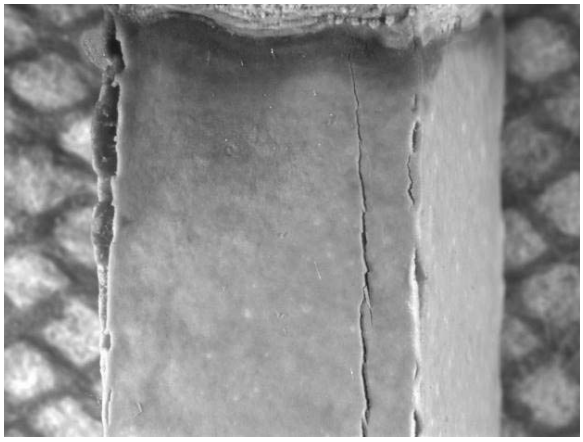

Figure A-150. Optical micrograph of the HfB_2 specimen subjected to 20 h of compression creep at 75 MPa at 1500°C.

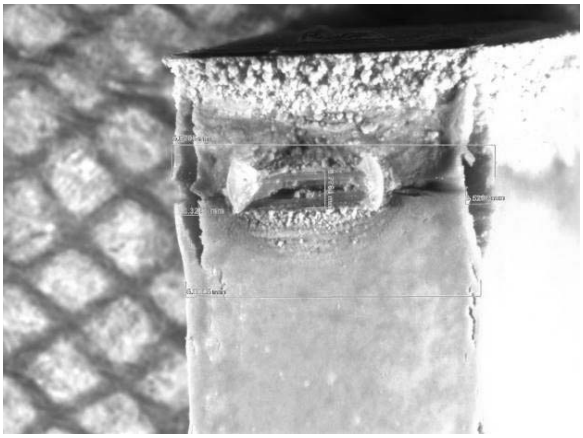

Figure A-152. Optical micrograph of the HfB_2 specimen subjected to 30 h of compression creep at 75 MPa at 1500°C. Note the scale buildup and discoloration near ends. Depression at extensometer groove includes two broken pieces of sapphire extensometer rod.

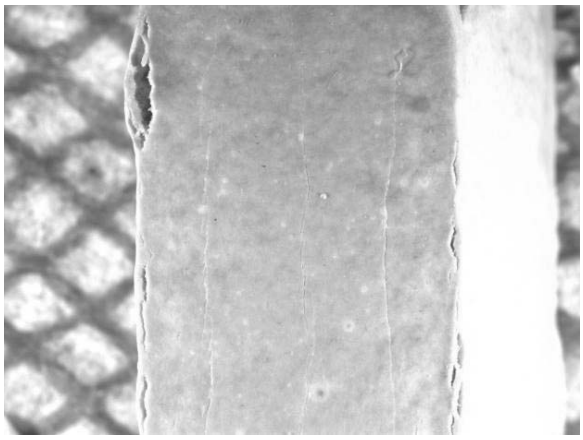

Figure A-153. Optical micrograph of the HfB_2 specimen subjected to 30 h of compression creep at 75 MPa at 1500°C.

Figure A-154. Optical micrograph of the HfB_2 specimen subjected to 30 h of compression creep at 75 MPa at 1500°C.

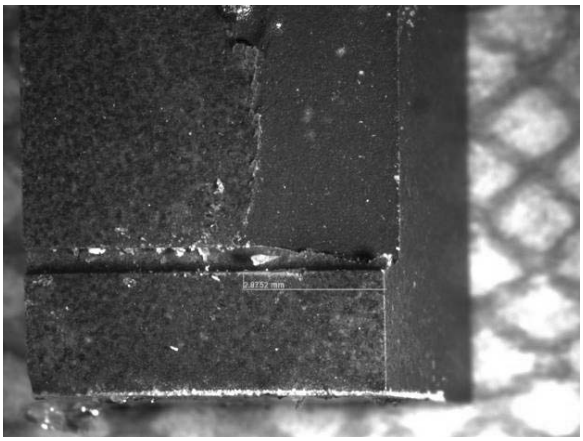

Figure A-155. Optical micrograph of the HfB_2 -10% SiC specimen subjected to 1 h of compression creep at 8 MPa at 1500°C (spacer failure upon load up to 100MPa). Specimen sheared to precut extensometer groove, exhibiting brittle behavior common in ceramics.

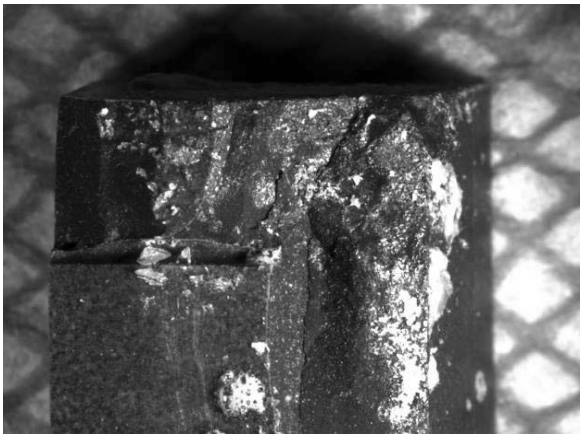

Figure A-156. Optical micrograph of the HfB_2 -10% SiC specimen subjected to 1 h of compression creep at 8 MPa at 1500°C (spacer failure upon load up to 100MPa).

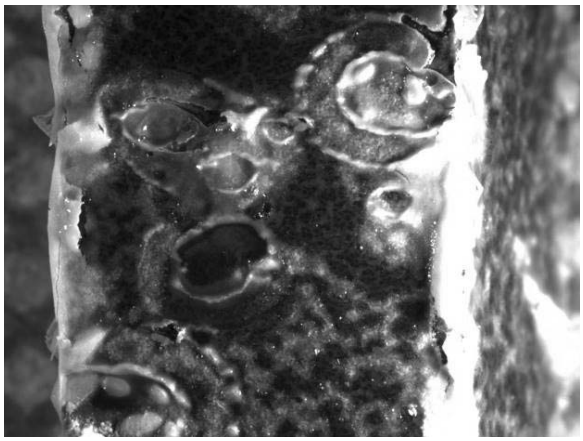

Figure A-157. Optical micrograph of the HfB_2 -10% SiC specimen subjected to 66.3 h of compression creep at 75 MPa at 1500°C. Note boria ruptures reflected in scale.

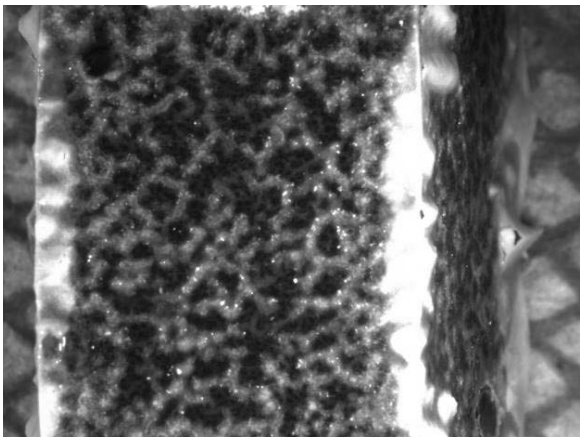

Figure A-159. Optical micrograph of the HfB_2 -10% SiC specimen subjected to 66.3 h of compression creep at 75 MPa at 1500°C.

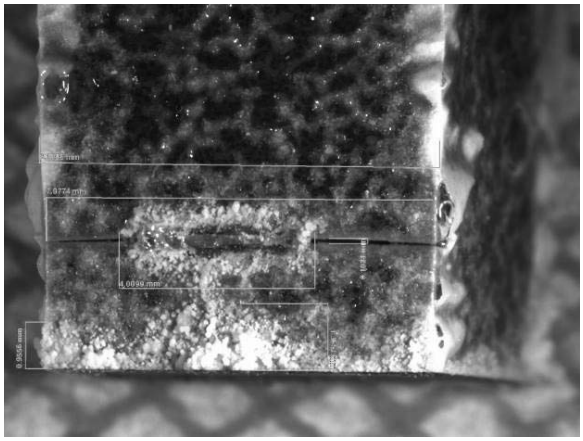

Figure A-158. Optical micrograph of the HfB_2 -10% SiC specimen subjected to 66.3 h of compression creep at 75 MPa at 1500°C. Note crushed extensometer groove due to 12% strain.

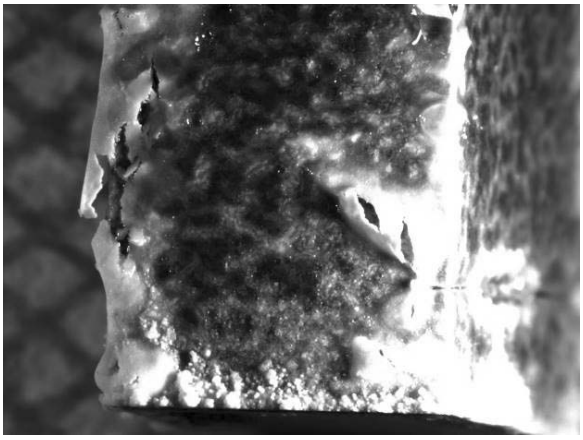

Figure A-160. Optical micrograph of the HfB_2 -10% SiC specimen subjected to 66.3 h of compression creep at 75 MPa at 1500°C. Note scale separation near corners.

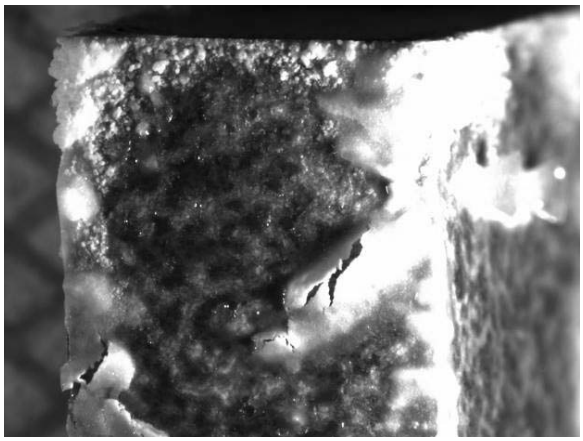

Figure A-161. Optical micrograph of the HfB_2 -10% SiC specimen subjected to 66.3 h of compression creep at 75 MPa at 1500°C.

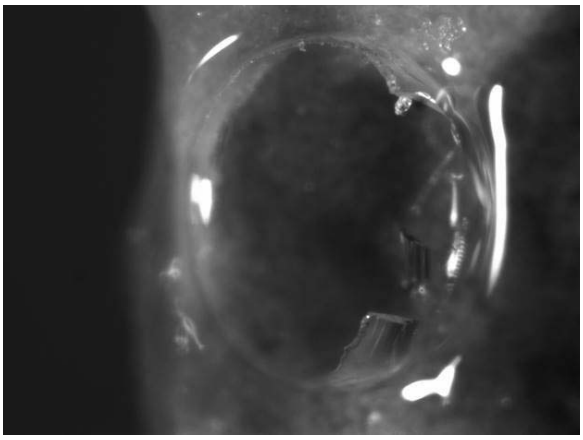

Figure A-162. Optical micrograph of the HfB_2 -10% SiC specimen subjected to 66.3 h of compression creep at 75 MPa at 1500°C. Boria bubble burst.

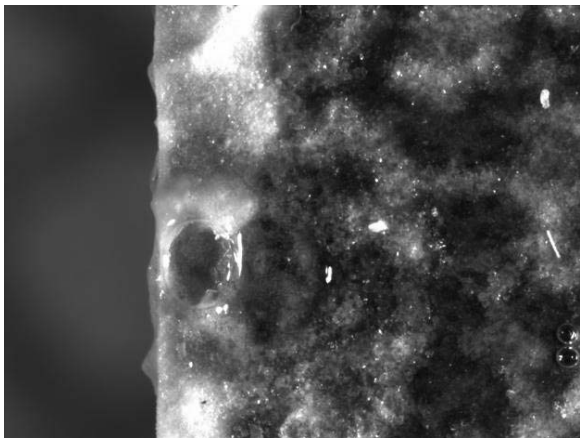

Figure A-162. Optical micrograph of the HfB_2 -10% SiC specimen subjected to 66.3 h of compression creep at 75 MPa at 1500°C.

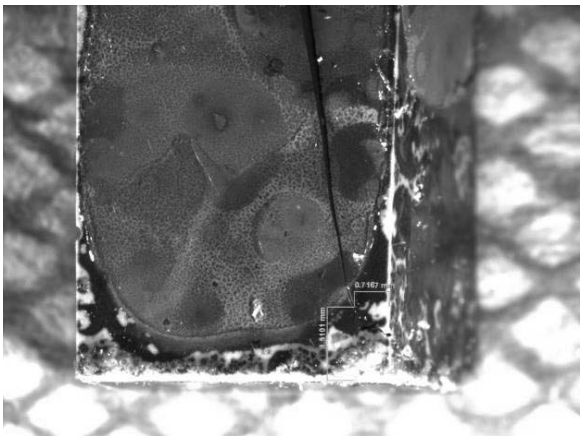

Figure A-163. Optical micrograph of the HfB_2 -30% SiC specimen subjected to 8.8 h of compression creep at 100 MPa at 1500°C. Note crack in specimen.

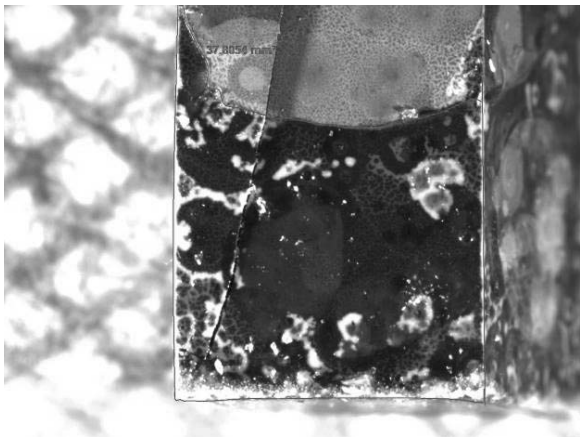

Figure A-164. Optical micrograph of the HfB_2 -30% SiC specimen subjected to 8.8 h of compression creep at 100 MPa at 1500°C. Note discoloration between surface scale reflecting non-uniform oxidation.

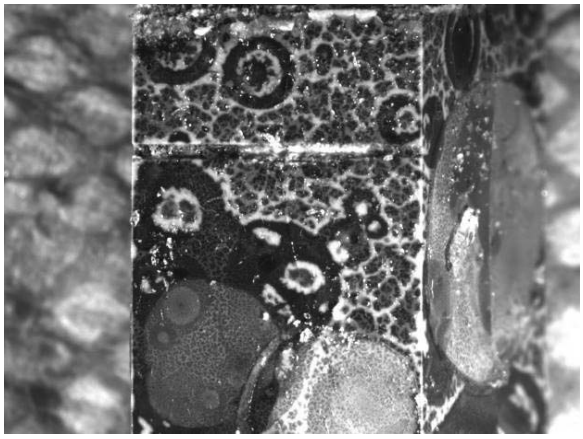

Figure A-165. Optical micrograph of the HfB_2 -30% SiC specimen subjected to 8.8 h of compression creep at 100 MPa at 1500°C.

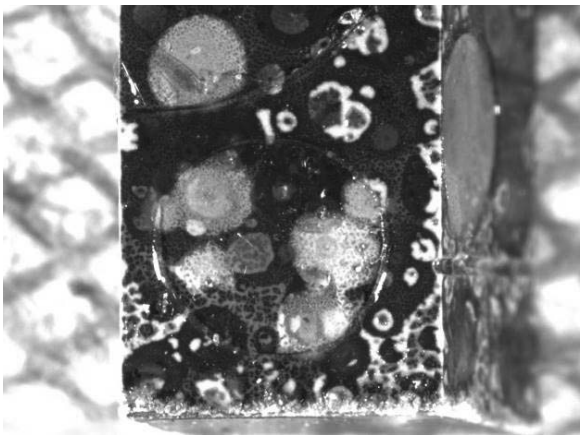

Figure A-166. Optical micrograph of the HfB_2 -30% SiC specimen subjected to 8.8 h of compression creep at 100 MPa at 1500°C.

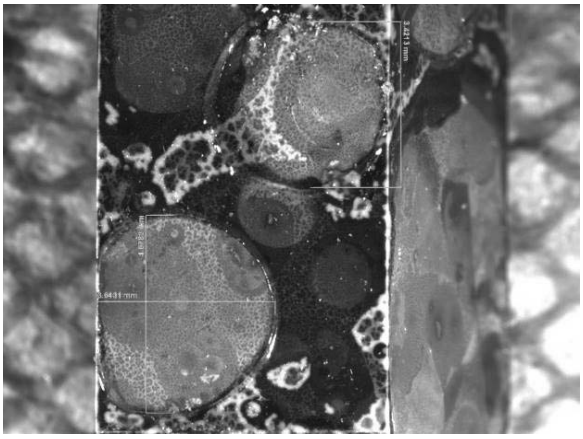

Figure A-167. Optical micrograph of the HfB_2 -30% SiC specimen subjected to 8.8 h of compression creep at 100 MPa at1500°C.

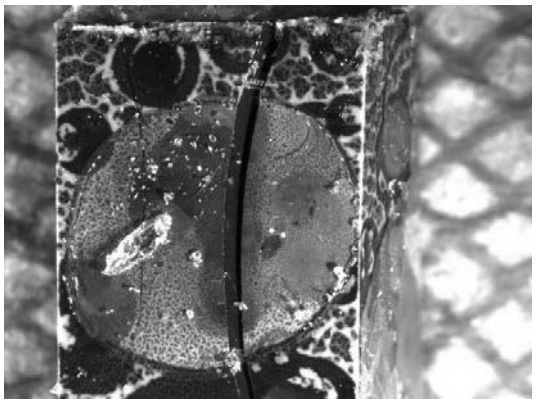

Figure A-168. Optical micrograph of the HfB_2-30% SiC specimen subjeted to 8.8 h of compression creep at 100 MPa at 1500°C. Note crack in specimen

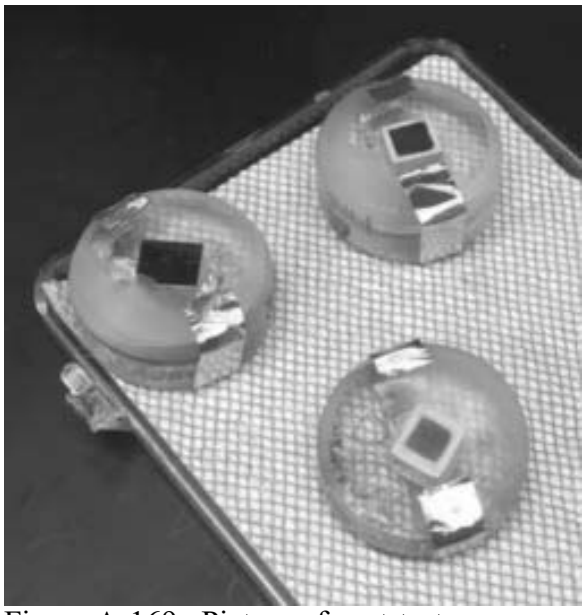

Figure A-169. Picture of post-test specimens prepared for SEM imagery.

Figure A-170. Picture of HfB_2-30% SiC specimen subjected to 100 MPa compressive creep stress for 8.8 h at 1500°C.

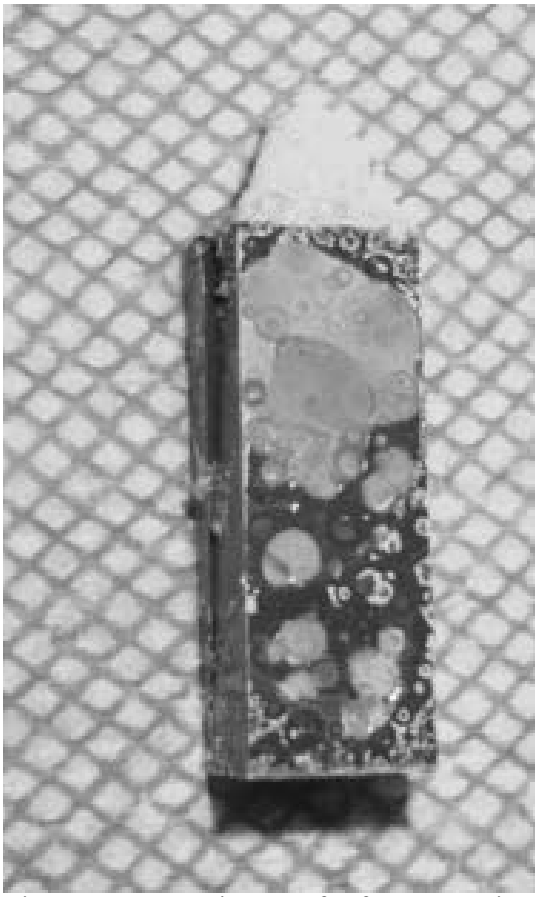

Figure A-171. Picture of HfB_2-30% SiC specimen subjected to 100 MPa compressive creep stress for 8.8 h at 1500°C.

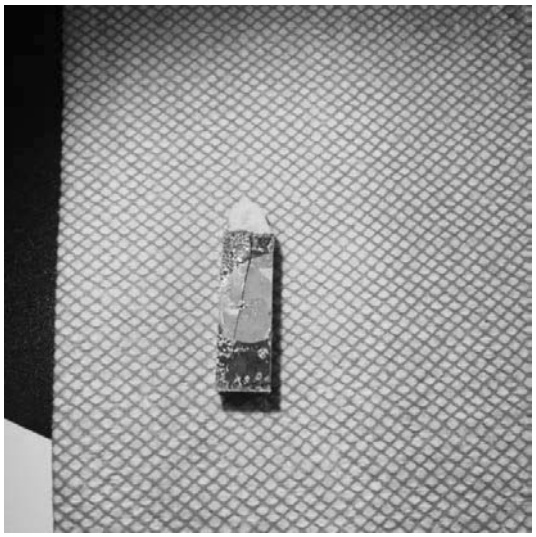

Figure A-172. Picture of HfB_2-30% SiC specimen subjected to 100 MPa compressive creep stress for 8.8 h at 1500°C.

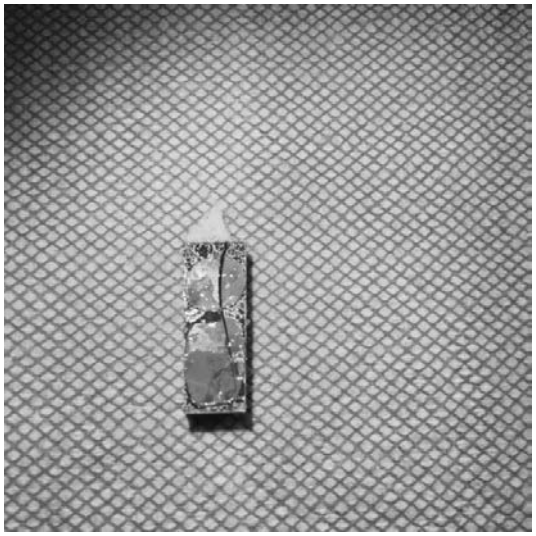

Figure A-173. Picture of HfB_2-30% SiC specimen subjected to 100 MPa compressive creep stress for 8.8 h at 1500°C.

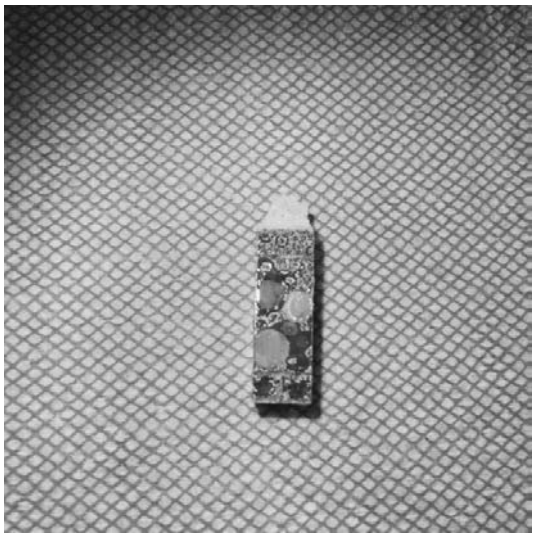

Figure A-174. Picture of HfB_2-30% SiC specimen subjected to 100 MPa compressive creep stress for 8.8 h at 1500°C.

Figure A-175. Picture of HfB_2 specimen subjected to 75 MPa compressive creep stress for 20 h at 1500°C.

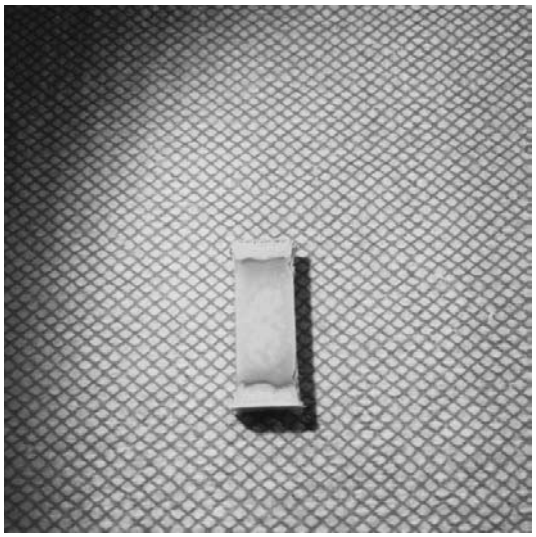

Figure A-176. Picture of HfB_2 specimen subjected to 75 MPa compressive creep stress for 20 h at 1500°C.

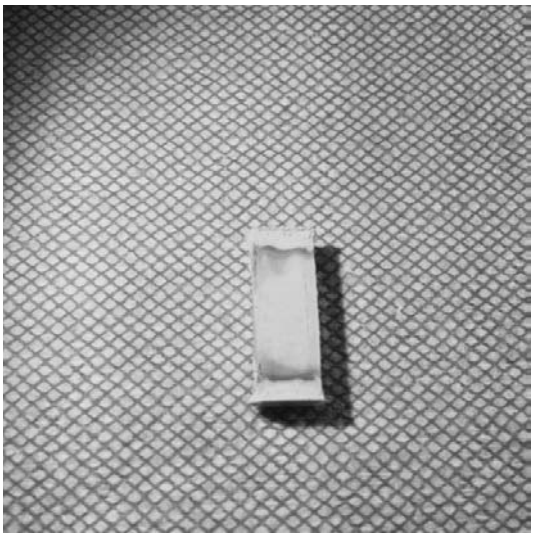

Figure A-178. Picture of HfB_2 specimen subjected to 75 MPa compressive creep stress for 20 h at 1500°C.

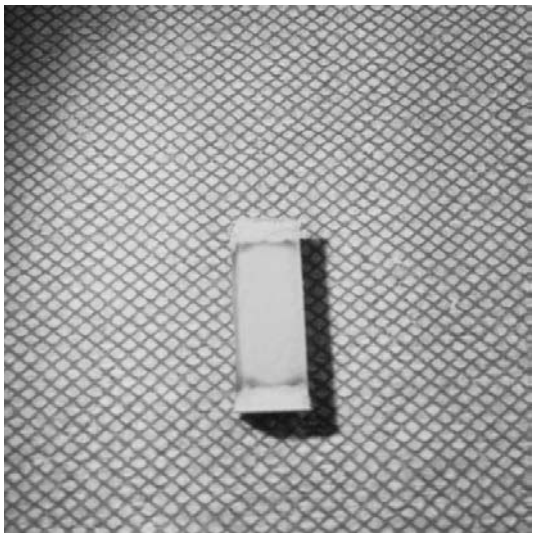

Figure A-177. Picture of HfB_2 specimen subjected to 75 MPa compressive creep stress for 20 h at 1500°C.

Figure A-179. Picture of HfB_2 specimen subjected to 75 MPa compressive creep stress for 30 h at 1500°C.

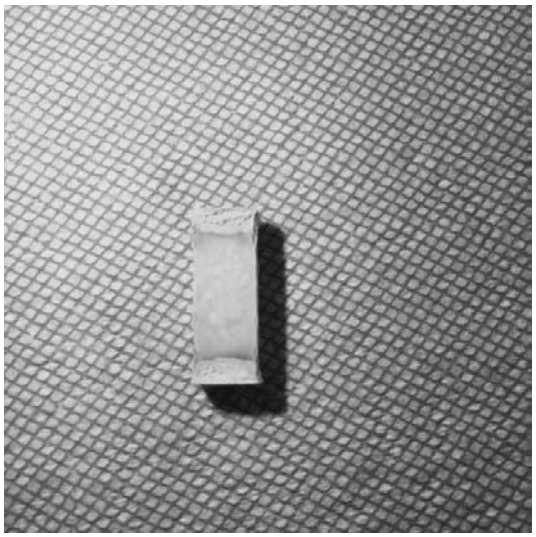

Figure A-180. Picture of HfB_2 specimen subjected to 75 MPa compressive creep stress for 30 h at 1500°C.

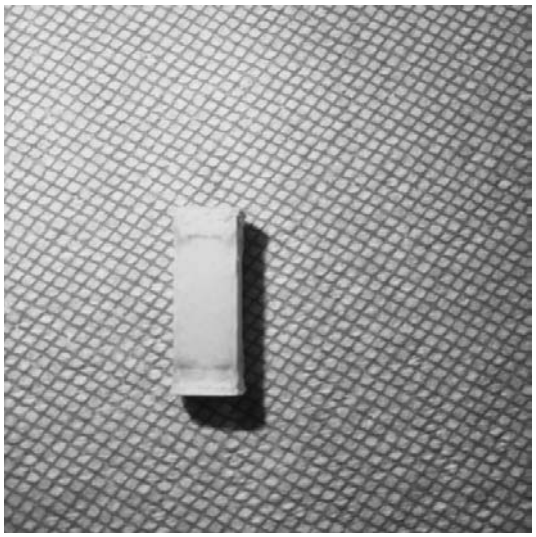

Figure A-181. Picture of HfB_2 specimen subjected to 75 MPa compressive creep stress for 30 h at 1500°C.

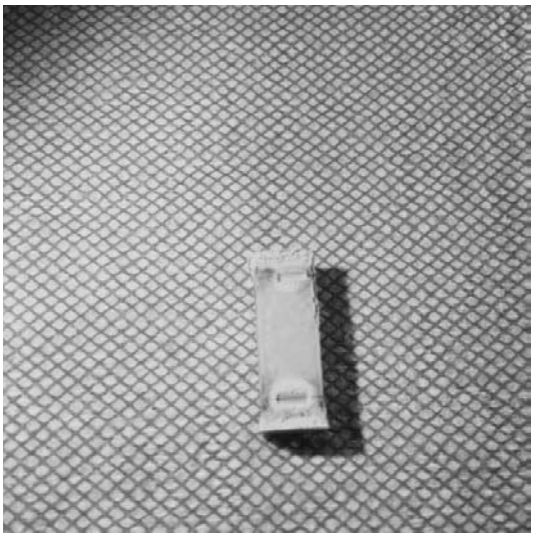

Figure A-182. Picture of HfB_2 specimen subjected to 75 MPa compressive creep stress for 30 h at 1500°C.

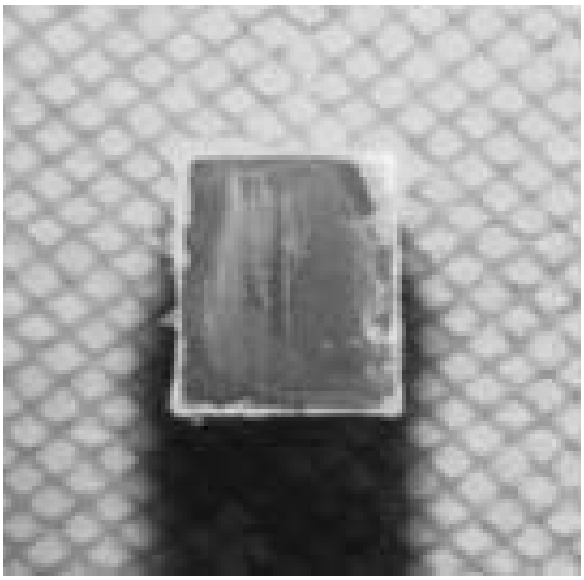

Figure A-183. Picture of HfB_2 specimen subjected to 75 MPa compressive creep stress for 30 h at 1500°C.

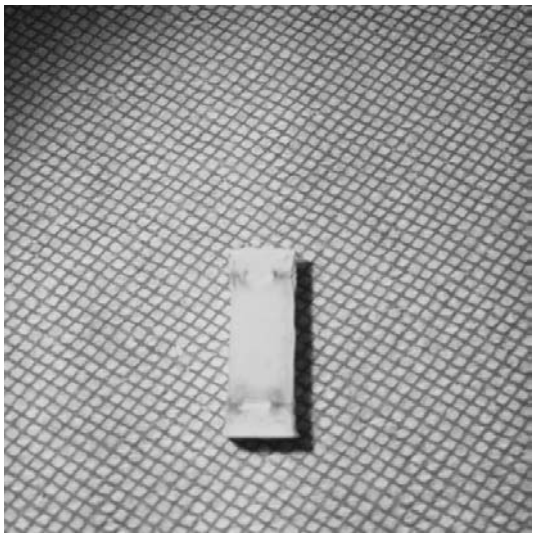

Figure A-184. Picture of HfB_2 specimen subjected to 75 MPa compressive creep stress for 30 h at 1500°C.

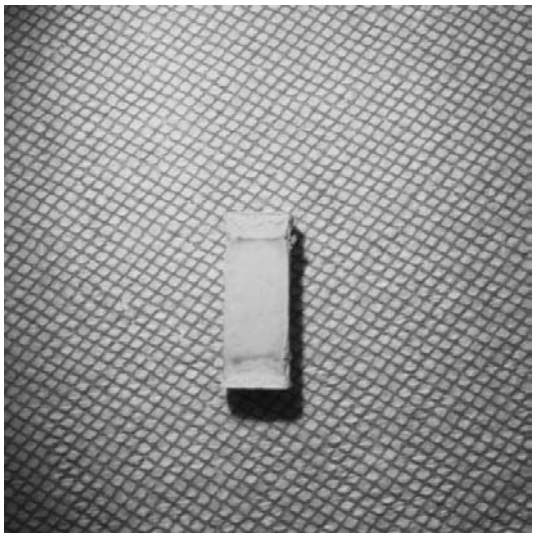

Figure A-185. Picture of HfB_2 specimen subjected to 75 MPa compressive creep stress for 30 h at 1500°C.

Figure A-186. Picture of HfB_2-10SiC specimen subjected to 75 MPa compressive creep stress for 66.3 h at 1500°C.

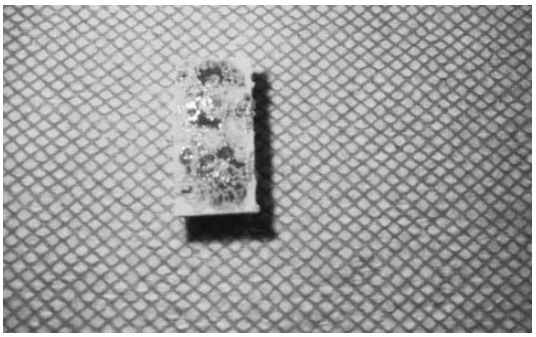

Figure A-187. Picture of HfB_2-10SiC specimen subjected to 75 MPa compressive creep stress for 66.3 h at 1500°C.

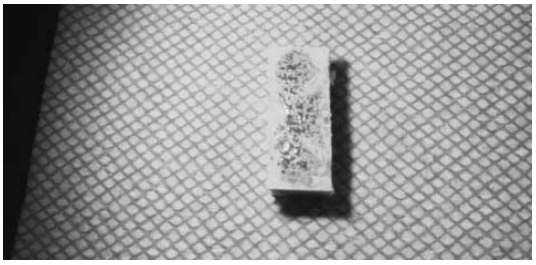

Figure A-188. Picture of HfB_2-10SiC specimen subjected to 75 MPa compressive creep stress for 66.3 h at 1500°C.

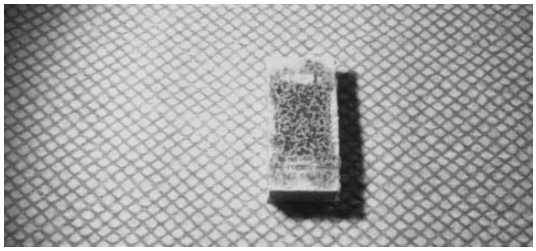

Figure A-189. Picture of HfB_2-10SiC specimen subjected to 75 MPa compressive creep stress for 66.3 h at 1500°C.

Figure A-190. Picture of HfB_2-10SiC specimen that failed upon load up to 100 MPa at 1500°C.

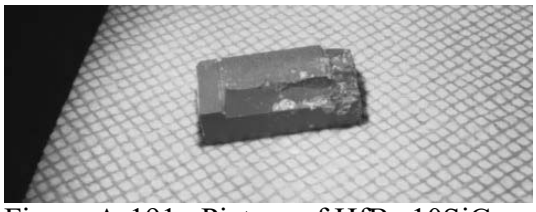

Figure A-191. Picture of HfB_2-10SiC specimen that failed upon load up to 100 MPa at 1500°C.

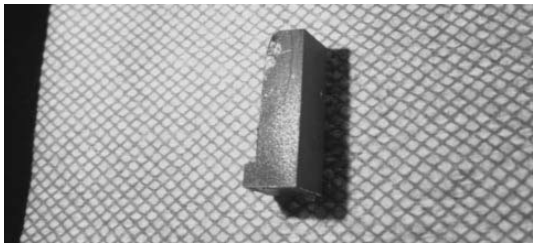

Figure A-192. Picture of HfB_2-10SiC specimen that failed upon load up to 100 MPa at 1500°C.

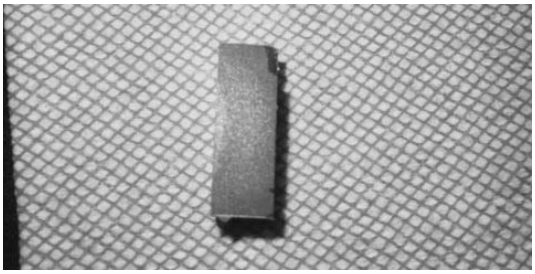

Figure A-191. Picture of HfB_2-10SiC specimen that failed upon load up to 100 MPa at 1500°C.

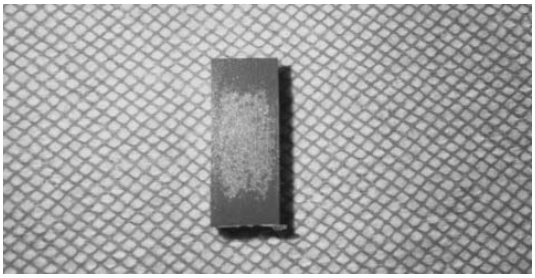

Figure A-193. Picture of HfB_2-10SiC specimen that failed upon load up to 100 MPa at 1500°C.

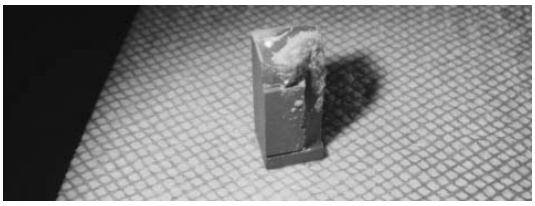

Figure A-194. Picture of HfB_2-10SiC specimen that failed upon load up to 100 MPa at 1500°C.

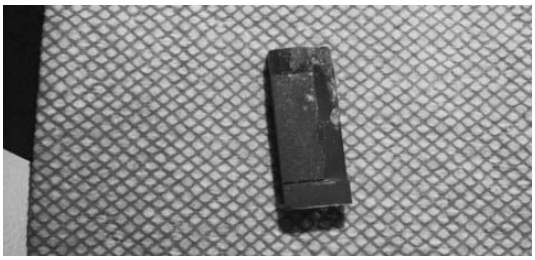

Figure A-195. Picture of HfB_2-10SiC specimen that failed upon load up to 100 MPa at 1500°C.

Figure A-196. Picture of Extensometer rods and argon feed tubes installed in closed furnace.

Figure A-197. Specimen loaded for compression creep testing.

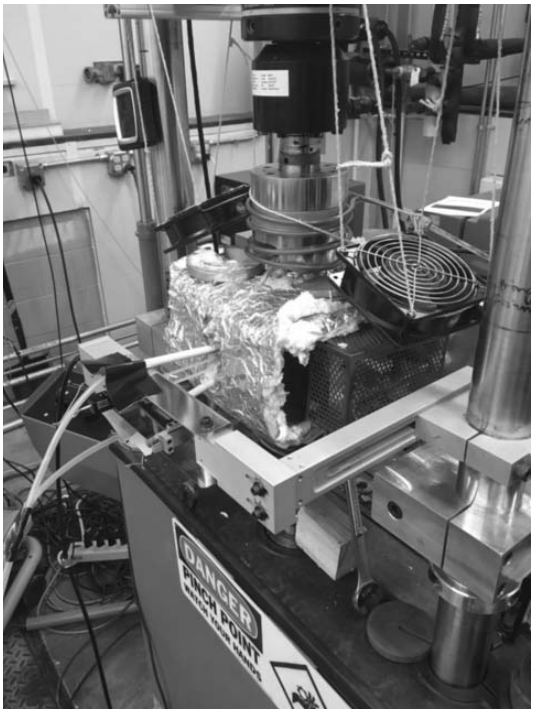

Figure A-198. Test facility loaded and ready for testing.

Figure A-199. Load train after testing HfB_2 specimen for 20 h at 75 MPa in air at 1500°C with four random orientation spacers.

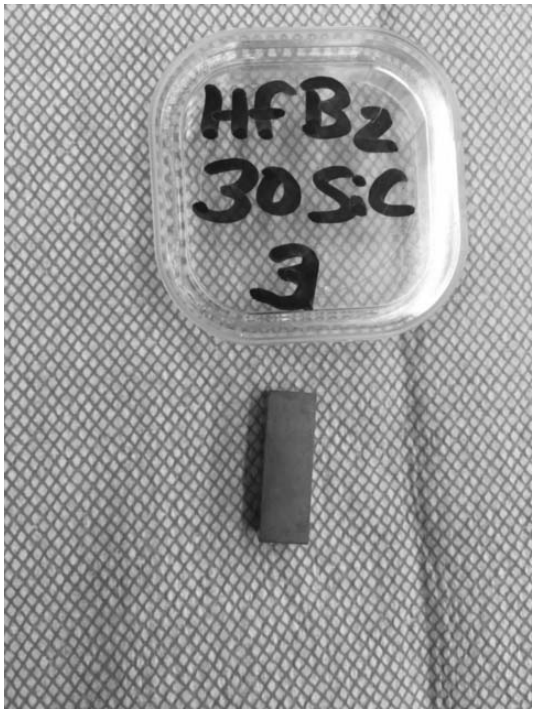

Figure A-200. Pre-test images of a HfB_2-30% to be subjected to compression creep at 100 MPa for 8.8 h.

Figure A-202. Pre-test images of a HfB_2-30% to be subjected to compression creep at 100 MPa for 8.8 h.

Figure A-201. Pre-test images of a HfB_2-30% to be subjected to compression creep at 100 MPa for 8.8 h.

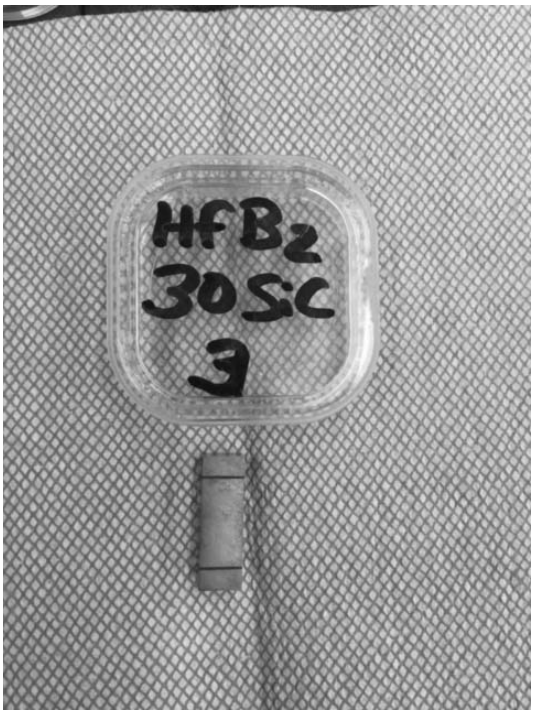

Figure A-203. Pre-test images of a HfB_2-30% to be subjected to compression creep at 100 MPa for 8.8 h.

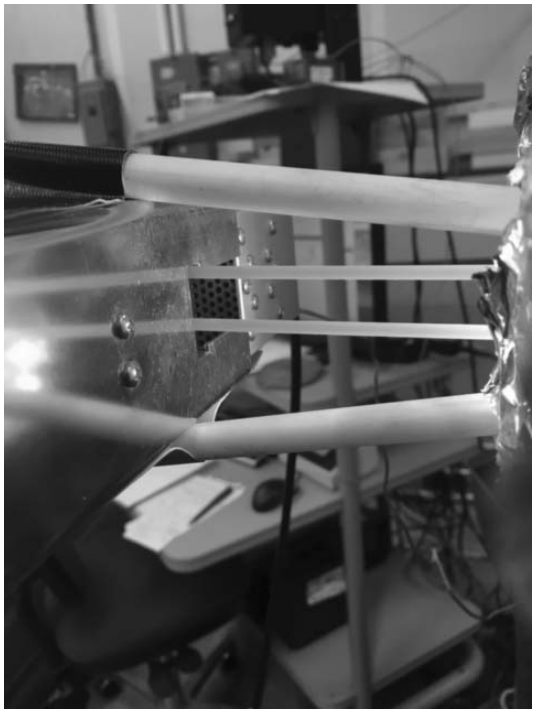

Figure A-204. Extensometer and argon tubes installed during furnace heat up.

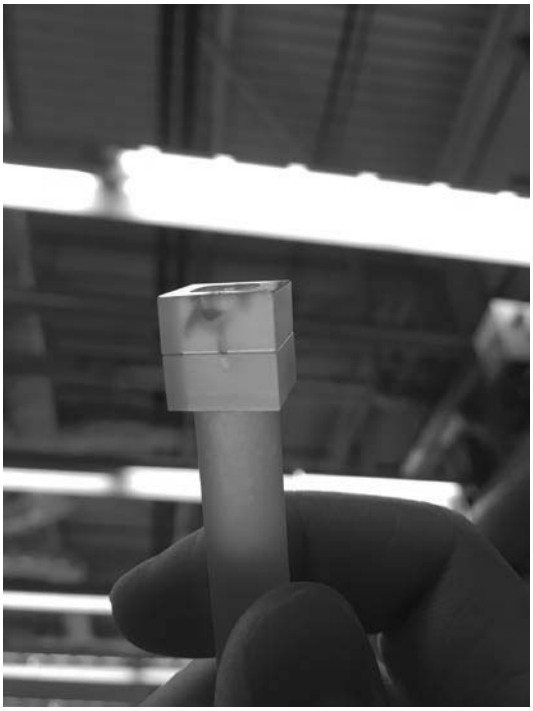

Figure A-206. Sapphire spacers damaged post-test and fused together.

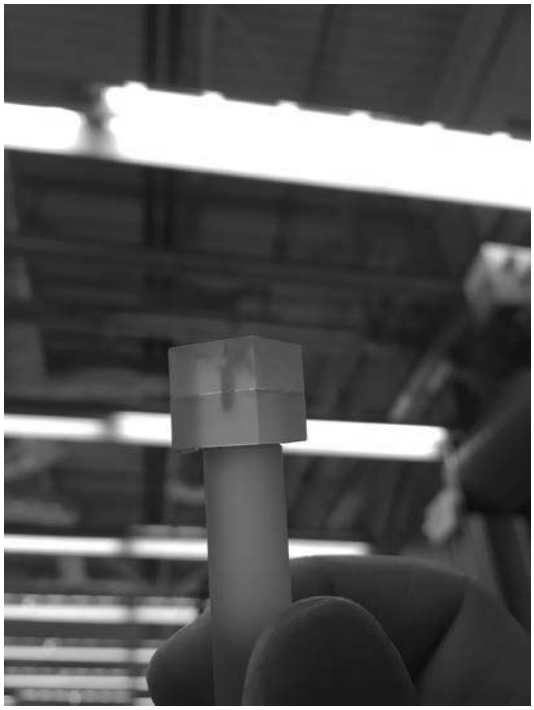

Figure A-205. Sapphire spacers damaged post-test and fused together.

Figure A-207. Load train subjected compression creep of HfB_2 specimen at 75 MPa for 30 h with four random orientation spacers.

Figure A-208. Load train subjected compression creep of HfB_2-10% SiC specimen at 75 MPa for 66.3 h with 4 random orientation spacers.

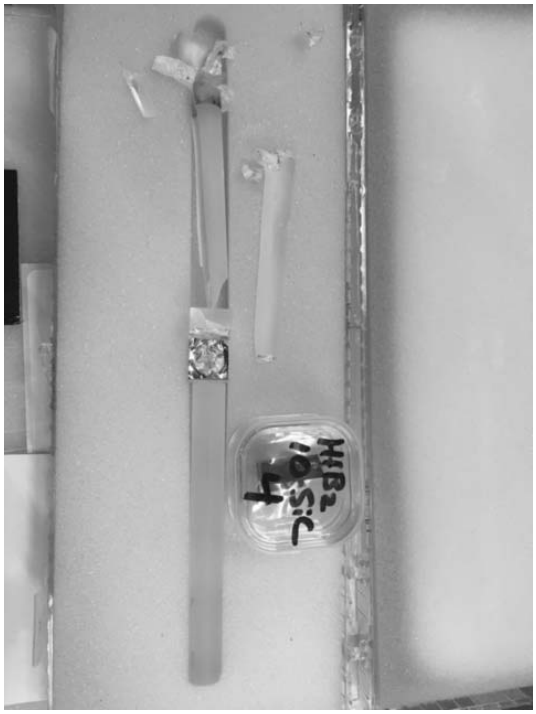

Figure A-209. Load train failure when subjected to 100 MPa compression stress with HfB_2-10% SiC specimen and 4 c-plane spacers.

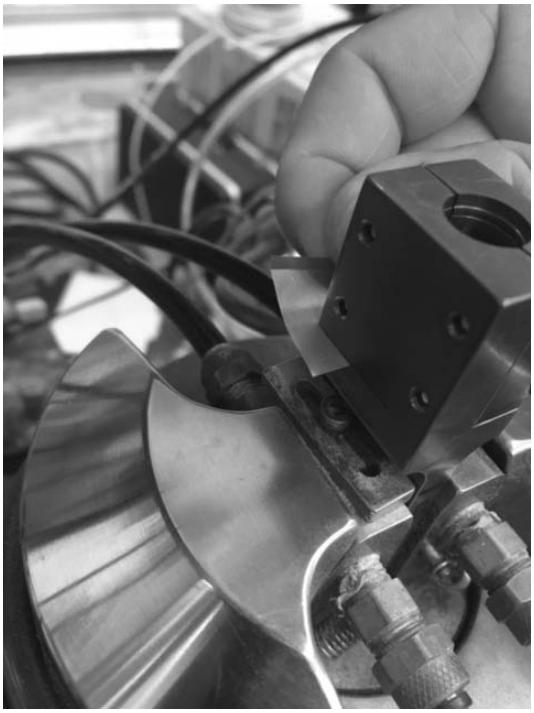
Figure A-210. Sliding copper foil into YAG holder slit.

Figure A-211. Picture of a HfB_2 specimen prior to being subjected to compression creep at 75 MPa for 20h at 1500°C in air.

Figure A-212. Picture of a HfB_2 specimen prior to being subjected to compression creep at 75 MPa for 20h at 1500°C in air.

Figure A-213. Picture of a HfB_2 specimen prior to being subjected to compression creep at 75 MPa for 20h at 1500°C in air.

Figure A-214. Picture of a HfB_2 specimen prior to being subjected to compression creep at 75 MPa for 20h at 1500°C in air.

Figure A-215. Picture of load train with a HfB_2 specimen after being subjected to compression creep at 75 MPa for 30h at 1500°C in air.

Figure A-216. Picture of load train with a HfB_2 specimen after being subjected to compression creep at 75 MPa for 30h at 1500°C in air.

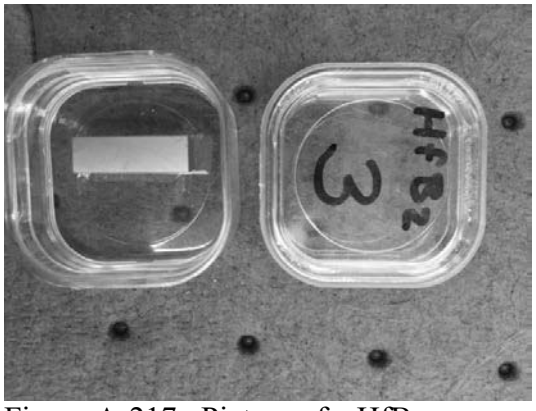

Figure A-217. Picture of a HfB_2 specimen prior to being subjected to compression creep at 75 MPa for 30h at 1500°C in air.

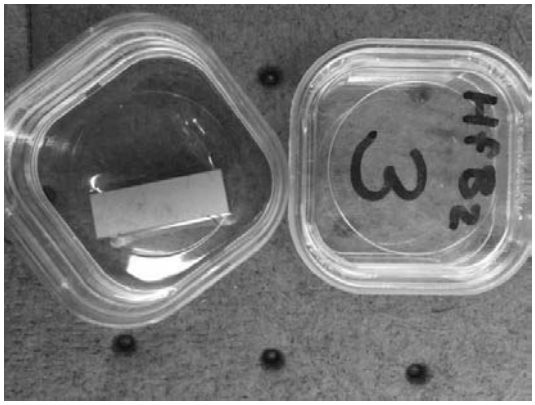

Figure A-218. Picture of a HfB_2 specimen prior to being subjected to compression creep at 75 MPa for 30h at 1500°C in air.

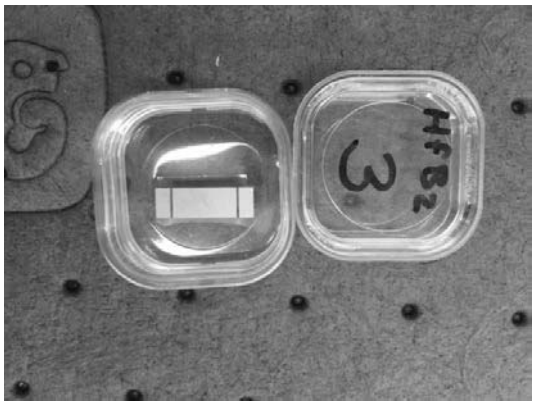

Figure A-219. Picture of a HfB_2 specimen prior to being subjected to compression creep at 75 MPa for 30h at 1500°C in air.

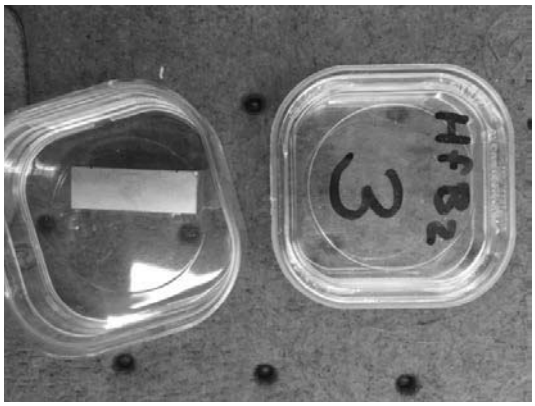

Figure A-220. Picture of a HfB_2 specimen prior to being subjected to compression creep at 75 MPa for 30h at 1500°C in air.

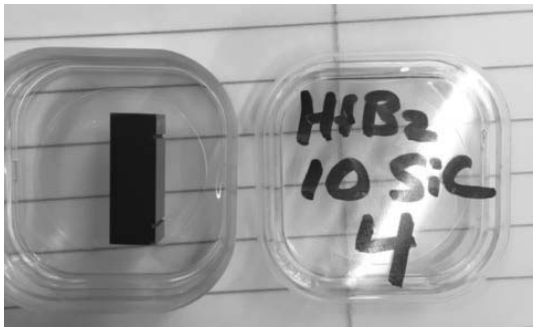

Figure A-221. Picture of a HfB_2-10% SiC specimen prior to failure upon load up to a compression Stress of 100 MPa at 1500°C in air.

Figure A-222. Picture of a HfB_2-10% SiC specimen prior to failure upon load up to a compression Stress of 100 MPa at 1500°C in air.

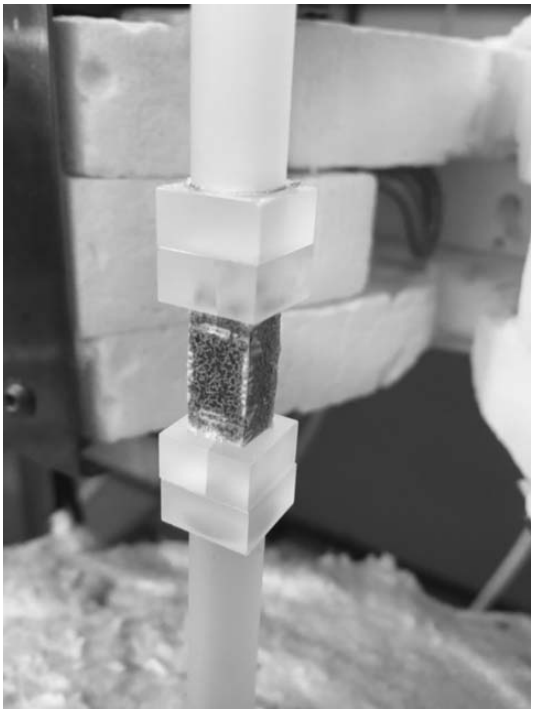

Figure A-222. Picture of the load train containing a HfB_2-10% SiC specimen after compression creep at 75 MPa for 66.3 h at 1500°C in air.

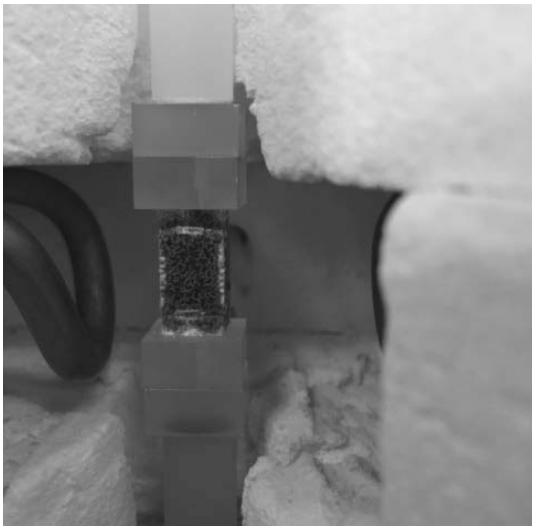

Figure A-222. Picture of the load train containing a HfB_2-10% SiC specimen after compression creep at 75 MPa for 66.3 h at 1500°C in air.

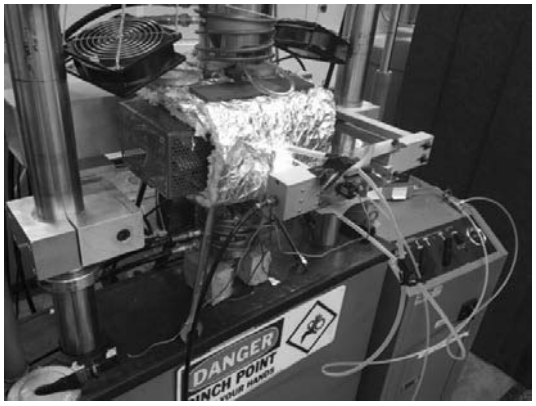

Figure A-223. Test facility during a compression creep test at 1500°C.


Figure A-224. Overnight camping during the compression creep testing.

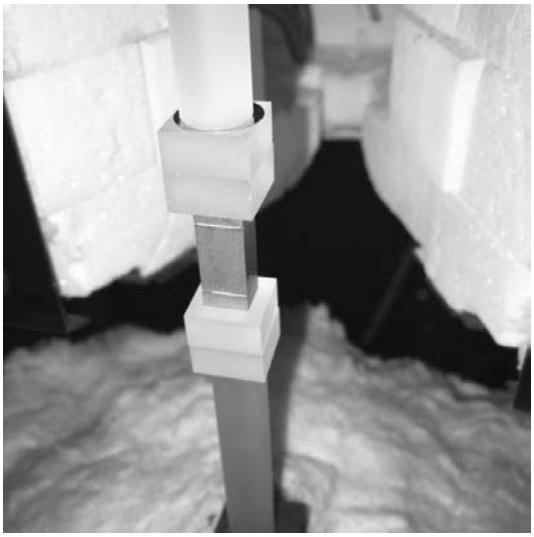
Figure A-225. Load train of HfB_2-10% SiC specimen prior to compression creep test at 75 MPa for 66.3 h at 1500°C in air.

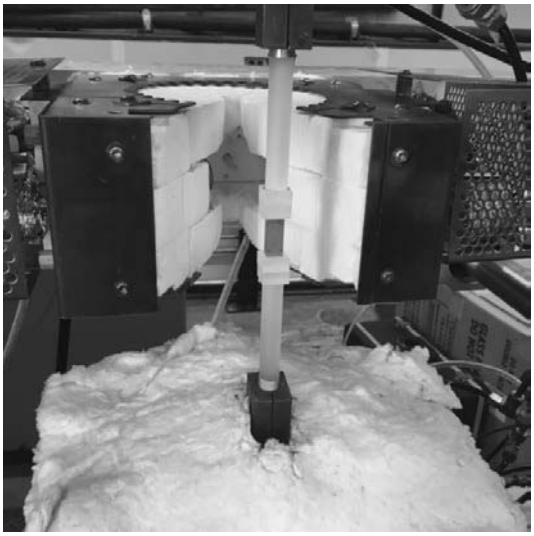
Figure A-226. Load train of HfB_2-10% SiC specimen prior to compression creep test at 75 MPa for 66.3 h at 1500°C in air.

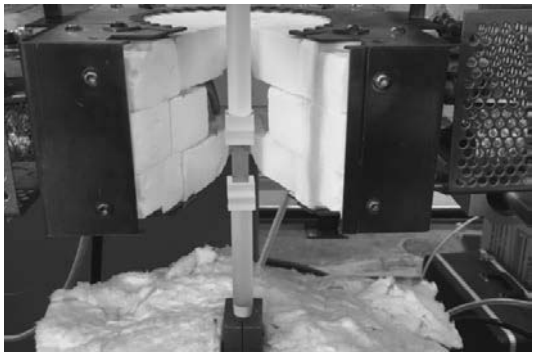

Figure A-227. Load train of HfB_2-10% SiC specimen prior to compression creep test at 75 MPa for 66.3 h at 1500°C in air.

Figure A-228. Load train of HfB_2-10% SiC specimen after a compression creep test at 75 MPa for 66.3 h at 1500°C in air.

Figure A-229. Initial testing of alignment tool during temperature calibrations.

Figure A-230. MTS software (foreground) and temperature controller (background).

Appendix B: Test Procedures

Pre-Test

Specimen:

- Select specimen, new/refurbished YAG rods, new/refurbished sapphire extensometer rods, new sapphire spacers, temperature and stress for test

- Weigh, measure (caliper), and photo specimen

- Calculate load required for desired stress
MTS Station

- If MTS Station Manager needs to be opened, select "Temperature.cfg" and desired parameters

- Select "New Specimen" on MTS Station Manager, enter specimen name, and hit <ENTER>

- Reset and edit procedure Creep.000 (load, temp, displacement limit detector values) and Save

- Check to ensure heating element leads are clear of metal-to-metal contact with the furnace and that the braids are securely connected (do not over tighten)

- Power on standalone hydraulic pump, Eurotherm controller, grip hydraulic power

- Clear MTS Station Manager limit detectors, reset/override if needed, and start hydraulics (low then high)

- Start function generator (1 Hz, 5 mm sine wave)

- Stop function generator after a minimum of 30 minutes

Load Train Assembly:

- Assemble custom YAG holder with silver plated screws and spring washers

- Wrap steel shims around alignment rod

- Insert alignment rod into custom holder, finger tighten setscrews so rod is snug

- Insert assembly into MTS grips with 5mm separation between custom holder and MTS grip with both holders touching rear L-brackets, close top grip

- In displacement control, zero load via MTS interface, switch to force control with 0 lbf command, close bottom grip

- Ensure alignment rod is still free to move (i.e. not loaded)

- Return to displacement control, raise top crosshead, remove alignment rod

- Insert copper foil into slit at base of both custom holders

- Shim the YAG rods with enough copper foil to wrap one time around and insert into custom grips; secure set screws with hex key until finger tight

- Bring YAG rods together to verify alignment; repeat alignment procedure if not aligned

- In displacement control, zero force

- Lower bottom crosshead, place wrap-around soft insulation through bottom YAG rod, raise crosshead

- Cut 2 pieces of Pt foil to size of a sapphire spacer

- Load one side of 3D printed alignment tool: Pt foil, 2 sapphire spacers, test specimen, 2 sapphire spacers, Pt foil

- Using other side of 3D printed tool bring YAG rods together so they are almost to the spacer cutouts, as shown in Figure 16

- Carefully insert loaded half of alignment tool such that the YAG rods fit into their respective cutouts as shown in Figure 15.

- Place other half of alignment tool on the exposed side, encasing load train with alignment tool as shown in Figure 15.

- Holding the tool together, raise lower crosshead in 0.1mm increments until -10lbf is reached

- Switch to force control and command -50lbf

- Carefully remove alignment tool to verify specimen is square to extensometer

- If adjustments are required rotate load train assembly using alignment tool; this may be accomplished at -50lbf but could require restarting

- Verify alignment; repeat alignment procedure if not aligned; zero displacement

- Set values for displacement limit detectors on MTS Station Manager, and activate for Station Power Off (+9/-5 mm)

- Replace extensometer rods (use fresh rods every time)

- Test extensometer on specimen; adjust rods as necessary; rods must be as centered in window as possible

- Zero strain; remove extensometer

Insulation:

- Slide furnace forward and secure; insert pie piece

- Place insulation around bottom YAG rod, between wrap around and furnace, to plug lower hole

- Wrap up wrap around soft insulation; secure with weight bar

- Place top soft insulation; secure with weights

- Support bottom of wrap around soft insulation with braces (metal ruler, wrenches)

- Place side soft insulation

- Place extensometer; verify strain reading should be near zero with appropriate noise levels (<1%); zero strain

- Insert argon feeding tubes (even if testing in air), secure with tape to extensometer mounting brace

Heat:

- Turn on coolant to grips; ensure chiller is filled with distilled water

- Turn on heating element cooling fans and cooling air for extensometer

- Start procedure “Creep.000” (starts heat up and displays “Start”, “End”, and “ABORT” test buttons)

- Record lab temperature, relative humidity, and anytime the temperature goes into or out of limits

- When furnace begins to glow, visually verify the specimen and extensometer are in good position

- After reaching target temperature, wait for 1 hour of temperature soak

- Verify temperature and strain readings are steady before proceeding with Load

Load:

- Verify good thermal strain; verify temperature and strain are stable and within limits

- Select “Start Test” button (loads up to desired load)

<u>During Test</u>

- Check to ensure extensometer is clear of obstacles and is in grooves on specimen (use welding goggles)

- Check temperature, strain, displacement, and force values

- Check to ensure displacement is not too close to limit detector values

- Record strain, displacement, argon pressures, and time

<u>Post Test</u>

- “End Test” button (commands -50 lbf and 0°C)

- Let cool naturally until 100°C (opening early can shock the YAG and crack them)

- Remove argon feeding tubes, extensometer, top and side soft insulations; raise topside of wrap around insulation

- Remove pie piece; photo specimen; “Release Specimen” button, switch to displacement control

- Lower bottom crosshead in 0.1 mm intervals until there’s clearance to remove specimen

- Remove, photo, and secure specimen

- Power down grip coolant, hydraulics on MTS Station Manager, Eurotherm controller

- Remove bottom supports and wrap around insulation

- Push back furnace and secure

- Remove top and bottom custom grips and power down hydraulics for grips
- Power down standalone hydraulic pump
- Remove YAG rods from custom holders and turn in for repair if reparable
- Copy and analyze data from MTS computer
- Weigh and measure specimen; assess oxide scale and thickness

References

[1] "History of Flight Timeline," AIAA : The American Institute of Aeronautics and Astronautics. [Online]. Available: https://www.aiaa.org/secondarytwocolumn.aspx?id=5674. [Accessed: 08-Sep-2016].

[2] J. D. Anderson, Hypersonic and High-Temperature Gas Dynamics; Second Edition. AIAA, 2006.

[3] M. F. Ashby, Materials Selection in Mechanical Design, 4th ed. Burlington: Elsevier Science, 2011.

[4]. Shaffer, "Precision Strike Annual Review," 17-Mar-15. [Online] Available: http://www.dtic.mil/ndia/2015PSAR/AlShaffer.pdfA. [Accessed: 08-Sep-2016].

[5] "THE X-15 PROGRAM IN RETROSPECT," NASA. [Online]. Available: http://history.nasa.gov/x15lect/structur.html. [Accessed: 08-Sep-2016].

[6] W. G. Fahrenholtz, G. E. Hilmas, I. G. Talmy, and J. A. Zaykoski, "Refractory Diborides of Zirconium and Hafnium," Journal of the American Ceramic Society J American Ceramic Society, vol. 90, no. 5, pp. 1347–1364, 2007.

[7] E. Wuchina, E. Opila, W. Fahrenholtz, and I. Talmy, "UHTCs: Ultra-High Temperature Ceramic Materials for Extreme Environment Applications," Interface, 2007.

[8] "Ceramic History." [Online]. Available: http://depts.washington.edu/matseed/mse_resources/webpage/ceramics/ceramichistory.htm. [Accessed: 08-Sep-2016].

[9] W. F. Smith, Principles of materials science and engineering. New York: McGraw-Hill, 1996.

[10] K. K. Chawla, Ceramic matrix composites. London: Chapman & Hall, 1993.

[11] P. Wollgramm, H. Buck, K. Neuking, A.B. Parsa, S. Schuwalow, J. Rogal, R. Drautz, G. Eggeler, On the role of Re in the stress and temperature dependence of creep of Ni-base single crystal superalloys, Materials Science and Engineering: A, Volume 628, 25 March 2015, Pages 382-395, ISSN 0921-5093, http://dx.doi.org/10.1016/j.msea.2015.01.010.

[12] S. L. Winder, "MECHANICAL TESTING OF ULTRA-HIGH TEMPERATURE CERAMICS AT 1500°C IN AIR – DEVELOPMENT OF AN EXPERIMENTAL FACILITY AND TEST METHOD," dissertation, Defense Technical Information Center, 2015.

[13] M. W. Bird, R. P. Aune, F. Yu, P. F. Becher, and K. W. White, “Creep behavior of a zirconium diboride–silicon carbide composite,” Journal of the European Ceramic Society, vol. 33, no. 13-14, pp. 2407–2420, 2013.

[14] R. T. DeHoff, Thermodynamics in materials science. Boca Raton: CRC/Taylor & Francis, 2006.

[15] C. B. Bargeron, R. C. Benson, R. W. Newman, A. N. Jette, and T. E. Phillips, “Oxidation Mechanisms of Hafnium Carbide and Hafnium Diboride in the Temperature Range 1400 to 2100˚C,” John Hopkins APL Tech Digest, vol. 14, no. 1, pp. 29–36, 1993.

[16] M. Mallik, K. Ray, and R. Mitra, “Oxidation behavior of hot pressed ZrB2–SiC and HfB2–SiC composites,” Journal of the European Ceramic Society, vol. 31, no. 1-2, pp. 199–215, 2011.

[17] A. DeGregoria, “CREEP AND OXIDATION OF HAFNIUM DIBORIDE-BASED ULTRA HIGH TEMPERATURE CERAMICS AT 1500˚C,” dissertation, Defense Technical Information Center, 2015.

[18] Carney, C. M., Parthasarathy, T. A. and Cinibulk, M. K. (2011), Oxidation Resistance of Hafnium Diboride Ceramics with Additions of Silicon Carbide and Tungsten Boride or Tungsten Carbide. Journal of the American Ceramic Society, 94: 2600–2607.

[19] C. J. Armani, Creep Performance of Oxide Ceramic Fiber Materials at Elevated Temperature in Air and in Steam; PhD Dissertation, Air Force Institute of Technology, Dayton, OH 2011.

[20] Desai, P. D., and C. Y. Ho. *THERMAL LINEAR EXPANSION OF NINE SELECTED AISI STAINLESS STEELS*. Defense Technical Information Center, 1978. Print.

[21] “YAG YTTRIUM ALUMINU GARNET LASER MATERIALS.” VLOC, Web. <http://users.unimi.it/aqm/wp-content/uploads/YAGBrochure.pdf>.

[22] Fischer, John W., W. R. Compton, Nancy A. Jaeger, and Daniel C. Harris. "Strength of sapphire as a function of temperature and crystal orientation." Window and Dome Technologies and Materials II (1990): n. pag. Web. <http://www-eng.lbl.gov/~shuman/NEXT/MATERIALS%26COMPONENTS/Quartz/sapphire-strength_temp_orient_Fischer.pdf>.

[23] Winder, S.l., M.b. Ruggles-Wrenn, T. Parthasarathy, T. Key, and C.m. Carney. "Thermo-chemical compatibility of hafnium diboride with yttrium aluminum garnet at 1500°C in air." Journal of the European Ceramic Society 35.9 (2015): 2437-444. Web.

[24] K. Shugart and E. Opila, “SiC Depletion in ZrB2-30 vol% SiC at Ultrahigh Temperatures,” J. Am. Ceram. Soc., vol. 98, no. 5, pp. 1673–1683, May 2015.

[25] C. M. Carney, “Oxidation resistance of hafnium diboride-silicon carbide from 1400 to 2000°C,” Journal of Materials Science, vol. 44, no. 20. p. 5673, Jan-2009

[26] T. A. Parthasarathy, R. A. Rapp, M. Opeka and R. J. Kerans, 'A Model for the Oxidation of ZrB2, HfB2, and TiB2,' Acta. Mater., 55 [17] 5999-6010 (2007).

[27] T. A. Parthasarathy, R. A. Rapp, M. Opeka and M. K. Cinibulk, 'Modeling Oxidation Kinetics of SiC-Containing Refractory DIborides,' J. Am. Ceram. Soc., 95 [1] 338-349 (2012).

REPORT DOCUMENTATION PAGE

Form Approved
OMB No. 0704-0188

1. REPORT DATE *(DD-MM-YYYY)*	2. REPORT TYPE	3. DATES COVERED *(From - To)*
23-03-2017	Master's Thesis	1 Oct 2015 - 23 Mar 2017

4. TITLE AND SUBTITLE

Stressed Oxidation of Hafnium Diboride in Air at 1500˚C

5a. CONTRACT NUMBER

5b. GRANT NUMBER

5c. PROGRAM ELEMENT NUMBER

6. AUTHOR(S)

Bowen, Thomas A., Capt

5d. PROJECT NUMBER

5e. TASK NUMBER

5f. WORK UNIT NUMBER

7. PERFORMING ORGANIZATION NAME(S) AND ADDRESS(ES)

Air Force Institute of Technology
Graduate School of Engineering and Management (AFIT/EN)
2950 Hobson Way
Wright-Patterson AFB OH 45433-7765

8. PERFORMING ORGANIZATION REPORT NUMBER

AFIT-ENY-MS-17-M-243

9. SPONSORING/MONITORING AGENCY NAME(S) AND ADDRESS(ES)

Air Force Office of Scientific Research
Ali Sayir, PhD, Aerospace Materials for Extreme Environments
AFOSR, 875 North Randolph St.
Arlington, VA 22203
ali.sayir.2@us.af.mil

10. SPONSOR/MONITOR'S ACRONYM(S)

AFRMC AFOSR/RTB

11. SPONSOR/MONITOR'S REPORT NUMBER(S)

12. DISTRIBUTION/AVAILABILITY STATEMENT

DISTRIBUTION STATEMENT A. APPROVED FOR PUBLIC RELEASE; DISTRIBUTION UNLIMITED.

13. SUPPLEMENTARY NOTES

This work is declared a work of the U.S. Government and is not subject to copyright protection in the United States.

14. ABSTRACT

Hypersonic vehicles with narrow airfoils produce thin boundary layers and shock temperatures in excess of 2000°C, exceeding the operating limits of traditional aerospace materials. The use of ultra-high temperature ceramics (UHTCs) allows for operating temperatures far exceeding those of metallic alloys. One such UHTC is hafnium diboride (HfB2). Transition metal diborides generally experience significant oxidation degradation at elevated temperatures. The use of additives, such as silicon carbide (SiC) has been shown to reduce the oxidation of transition metal diborides. This research focused on the compressive creep of HfB2 with varying amounts of SiC in air at 1500°C. The existing test set-up was successfully modified to permit compression creep testing at higher stress (75-100 MPa) levels for longer durations (>66 h). Post-test microstructural examination revealed significant SiC-depleted layers in HfB2-SiC samples. Oxide layers in HfB2 samples subjected to 75 and 100 MPa compressive creep tests were significantly thinner than those observed under zero stress, suggesting that sustained compressive load may restrict oxidation.

15. SUBJECT TERMS

Creep, Compression, UHTC, Ceramic, Hafnium, Diboride, Oxidation, SiC, HfB2, Hypersonic

16. SECURITY CLASSIFICATION OF:			17. LIMITATION OF ABSTRACT	18. NUMBER OF PAGES	19a. NAME OF RESPONSIBLE PERSON
a. REPORT	b. ABSTRACT	c. THIS PAGE			Dr. Marina Ruggles-Wrenn, AFIT/ENY
U	U	U	UU	129	19b. TELEPHONE NUMBER *(Include area code)* 937-255-3636x4641 marina.ruggles-wrenn@afit.edu